STUK

STUK-YTO-TR 209 / AUGUST 2004

DECOVALEX III, 1999–2003

An international project for the modelling of coupled Thermo–Hydro–Mechanical processes for spent fuel disposal

Finnish national contributions

Esko Eloranta (ed.)

STUK • **SÄTEILYTURVAKESKUS**
STRÅLSÄKERHETSCENTRALEN
RADIATION AND NUCLEAR SAFETY AUTHORITY

Osoite/Address • Laippatie 4, 00880 Helsinki
Postiosoite / Postal address • PL / P.O.Box 14, FIN-00881 Helsinki, FINLAND
Puh./Tel. (09) 759 881, +358 9 759 881 • Fax (09) 759 88 500, +358 9 759 88 500 • www.stuk.fi

The conclusions presented in the STUK report series are those of the authors and do not necessarily represent the official position of STUK.

ISBN 951-712-900-9 (print, Dark Oy, Vantaa/Finland 2004)
ISBN 951-712-901-7 (pdf)
ISSN 0785-9325

ELORANTA Esko (ed.). DECOVALEX III, 1999–2003. An international project for the modelling of coupled Thermo–Hydro–Mechanical processes for spent fuel disposal. Finnish national contributions. STUK-YTO-TR 209. Helsinki 2004. 12 + 24 + 26 + 11 + 42 pp.

Keywords: rock mechanics, geohydrology, permafrost, bentonite, coupled processes, numerical modelling

Abstract

During the years 1999–2003 an international project was going on to study the coupled Thermo–Hydro–Mechanical (THM) processes in a spent fuel repository. The project was called DECOVALEX III and it was a direct continuation of DECOVALEX II project which was carried out in 1995–1999. DECOVALEX is an acronym coming from the "DEvelopment of COupled models and their VALidation against EXperiments in nuclear waste isolation".

The Finnish national contributions to the project were: (1) development of THM model for the bentonite buffer (Task 1, FEBEX-experiment), (2) upscaling and homogenization of fractured rock (Task 3, Bench Mark Test 2 – BMT 2), and (3) permafrost modelling (Task 3, BMT 3). In addition to these issues a master's thesis concerning the stability of the canister in the bentonite buffer was made at Helsinki University of Technology.

The Finnish work was reviewed by a *National DECOVALEX III Group* which had eight meetings during the years 1999–2003. The group had members from different research organizations, universities, rock engineering consulting companies, and Posiva Oy. Altogether the number of group members was about 20.

This report is a summary report of the Finnish national work done in DECOVALEX III.

ELORANTA Esko (toim.). DECOVALEX III, Kansainvälinen projekti kytkettyjen termo–hydro–mekaanisten prosessien mallintamiseksi ydinjätteen loppusijoitusta varten. Suomalaiset osatyöt. STUK-YTO-TR 209. Helsinki 2004. 12 + 24 + 26 + 11 + 42 s.

Avainsanat: kalliomekaniikka, geohydrologia, ikirouta, bentoniitti, kytketyt prosessit, numeerinen mallinnus

Tiivistelmä

Vuosina 1999–2003 oli käynnissä kansainvälinen projekti kytkettyjen termo–hydro–mekaanisten (THM) prosessien tutkimiseksi käytetyn ydinpolttoaineen loppusijoitusta varten. Projektin nimi oli DECOVALEX III ja se oli suoraa jatkoa vuosina 1995–1999 käynnissä olleelle DECOVALEX II -projektille.

Suomen kansallinen osallistuminen käsitti seuraavat aihepiirit: (1) bentoniitin kytketyn THM-mallin muodostamisen, joka kuului Task 1:een eli FEBEX-kokeeseen, (2) rakoilleen kallion ominaisuuksien skaalautuminen ja homogenisointi, jotka kuuluivat Task 3:n Bench Mark Test 2:een (BMT 2) ja (3) ikiroudan mallintaminen, joka kuului Task 3:n BMT 3:een. Näiden lisäksi projektin kansallisen työn puitteissa tehtiin Teknillisessä korkeakoulussa yksi diplomityö, joka käsitteli kapselin stabiiliutta bentoniittipuskurissa.

Suomen kansallista työtä tarkasteli kansallinen *DECOVALEX III -ryhmä*, jolla oli kahdeksan kokousta vuosien 1999–2003 aikana. Ryhmään kuului tutkijoita ja asioista muutoin kiinnostuneita eri tutkimusorganisaatioista, yliopistoista, kalliorakentamisen konsulttitoimistoista ja Posiva Oy:stä. Kaikkiaan jäseniä oli n. 20.

Tämä raportti on kansallisen työn yhteenveto DECOVALEX III -projektissa.

Contents

Introduction

The international DECOVALEX project has been in progress since 1991. The first phase was carried out in 1991–1995, the second phase in 1995–1999, and the third phase in 1999–2003. The Radiation and Nuclear Safety Authority (STUK) has taken part in all phases. This report describes the national work done in the third phase. The national activities carried out in the first and second phases have also been reported in STUK-YTO-TR series as reports (Eloranta 1996) and (Eloranta 2000), respectively. The name 'DECOVALEX' is an acronym, and means 'an international co-operative project for the DEvelopment of COupled models and their VALidation against EXperiments in nuclear waste isolation'. STUK has been one of the 14 Funding Organizations in the international project.

The project organization structure has been the same as in the previous DECOVALEX phases. SKI from Sweden was the managing participant. The Royal School of Technology (Stockholm) acted as a secretariat, and the funding organizations formed the Steering Committee of the project. The chairman of the Steering Committee was Dr. Chin-Fu Tsang from Lawrence Berkeley National Laboratory. Funding organizations supported and supervised also their Research Teams.

The main interest in the project has been the different ways to model the coupled Thermo–Hydro–Mechanical phenomena occurring in a repository of spent nuclear fuel. These processes are especially important in consideration of radionuclide release and transport from the repository. The main emphasis has been in fractured rocks and buffer materials and in the role in Performance Assessment (PA). International co-operation has also provided exchanges of laboratory and field data for validation purposes, and prepared statements on coupled T–H–M issues for performance assessment.

STUK concentrated its interests on three issues, i.e., (1) the modelling of the bentonite behaviour, (2) the upscaling and homogenization of hydro-mechanical properties of fractured rock, and (3) the modelling of the development of permafrost as well as the influences of permafrost on the repository. The modelling of bentonite buffer was studied at Helsinki University of Technology, Institute of Mathematics, the upscaling and homogenization of fractured rock were studied at Uppsala University in Sweden and at the Helsinki University of Technology, Laboratory of Rock Engineering. The permafrost issues were studied at the Helsinki University of Technology, Laboratory of Structural Mechanics. The national reports of these issues are included as appendixes in the present report.

In addition to these issues a master's thesis was made at the Helsinki University of Technology, Insititute of Mathematics. The thesis dealt with the mechanical stability of a canister in a bentonite buffer (Lahtinen 2002).

The participants and activities of DECOVALEX III project

The following organizations have acted as the Funding Organizations of DECOVALEX III project:

- U.S. Department of Energy, DOE, USA
- Svensk Kärnbränslehantering AB, SKB, Sweden
- Radiation and Nuclear Safety Authority, (Säteilyturvakeskus), STUK, Finland
- ENRESA, Spain
- Ontario Power Generation, OPG, Canada
- Swedish Nuclear Power Inspectorate, (Statens Kärnkraftinspektion), (SKI), Sweden
- NIREX Ltd., United Kingdom
- CEA CADARACHE, France
- US NRC, USA
- Canadian Nuclear Safety Commission, CNCS, Canada
- IRSN, France
- ANDRA, France
- Japan Nuclear Cycle Development Institute, (JNC), Japan
- Federal Institute for Geosciences and Natural Resources, BGR, Germany.

The international project arranged seven workshops. During the workshops also Steering Committee Meetings took place. The workshops have been:

1. Las Vegas, USA, October, 5–6, 1999 (start-up meeting)
2. Meiringen, Switzerland, June 6–9, 2000
3. Tokai, Japan, January 22–27, 2001
4. Naantali (Nådendal), Finland, October 22–26, 2001
5. Toronto, Canada, June 10–13, 2002
6. Berlin, Germany, January 28–30, 2003
7. Stockholm, Sweden, October 13–15, 2003.

There are also web-pages for DECOVALEX project: <www.decovalex.com>. The documents and data have been distributed and transferred mainly via internet.

The tasks of the international project

The following characterizations of different tasks are based on the descriptions on the DECOVALEX web-pages: www.decovalex.com.

Task 1 FEBEX in-situ T–H–M experiment

The test case was based on the now completed FEBEX in-situ experiment carried out in Switzerland. Two large scale in-situ experiments were performed: 1) an in-situ field test of heater-buffer-rock system with a long period of heating, followed by 2) a large scale laboratory "mock-up" test. The aim of the project was demonstrating the present capabilities for building bentonite barriers in conditions similar to actual repository design and providing monitoring data to understand coupled THM and THG (Thermo–Hydro–Geochemical) processes in the near-field. Large quantities of monitoring data regarding stress, deformation, water content, water pressure, and temperature distributions and their histories with time at a large number of monitoring places were recorded in-situ and a large number of rock/buffer property parameters were measured also in laboratory tests.

Based on this data package, a bench mark test (BMT) problem was proposed. The object of the BMT was to apply different numerical models and codes to simulate the FEBEX in-situ field test, with the support of available monitored in-situ system responses and laboratory property data, for the coupled hydro–mechanical or coupled thermo–hydro–mechanical processes of the fractured rock-buffer-heater system. The aim was to verify the currently available numerical models for coupled THM processes, improve confidence levels in numerical modelling and deepen understanding to the coupled behaviour of fractured rock-buffer interactions during heating. The BMT was divided into two subtasks: 1) simulation of hydro-mechanical behaviour of the fractured rock mass with respect to the tunnel excavation; and 2) the simulation coupled thermo–hydro–mechanical responses of the complete rock-buffer–heater system during the whole heating period.

The first subtask required predictions to the redistribution of water head field, flow rate field, stress field and deformation field in the rock mass induced by tunnel boring. The numerical models then could be supported and calibrated against monitored data on geological and hydrological characterization of the rock mass surrounding the tunnel, the hydraulic tests carried out before the tunnel excavation.

The second subtask required predictions to responses of buffer and rock mass and their interactions, including temporal evolutions and spatial distributions of temperature, water content, water pressure, stress and deformation of the buffer material and rock mass near the tunnel. The results were compared at selected points. As a global measure of the rock-buffer–heater system, the time history of the total system power input to the heater was also to be predicted. The prediction–calibration cycle could be maintained throughout the BMT to enhance the numerical capability and improve confidence.

Task 2 US DOE's proposed test case

The Drift Scale Test (DST) in the Exploratory Studies Facility (ESF) at Yucca Mountain is a large-scale thermal test, conducted by the Yucca Mountain Site Characterization Office of the U. S. Department of Energy (DOE). It is part of DOE's program of characterizing the Yucca Mountain site to evaluate its suitability for a potential nuclear waste repository. The heating phase of the test, started on December 3, 1997, was scheduled to continue for approximately four years. This was by a cooling phase of another four years and a period of post-test characterization of the test block. Analysis, interpretation and reporting of the results were on going in parallel. The objective of the test was to help increase the confidence in models of coupled thermal–mechanical–hydrological–chemical processes in the rock mass. These models could be employed to quantitatively assess the long-term performance of the potential repository.

Heating was effected through nine cylindrical heaters placed on the floor of a 47.5 meter drift and 50 wing heaters, each 10 m long, inserted into horizontal boreholes into either side-wall of the drift. The purpose of this arrangement was to: (a) simulate the thermal pulse an emplacement drift will experience from its neighbours, and (b) heat a large volume of rock mass to boiling temperatures in a reasonable period of time. Measurements/monitoring made in the DST included:

1. Quantity of heat applied, and temperature distribution based on 3000 sensors.
2. Displacements in the rock by multiple point borehole extensometers; deformation of concrete lining sections by convergence monitors; strain in the concrete sections by strain gauges; acoustic and microseismic emissions.
3. Moisture contents of the rock by neutron logging, electric resistivity tomography and ground penetrating radar.
4. Air pressure, relative humidity, and temperature in packed intervals in boreholes; pneumatic pressure transient testing; gas tracer transport testing.
5. Gas and water sampling to study chemical changes; post-test sampling and analysis.

DOE provided data to interested organizations in DECOVALEX, who could use them to study and test the following kinds of codes and models:

1. Thermohydrological (TH) codes: heat and fluid flow in unsaturated fractured rocks; heat pipe effect and other heat transfer mechanisms; effects of temperature dependence of permeability and conductivity, etc.
2. Thermomechanical (TM) codes: changes in concrete lined drift; changes in the unsaturated rock; comparison between field and laboratory parameters (scale effect).
3. Thermo–hydro–mechanical (THM) codes: processes in unsaturated fractured rocks; including the presence of drifts; effects of thermo–mechanical processes on hydrologic characteristics.
4. Thermo–hydro–chemical (THC) codes: chemical changes under air–water-vapour flow in fractured rock; changes in Eh and pH; chemical reactions under phase change; effects of dissolution and precipitation on hydrologic characteristics.

Task 3 Benchmark Test Problems for Treatment of Coupled T–H–M

The proposed task was based on suggestions from a number of different funding organisations. It consisted of three benchmark test cases (BMTs), which were defined to study how to treat T–H–M couplings when evaluating long-term performance of nuclear waste repositories in complex rock structures. The BMTs were not defined as code-comparison exercises with identical parameters and boundary conditions, but as frameworks from which the research teams must establish, justify and document their model conceptualisation and property/parameter identification according to a common data base from realistic large scale experiments existing today. The main means of judgement was the impact on the chosen performance measures due to the different simplification/idealization and bounding analyses. By this means, experiences by one team could be communicated interactively to the others in the project, thus enabling development of a more well-based procedure for simplification and treatment of THM in PA than would not be possible with just one team analysing the problem.

The selection of BMTs was thought to represent situations of relevance to many national repository programmes, with flexible definitions to reflect desires of different programmes. The methodology of analyses developed when attacking the cases, however, was readily applicable. The following three benchmark tests were suggested: (a) Resaturation BMT, (b) Homogenization BMT and (c) Glaciation BMT.

BMT 1

The Resaturation BMT concerned basically with the resaturation of a hypothetical repository immediately after its closure and in principle, it was defined to include two alternative formations, fractured hard rock and sedimentary rock, to satisfy needs from different national waste repository concepts. The data bases developed at the FEBEX or the Monterri sites, both in Switzerland, could be used for the detailed technical definition of the BMT with alternative repository geometry. The main PA measures were the resaturation progress in buffer and rock, the mechanical effects on buffer and waste form, and the temperature distribution in buffer.

BMT 2

The Homogenization BMT (as originally proposed as upscaling BMT) concerned basically with the relationship between an equivalent continuum (which could be heterogeneous) and detailed discrete representations of fractured rocks, and the extrapolation of rock properties obtained from small scale test and observations to large repository scale, with analysis for uncertainties. The main PA measures were the methods of derivation of flow and deformation properties of the fractured rock from a small detailed model to large scale equivalent continuum model, and its impact on large scale changes of flow and deformability fields. The data base developed at Sellafield for the Task 1 of DECOVALEX II was used for the detailed technical definition of the BMT.

BMT 3

The Glaciation BMT concerned mainly with the hydro-mechanical impacts of a cycle of glaciation and deglaciation on the long term (up to 100,000 years) performance of a hypothetical post-closure repository, without considering the thermal effect. Many different scenarios could be included as alternative contents, such as permafrost, different ice–rock interface conditions, 2D–3D transition, inland/coastal repository locations, sea level changes, saline water intrusion, fracture initiation, propagation and creeping, etc. The main PA measures were the maximum deformation, changes of permeability fields, flow patterns and formation of critical flow paths, ground surface subsidence and rebound. Only long-lasting and large scale changes in PA measures were significant.

For each BMT, discussions focused on: the identification of simplification in geometry and processes; discussion of uncertainties or open questions related to each type of simplification; evaluation on to what extent observations made so far really affects PA; and discussion of next steps of simplification/bounding analyses.

Task 4 Forum and documentation on treatment of T–H–M in Performance Assessment

In order to better understand the relevance of T-H-M coupling to performance assessment (PA), the associated uncertainties and the applicability ranges, the Task 4 was proposed as a platform for presentation, discussion and documentation on the treatment of T–H–M issues in the framework of PA analyses. The task contained two subtasks: i) Task 4a: a state–of–the–art review on the current and past international treatment of T–H–M issues in PA framework and ii) forum and documentation on T–H–M treatment in the PA framework.

Task 4a

The aim of the Task 4a was to assemble works performed or underway in different nuclear waste R&D programmes and evaluate/compile a state–of–the–art review report, using the peer review on the DECOVALEX – II Task 4 report "Coupled THM issues related to repository design and performance" (Stephansson et al., 1999) and its supplement "Examples of treatment of mechanical and thermo–hydro–mechanical issues in some safety assessments" by Andersson (1999), as a start. The common outline format should include: define the coupled process (such as HM) and how they were identified (e.g. through RES, Influence Diagrams or other FEP procedures); what has been done; preliminary conclusions – bounding calculations; uncertainty and sensitivity; and outstanding questions and overall conclusions.

Task 4b

Task 4b was aimed to invite a number of international experts on PA to present on the past and current activities PA analysis, and the associated treatment of T–H–M issues, at all possible workshops. The purpose was to provide the project, especially the research teams, with a broader view on the PA processes and issues involved, so that their studies of other tasks would be performed with more PA perspective. At the end of the project, a thorough and in-depth state–of–the–art report on treatment of T–H–M issues in PA, with inputs from both the presentations of the invited experts and the findings of the research teams of the project regarding all other tasks, should be prepared. A clearly defined and documented consensus on T–H–M processes in PA should be reached by this report.

In the Naantali workshop, October 2001, Dr. Timo Vieno from VTT presented the Finnish approach to PA issues.

The National DECOVALEX III Group

As managed during the previous DECOVALEX projects, (1991–1995 and 1995–1999), STUK decided to establish a forum for the exchange of experiences and discussion between different national organizations and experts. This forum was called The National DECOVALEX III Group (NDG). The Group was open to all who were interested in the task problems of the international project and who wanted to contribute one way or another to the national effort. In recent times it is customary to use electronic mail and internet as much as possible. Thus some members of the national group had never attended the meetings but have given their contributions and observations via E-mail. The following organizations and their representatives have been involved in the national team work:

Helsinki University of Technology, Laboratory of Theoretical and Applied Mechanics (later on Institute of Mathematics):
- professor Martti Mikkola
- professor Rolf Stenberg
- M.Sc. (Tech) Antti Lempinen (until the end of 2001)
- M.Sc. (Tech) Petri Jussila
- M.Sc. (Tech) Tuukka Lahtinen
- M.Sc. (Tech) Juha Hartikainen (later on at the Laboratory of Structural Mechanics).

Helsinki University of Technology, Laboratory of Structural Mechanics:
- professor Jukka Aalto
- M.Sc. (Tech) Juha Hartikainen.

Helsinki University of Technology, Laboratory of Rock Engineering:
- professor Pekka Särkkä
- Dr. Tech. Juha Antikainen
- Dr. Tech. Nuria Marcos.

Uppsala University, Sweden:
- Dr. Tech. Auli Niemi
- M.Sc. Johan Öhman.

VTT, Technical Research Centre of Finland:
- Dr. Tech. Kari Rasilainen
- M.Sc. Antti Poteri.

Ministry of Trade and Industry:
- Lic. Tech. Anne Väätäinen.

Fintact Oy (later JP-Fintact):
- Lic. Tech. Tiina Vaittinen.

Fracom Oy:
- Lic. Tech. Mikael Rinne.

Gridpoint Finland Oy:
- M.Sc. (Tech) Matti Hakala.

Saanio & Riekkola Oy:
- Lic. Tech. Erik Johansson.

Posiva Oy:
- Lic. Tech. Jukka-Pekka Salo.

Fundus Oy:
- Lic. Tech. Jukka Pöllä.

Radiation and Nuclear Safety Authority
- Dr. Tech. Esko Eloranta (chairman)
- Phil. Lic. Kaisa-Leena Hutri.

The group had eight meetings during 1999–2003. The last meeting was held in STUK's premises October 6, 2003. It was at the same time a seminar in the national KYT-programme ("Finnish Research Programme on Nuclear Waste Management").

References

Andersson, J., 1999. Examples of the Treatment of Mechanical and Thermo–Hydro–Mechanical Issues in Some Safety Assessments. SKI Report 99:7, Supplementary Report 2.

Eloranta, E. (ed.), 1996. The international DECOVALEX project for the modelling of coupled Thermo–Hydro–Mechanical processes in a nuclear waste repository. The Finnish contribution during 1991-1995. STUK-YTO-TR 113, Finnish Centre for Radiation and Nuclear Safety (now called Radiation and Nuclear Safety Authority), STUK, Helsinki, Finland.

Eloranta, E. (ed.), 2000. DECOVALEX II. The summary reposrt of the Finnish contributions 1995–1999. STUK-YTO-TR 163, Radiation and Nuclear Safety Authority, STUK, Helsinki, Finland.

Lahtinen, T., 2002. Ydinjätteen kapselisijoituksen mekaanisen stabiiliuden laskentamenetelmä. (Calculation Method for the Mechanical Stability of Nuclear Waste Canister Disposal). (in Finnish with an English abstract). Master's thesis at Helsinki University of Technology, Department of Engineering Physics and Mathematics, 75 p.

Stephansson, O., Hudson, J.A., Tsang, C.-F., Jing, L., and Andersson, J., 1999. DECOVALEX II PROJECT, Coupled THM Issues Related to Repository Design and Performance – Task 4. SKI Report 99:7.

The Finnish contributions included in the present report

Appendix I, the work by Petri Jussila on FEBEX experiment (Task 1)

Appendix II, the work by Auli Niemi, Johan Öhman and Juha Antikainen (Task 3, BMT 2)

Appendix III, the work by Juha Antikainen on rock mechanics (Task 3, BMT 2)

Appendix IV, the work by Juha Hartikainen on permafrost issues (Task 3, BMT 3)

DECOVALEX III – TASK 1, PART B
MODELLING REPORT BY STU

Petri Jussila
Helsinki University of Technology
Institute of Mathematics
P.O.Box 1100 Fin-02015 HUT Finland
October 2003

Table of Contents

Introduction

A buffer of compacted bentonite clay is planned to be used to prevent the movement of groundwater and the consequential transport of material from a geological repository for spent nuclear fuel. Fluid flow, phase changes, mechanical behaviour of the buffer, rock, and the waste canisters, and the heat produced by the waste constitute a coupled thermohydro-mechanical system. The aim of the study is to derive a general thermodynamically consistent thermohydromechanical model for an arbitrary mixture. The general theory is applied to the thermohydraulic modelling of a mixture of compacted bentonite, liquid water, vapour, and air.

The model describes the behaviour of the mixture via proper choices of free energy and dissipation function. The behaviour of the system originates from the individual behaviours of the components and from their mutual interactions. The free energy of the system is chosen to take into account the interaction of the mixture components through adsorption, vaporisation, and mixing of the gaseous components. The choice is based on the equilibrium conditions for the water species in different combinations of the components.

The model is fitted to a suction experiment for Febex bentonite and applied to the thermohydraulic simulation of the bentonite buffer of the Febex in situ test. The approach is to describe the essential features of the thermohydraulic behaviour of the buffer in a simple 1D geometry. The results calculated with FEM are compared to the measurements.

The general model

Basic concepts

The considered system consists of solid skeleton (s), liquid water (l), water vapour (v), and dry air (a). Vapour and air occupy the same gaseous (g) volume fraction. The volume fraction β_j [-] of the phase j is the ratio of its volume and the representative elementary volume V, i.e.,

$$\beta_\mathrm{j} = \frac{V_\mathrm{j}}{\sum_\mathrm{j} V_\mathrm{j}} = \frac{V_\mathrm{j}}{V}, \quad \mathrm{j} \in \{\mathrm{s, l, g}\}. \tag{1}$$

The molar fraction x_k [-] of component k is the ratio of the mole number n_k [mol] of the component k and the number of moles occupying the same volume fraction

$$x_\mathrm{k} = \frac{n_\mathrm{k}}{n_\mathrm{a} + n_\mathrm{v}}, \mathrm{k} \in \{\mathrm{a, v}\}; \quad x_\mathrm{k} = 1, \mathrm{k} \in \{\mathrm{s, l}\}. \tag{2}$$

The molar volume fraction ξ_k [-] of component k is the product of the molar fraction and the volume fraction occupied by the component

$$\xi_\mathrm{k} = \beta_\mathrm{g} x_\mathrm{k}, \mathrm{k} \in \{\mathrm{a, v}\}; \quad \xi_\mathrm{k} = \beta_\mathrm{k}, \mathrm{k} \in \{\mathrm{s, l}\}. \tag{3}$$

Apparently we have $\sum_{\mathrm{k}\in\{\mathrm{s, l, v, a}\}} \xi_\mathrm{k} = 1$. The molar volume fractions relate the apparent densities $\rho_\mathrm{k} = m_\mathrm{k}/V$ [kg/m^3] to the bulk densities $\bar{\rho}_\mathrm{k} = m_\mathrm{k}/\left(x_\mathrm{k} V_\mathrm{j}\right)$, for which j = g for k∈{a, v} and j = k for k∈{s, l} by $\rho_\mathrm{k} = \xi_\mathrm{k} \bar{\rho}_\mathrm{k}$.

We also define porosity $\eta = 1 - \xi_\mathrm{s}$, liquid saturation $\chi = \xi_\mathrm{l}/(1 - \xi_\mathrm{s})$, and vapour fraction $\zeta = \xi_\mathrm{v}/(\xi_\mathrm{a} + \xi_\mathrm{v})$ as alternative variables, by means of which the molar volume fractions of the components s, l, v, and a are expressed by $\xi_\mathrm{s} = 1 - \eta$, $\xi_\mathrm{l} = \eta\chi$, $\xi_\mathrm{v} = \eta(1 - \chi)\zeta$, and $\xi_\mathrm{a} = \eta(1 - \chi)(1 - \zeta)$, respectively.

The absolute velocity of the component k is denoted by $\mathbf{U}_\mathrm{k}$ [m/s] and a relative velocity by $\mathbf{V}_\mathrm{k} = \mathbf{U}_\mathrm{k} - \mathbf{U}_*$, where $\mathbf{U}_*$ is a reference velocity. The material time derivative is $d^\mathrm{k}/dt = \partial/\partial t + \mathbf{U}_\mathrm{k} \cdot \nabla$. Tensors can be divided into deviatoric and spherical parts, e.g., the Cauchy stress tensor [Pa] of component k is $\boldsymbol{\sigma}_\mathrm{k} = \boldsymbol{\sigma}'_\mathrm{k} + \mathrm{tr}(\boldsymbol{\sigma}_\mathrm{k})/3 = \boldsymbol{\sigma}'_\mathrm{k} - p_\mathrm{k}\mathbf{I}$, where p_k is the pressure. Strain $\boldsymbol{\varepsilon}_\mathrm{k}$ [-] and rate of deformation $\mathbf{D}_\mathrm{k}$ [1/s] of component k, respectively, are defined by

$$\boldsymbol{\varepsilon}_\mathrm{k} = \frac{1}{2}\left[\nabla \mathbf{u}_\mathrm{k} + (\nabla \mathbf{u}_\mathrm{k})^T\right], \quad \mathbf{D}_\mathrm{k} = \frac{1}{2}\left[\nabla \mathbf{U}_\mathrm{k} + (\nabla \mathbf{U}_\mathrm{k})^T\right], \tag{4}$$

where $\mathbf{u}_\mathrm{k}$ [m] is the displacement of component k.

Thermodynamic state of the system

The thermodynamic state of the system is uniquely characterised by the state variables. In the general model they are chosen to be the molar volume fractions ξ_k, intrinsic densities $\overline{\rho}_\mathrm{k}$, and strains $\boldsymbol{\varepsilon}_\mathrm{k}$ of the components, and the common temperature T. The specific thermodynamic potentials are functions of the state variables. The indicator function taking care of the restriction for the molar volume fractions is

$$I\left(\xi_\mathrm{s},\xi_\mathrm{l},\xi_\mathrm{v},\xi_\mathrm{a}\right)=\begin{cases}0, & \left(\xi_\mathrm{s},\xi_\mathrm{l},\xi_\mathrm{v},\xi_\mathrm{a}\right)\in C,\\ +\infty, & \text{otherwise,}\end{cases} \tag{5}$$

where

$$C=\left\{\left(\xi_\mathrm{s},\xi_\mathrm{l},\xi_\mathrm{v},\xi_\mathrm{a}\right)\in\mathbb{R}^4\,\middle|\,\sum_\mathrm{k}\xi_\mathrm{k}=1,\ \xi_\mathrm{k}\geq 0,\ \mathrm{k}\in\{\mathrm{s,\ l,\ v,\ a}\}\right\}. \tag{6}$$

The free energy [J/m^3] of the system is

$$\psi=\sum_{\mathrm{k}\in\{\mathrm{s,\ l,\ v,\ a}\}}\rho_\mathrm{k}\psi_\mathrm{k}=\sum_{\mathrm{k}\in\{\mathrm{s,\ l,\ v,\ a}\}}\rho_\mathrm{k}\tilde{\psi}_\mathrm{k}+TI\left(\xi_\mathrm{s},\xi_\mathrm{l},\xi_\mathrm{v},\xi_\mathrm{a}\right), \tag{7}$$

where $\tilde{\psi}_\mathrm{k}$ [J/kg] is the specific free energy of component k without the restriction involved in (6). The dissipative behaviour of the system is characterised by the dissipative variables, which in the general work are chosen to be the rates of deformation $\mathbf{D}_\mathrm{k}$, the heat flux vectors $\mathbf{q}_\mathrm{k}$ [W/m^2], and the relative velocities $\mathbf{V}_\mathrm{k}$. The dissipation function ϕ [W/m^3] is a function of the state variables and the dissipative variables

$$\phi=\phi\left(\xi_\mathrm{k},\overline{\rho}_\mathrm{k},\boldsymbol{\varepsilon}_\mathrm{k},T,\mathbf{D}_\mathrm{k},\mathbf{q}_\mathrm{k},\mathbf{V}_\mathrm{k}\right),\quad \mathrm{k}\in\{\mathrm{s,\ l,\ v,\ a}\}. \tag{8}$$

Fundamental laws for an arbitrary mixture

The conservation law of mass by means of the rate of production of mass θ_k [kg/(m^{3}s)] is

$$\sum_\mathrm{k}\theta_\mathrm{k}=0,\quad \theta_\mathrm{k}=\frac{\partial\rho_\mathrm{k}}{\partial t}+\nabla\cdot\left(\rho_\mathrm{k}\mathbf{U}_\mathrm{k}\right). \tag{9}$$

The conservation law of linear momentum by means of the rate of production of the linear momentum $\mathbf{m}_\mathrm{k}$ [N/m^3] of component k is

$$\sum_\mathrm{k}\mathbf{m}_\mathrm{k}=0,\quad \mathbf{m}_\mathrm{k}=\rho_\mathrm{k}\frac{d^\mathrm{k}\mathbf{U}_\mathrm{k}}{dt}+\theta_\mathrm{k}\mathbf{U}_\mathrm{k}-\nabla\cdot\boldsymbol{\sigma}_\mathrm{k}-\rho_\mathrm{k}\mathbf{g}, \tag{10}$$

where $\mathbf{g}$ [N/m^3] is the gravitational acceleration vector. The conservation law of energy by means of the rate of production of thermal energy l_k [W/m^3] is

$$\begin{aligned}&\sum_\mathrm{k}l_\mathrm{k}=0,\\ &l_\mathrm{k}=\rho_\mathrm{k}\frac{d^\mathrm{k}e_\mathrm{k}}{dt}+\left(e_\mathrm{k}-\frac{1}{2}\mathbf{U}_\mathrm{k}\cdot\mathbf{U}_\mathrm{k}\right)\theta_\mathrm{k}-\boldsymbol{\sigma}_\mathrm{k}:\nabla\mathbf{U}_\mathrm{k}+\mathbf{m}_\mathrm{k}\cdot\mathbf{U}_\mathrm{k}+\nabla\cdot\mathbf{q}_\mathrm{k}-r_\mathrm{k}\,.\end{aligned} \tag{11}$$

where e_k [J/kg] is the specific internal energy and r_k [W/m^3] is the thermal energy source. For the rate of production of entropy γ_k [W/(m^{3}K)] by component k we have

$$T\gamma_k = \boldsymbol{\sigma}_k : \nabla \mathbf{U}_k - \rho_k \left(\frac{d^k \psi_k}{dt} + s_k \frac{d^k T}{dt} \right) - \left(\psi_k - \frac{1}{2} \mathbf{U}_k \cdot \mathbf{U}_k \right) \theta_k - \\ - \mathbf{m}_k \cdot \mathbf{U}_k - \frac{\nabla T}{T} \cdot \mathbf{q}_k + l_k , \tag{12}$$

where s_k [J/(kg K)] is the specific entropy. The entropy inequality for the system is

$$\sum_k \gamma_k \geq 0 . \tag{13}$$

General constitutive relations

Following the procedure introduced by Hartikainen and Mikkola (1997), we use the principle of maximal rate of entropy production (Ziegler, 1977; Ziegler and Wehrli, 1988) and define the dissipation function as $\phi = \sum_k T\gamma_k$, with the orthogonality relation

$$\phi = \nu \sum_k \left[\left(\partial\phi / \partial \mathbf{D}'_k \right) : \mathbf{D}'_k + \left(\partial\phi / \partial \left(\mathrm{tr}\mathbf{D}_k \right) \right) \mathrm{tr}\mathbf{D}_k + \left(\partial\phi / \partial \mathbf{q}_k \right) \cdot \mathbf{q}_k + \left(\partial\phi / \partial \mathbf{V}_k \right) \cdot \mathbf{V}_k \right],$$

where

$$\nu = \phi \sum_k \left[\left(\partial\phi / \partial \mathbf{D}'_k \right) : \mathbf{D}'_k + \left(\partial\phi / \partial \left(\mathrm{tr}\mathbf{D}_k \right) \right) \mathrm{tr}\mathbf{D}_k + \left(\partial\phi / \partial \mathbf{q}_k \right) \cdot \mathbf{q}_k + \left(\partial\phi / \partial \mathbf{V}_k \right) \cdot \mathbf{V}_k \right]^{-1} .$$

What is new in the present work is the inclusion of the intrinsic densities as state variables. The result is the following general constitutive relations

$$\boldsymbol{\sigma}'_k = \rho_k \frac{\partial \tilde{\psi}_k}{\partial \boldsymbol{\varepsilon}'_k} + \nu \frac{\partial \phi}{\partial \mathbf{D}'_k} , \tag{14}$$

$$p_k = -\rho_k \frac{\partial \tilde{\psi}_k}{\partial \left(\mathrm{tr}\boldsymbol{\varepsilon}_k \right)} - \nu \frac{\partial \phi}{\partial \left(\mathrm{tr}\mathbf{D}_k \right)} + p_k^{\mathrm{th}} , \tag{15}$$

$$s_k = -\frac{\partial \tilde{\psi}_k}{\partial T} - \frac{I}{\overline{\rho}_k} , \tag{16}$$

$$-\frac{\nabla T}{T} = \nu \frac{\partial \phi}{\partial \mathbf{q}_k} , \tag{17}$$

$$-\mathbf{m}_k - \sum_j \left(\rho_k \frac{\partial \tilde{\psi}_k}{\partial \xi_j} + \xi_k \hat{B}_j \right) \nabla \xi_j + \sum_j \left(\rho_j \frac{\partial \tilde{\psi}_j}{\partial \xi_k} + \xi_j \hat{B}_k \right) \nabla \xi_k = \nu \frac{\partial \phi}{\partial \mathbf{V}_k} , \tag{18}$$

$$p_k^{\mathrm{th}} = \xi_k \overline{\rho}_k^2 \frac{\partial \tilde{\psi}_k}{\partial \overline{\rho}_k} - \xi_k T I , \tag{19}$$

$$G_q - G_p = 0 , \tag{20}$$

where

$$p_k^{\mathrm{th}} = \xi_k \left(\hat{B}_k + \sum_j \rho_j \frac{\partial \tilde{\psi}_j}{\partial \xi_k} \right) \tag{21}$$

is the relative thermodynamical pressure [Pa] of component k, $\hat{B}_{\mathrm{k}}$ [Pa] is a pressure term

$$\left(\hat{B}_{\mathrm{s}}, \hat{B}_{\mathrm{l}}, \hat{B}_{\mathrm{v}}, \hat{B}_{\mathrm{a}}\right) \in T\partial I\left(\xi_{\mathrm{s}}, \xi_{1}, \xi_{\mathrm{v}}, \xi_{\mathrm{a}}\right) \tag{22}$$

arising from the restriction involved in (6) and for which we have $\hat{B}_{\mathrm{s}} = \hat{B}_{\mathrm{l}} = \hat{B}_{\mathrm{v}} = \hat{B}_{\mathrm{a}} = \hat{B}$. The generalised specific Gibbs function [J/kg] of component k is

$$G_{\mathrm{k}} = \tilde{\psi}_{\mathrm{k}} - \frac{1}{2}\mathbf{U}_{\mathrm{k}} \cdot \mathbf{U}_{\mathrm{k}} + \frac{p_{\mathrm{k}}^{\mathrm{th}}}{\rho_{\mathrm{k}}}. \tag{23}$$

Thermohydraulic model for bentonite

Constitution

The general model is applied to thermohydraulic modelling of bentonite buffer for which the solid component is represented by a rigid clay skeleton. We get the constitution from the general constitutive relations (14)-(23) with appropriate choices of the free energies and the dissipation function. The chosen specific free energies of the components are the following

$$\psi_{\mathrm{s}}\left(T,\bar{\rho}_{\mathrm{s}},\xi_{\mathrm{j}}\right)=-c_{\mathrm{s}}T\ln\frac{T}{T_0}+\frac{T}{\bar{\rho}_{\mathrm{s}}}I\left(\xi_{\mathrm{j}}\right), \tag{24}$$

$$\psi_{\mathrm{l}}\left(T,\bar{\rho}_{\mathrm{l}},\xi_{\mathrm{j}}\right)=-c_{\mathrm{l}}T\ln\frac{T}{T_0}+\frac{RT}{M_{\mathrm{v}}}h\left(\xi_{\mathrm{s}},\xi_{\mathrm{l}}\right)+\frac{T}{\bar{\rho}_{\mathrm{l}}}I\left(\xi_{\mathrm{j}}\right), \tag{25}$$

$$\psi_{\mathrm{v}}\left(T,\bar{\rho}_{\mathrm{v}},\xi_{\mathrm{j}}\right)=-c_{\mathrm{v}}T\ln\frac{T}{T_0}+\frac{RT}{M_{\mathrm{v}}}\ln\frac{\bar{\rho}_{\mathrm{v}}}{\bar{\rho}_{\mathrm{v},0}}+f\left(T\right)+\frac{RT}{M_{\mathrm{v}}}g_{\mathrm{v}}\left(\xi_{\mathrm{j}}\right)+\frac{T}{\bar{\rho}_{\mathrm{v}}}I\left(\xi_{\mathrm{j}}\right), \tag{26}$$

$$\psi_{\mathrm{a}}\left(T,\bar{\rho}_{\mathrm{a}},\xi_{\mathrm{j}}\right)=-c_{\mathrm{a}}T\ln\frac{T}{T_0}+\frac{RT}{M_{\mathrm{a}}}\ln\frac{\bar{\rho}_{\mathrm{a}}}{\bar{\rho}_{\mathrm{a},0}}+\frac{RT}{M_{\mathrm{a}}}g_{\mathrm{a}}\left(\xi_{\mathrm{j}}\right)+\frac{T}{\bar{\rho}_{\mathrm{a}}}I\left(\xi_{\mathrm{j}}\right), \tag{27}$$

where c_{k} [J/(kg K)] is the specific heat at constant volume, M_{k} [kg/mol] is the molar weight, R [J/(mol K)] is the universal gas constant, f [J/kg] is a vaporisation function, h [-] is an adsorption function related to the interaction of solid and liquid, g_{k} [-] is a mixing interaction function for the gaseous components (k ∈ {a, v}), and $\bar{\rho}_{\mathrm{k},0}$ [kg/m^3] is the intrinsic density at the reference state $\left(P,T\right)=\left(P_0,T_0\right)$, where P [Pa] is the mixture pressure. The chosen adsorption function is

$$h\left(\xi_{\mathrm{s}},\xi_{\mathrm{l}}\right)=b\left(\frac{\xi_{\mathrm{s}}}{\xi_{\mathrm{l}}}-\frac{1}{\chi_{\max}}\frac{1-\eta_0}{\eta_0}\right)^2=a\left(\frac{1}{\chi}-\frac{1}{\chi_{\max}}\right)^2, \tag{28}$$

where $\chi_{\max}$ [-] is the maximum saturation, η_0 is the porosity at the reference state, and $a=b\left(\left(1-\eta_0\right)/\eta_0\right)^2$ is a constant material parameter to be determined from the experiments. The chosen mixing terms are

$$\begin{aligned} g_{\mathrm{v}}\left(\xi_{\mathrm{v}},\xi_{\mathrm{a}}\right)&=\ln\left(\frac{\xi_{\mathrm{v}}}{\xi_{\mathrm{a}}+\xi_{\mathrm{v}}}\Big/\frac{\xi_{\mathrm{v},0}}{\xi_{\mathrm{a},0}+\xi_{\mathrm{v},0}}\right)=\ln\frac{\zeta}{\zeta_0},\\ g_{\mathrm{a}}\left(\xi_{\mathrm{v}},\xi_{\mathrm{a}}\right)&=\ln\left(\frac{\xi_{\mathrm{a}}}{\xi_{\mathrm{a}}+\xi_{\mathrm{v}}}\Big/\frac{\xi_{\mathrm{a},0}}{\xi_{\mathrm{a},0}+\xi_{\mathrm{v},0}}\right)=\ln\frac{1-\zeta}{1-\zeta_0}. \end{aligned} \tag{29}$$

The dissipation function is chosen to be

$$\begin{aligned} \phi=&\sum_{\mathrm{k}\in\{\mathrm{s,l,v,a}\}}\frac{1}{\xi_{\mathrm{k}}\lambda_{\mathrm{k}}T}\mathbf{q}_{\mathrm{k}}\cdot\mathbf{q}_{\mathrm{k}}+\sum_{\mathrm{k}\in\{\mathrm{l,g}\}}\frac{\mu_{\mathrm{k}}}{k_{\mathrm{k}}}\left(\beta_{\mathrm{k}}\mathbf{V}_{\mathrm{k}}\right)\cdot\left(\beta_{\mathrm{k}}\mathbf{V}_{\mathrm{k}}\right)+\\ &+\bar{\rho}_{\mathrm{v}}\frac{RT}{M_{\mathrm{v}}}\frac{1}{D}\frac{\beta_{\mathrm{g}}}{\zeta\left(1-\zeta\right)}\left(\zeta\mathbf{V}_{\mathrm{vg}}\right)\cdot\left(\zeta\mathbf{V}_{\mathrm{vg}}\right), \end{aligned} \tag{30}$$

where λ_k [W/(Km)] is the heat conductivity, μ_k [kg/(sm)] is the dynamic viscosity, k_k [m^2] is the permeability, D [m^2/s] is the diffusivity, $\mathbf{V}_g = \zeta \mathbf{V}_v + (1-\zeta)\mathbf{V}_a$ is the molar weighted velocity of gas for which $\beta_g \mathbf{V}_g = \xi_v \mathbf{V}_v + \xi_a \mathbf{V}_a$, and $\mathbf{V}_{vg} = \mathbf{V}_v - \mathbf{V}_g$ is the relative velocity of vapour with respect to the molar weighted velocity of gas.

The pressures get the form

$$p_k = \xi_k \left(\hat{B} + \bar{\rho}_l \frac{RT}{M_v} \xi_l \frac{\partial h}{\partial \xi_k} \right). \tag{31}$$

The total stress of the system in the absence of the deviatoric components is

$$\boldsymbol{\sigma} = \sum_{k \in \{s,\, l,\, v,\, a\}} \boldsymbol{\sigma}_k = - \sum_{k \in \{s,\, l,\, v,\, a\}} p_k \mathbf{I} = -\hat{B}\mathbf{I}. \tag{32}$$

Consequently, the pressure term $\hat{B} = P$ is actually the mixture pressure. For air and vapour we get the ideal gas state equations

$$p_k = \rho_k \frac{RT}{M_k}, \quad k \in \{a,\, v\}. \tag{33}$$

The Darcy laws for liquid and gas, respectively, become

$$\beta_l \mathbf{V}_l = -\frac{k_l}{\mu_l} \left[\nabla \left(\frac{p_l}{\xi_l} \right) - \bar{\rho}_l \mathbf{g} + \bar{\rho}_l \frac{RT}{M_v} \nabla h \right], \quad \beta_g \mathbf{V}_g = -\frac{k_g}{\mu_g} \left[\nabla P - \frac{\rho_a + \rho_v}{\beta_g} \mathbf{g} \right]. \tag{34}$$

The Fick law for the relative velocity of vapour becomes

$$\zeta \mathbf{V}_{vg} = -D \left[\nabla \zeta - \zeta (1-\zeta) \frac{M_v - M_a}{RT} \mathbf{g} \right]. \tag{35}$$

The Fourier heat conduction law gets the usual form

$$\mathbf{q}_k = -\xi_k \lambda_k \nabla T, \tag{36}$$

and the specific internal energies are

$$\begin{aligned} e_k &= c_k T, \quad k \in \{s,\, l,\, a\}, \\ e_v &= c_v T + f(T) - T \frac{df(T)}{dT}. \end{aligned} \tag{37}$$

Interaction of the components

Interactions of the components are studied by considering equilibrium of the water species in different mixtures, i.e., “inside” and “outside” the porous medium.

Vaporisation and mixing of gases are covered by considering a mixture of liquid, vapour, and air with the water species in equilibrium outside the porous medium, i.e.,

$$G_v^0 = G_l^0, \tag{38}$$

where

$$
\begin{aligned}
G_{\mathrm{v}}^{0} &= -c_{\mathrm{v}} T \ln\frac{T}{T_0} + \frac{RT}{M_{\mathrm{v}}} \ln\frac{\bar{\rho}_{\mathrm{v}}^{0}}{\bar{\rho}_{\mathrm{v},0}} + f\left(T\right) + \frac{RT}{M_{\mathrm{v}}} \ln\frac{\zeta^{0}}{\zeta_0} + \frac{P^{0}}{\bar{\rho}_{\mathrm{v}}^{0}}, \\
G_{\mathrm{l}}^{0} &= -c_{\mathrm{l}} T \ln\frac{T}{T_0} + \frac{P^{0}}{\bar{\rho}_{\mathrm{l}}}.
\end{aligned}
\tag{39}
$$

We choose the phase change interaction function to be

$$
f(T) = -\frac{RT}{M_{\mathrm{v}}} - L_0 \frac{T - T_0}{T_0}, \tag{40}
$$

which yields the latent heat of vaporisation [J/kg] as $L\left(T\right) = L_0 + \left(c_{\mathrm{v}} + R/M_{\mathrm{v}} - c_{\mathrm{l}}\right)T$ and the Clausius-Clapeyron equation outside the porous medium

$$
\ln\frac{\zeta^{0} P^{0}}{\zeta_0 P_0} = \frac{M_{\mathrm{v}}}{RT}\left[L_0 \frac{T - T_0}{T_0} + \left(c_{\mathrm{v}} + \frac{R}{M_{\mathrm{v}}} - c_{\mathrm{l}} \right) T \ln\frac{T}{T_0} \right], \tag{41}
$$

where $\left(\zeta^{0} P^{0}\right)/\left(\zeta_0 P_0\right)$ is the ratio of the partial pressure of saturated vapour from the gaseous phase outside the porous medium at $\left(P^{0}, T\right)$ to the value of the same quantity at the reference state $\left(P_0, T_0\right)$. The result is equivalent to the result for the conventional equilibrium conditions for ideal vapour with the following assumptions

$$
c_{\mathrm{l}}^{p} = c_{\mathrm{l}}, \quad c_{\mathrm{v}}^{p} = c_{\mathrm{v}} + R/M_{\mathrm{v}}, \tag{42}
$$

$$
L(T) = L\left(T_0\right) + \left(c_{\mathrm{v}}^{p} - c_{\mathrm{l}}^{p}\right)\left(T - T_0\right) = L_0 + \left(c_{\mathrm{v}}^{p} - c_{\mathrm{l}}^{p}\right)T, \tag{43}
$$

where c_{k}^{p} [J/(kg K)] is the specific heat at constant pressure.

Adsorption interaction is covered by considering a mixture of solid, liquid, vapour, and air. In this case the Gibbs equilibrium between liquid and vapour is

$$
G_{\mathrm{v}} = G_{\mathrm{l}}, \tag{44}
$$

where

$$
\begin{aligned}
G_{\mathrm{v}} &= -c_{\mathrm{v}} T \ln\frac{T}{T_0} + \frac{RT}{M_{\mathrm{v}}} \ln\frac{\bar{\rho}_{\mathrm{v}}}{\bar{\rho}_{\mathrm{v},0}} + f\left(T\right) + \frac{RT}{M_{\mathrm{v}}} \ln\frac{\zeta}{\zeta_0} + \frac{p_{\mathrm{v}}}{\rho_{\mathrm{v}}}, \\
G_{\mathrm{l}} &= -c_{\mathrm{l}} T \ln\frac{T}{T_0} + \frac{RT}{M_{\mathrm{v}}} h + \frac{p_{\mathrm{l}}}{\rho_{\mathrm{l}}}.
\end{aligned}
\tag{45}
$$

By using the constitution (31) for the pressures, we get the Clausius-Clapeyron equation inside the porous medium to be

$$
\ln\frac{\zeta P}{\zeta_0 P_0} = \frac{M_{\mathrm{v}}}{RT}\left[L_0 \frac{T - T_0}{T_0} + \left(c_{\mathrm{v}}^{p} - c_{\mathrm{l}}^{p} \right) T \ln\frac{T}{T_0} \right] + h + \xi_{\mathrm{l}} \frac{\partial h}{\partial \xi_{\mathrm{l}}}, \tag{46}
$$

where $\left(\zeta P\right)/\left(\zeta_0 P_0\right)$ is the ratio of the partial pressure of saturated vapour of the gaseous phase inside the porous medium at $\left(P, T, \xi_{\mathrm{l}}\right)$ to the value of the same quantity at the reference state $\left(P_0, T_0\right)$ outside the porous medium.

The conventional Kelvin law for the suction pressure p_c [Pa] by means of the relative humidity *RH* [-] is

$$p_c = -\overline{\rho}_l \frac{RT_0}{M_v} \ln RH \,. \tag{47}$$

By combining the Gibbs equilibria outside (38) and inside (44) the porous medium at the same temperature we get for the relative humidity inside the porous medium

$$\ln RH = \ln\left(\frac{\zeta P}{\zeta^0 P^0}\right) = \ln\left(\frac{\zeta}{\zeta^0}\right) = h + \xi_l \frac{\partial h}{\partial \xi_l} \,. \tag{48}$$

From (48) and (47) we get the Kelvin suction pressure by means of the adsorption function as

$$p_c = -\overline{\rho}_l \frac{RT_0}{M_v}\left(h + \xi_l \frac{\partial h}{\partial \xi_l}\right), \tag{49}$$

which form is presented also by Frémond and Nicolas (1990) and by Nicolas (1989 and 1992). The parameter fitting is done by exploiting the Febex experiments in which the psychrometric data for the Kelvin suction pressure is given as a function of the water content. With the adsorption function (28) the Kelvin suction pressure (49) gets the form

$$p_c = \overline{\rho}_l \frac{RT_0}{M_v} a\left(\frac{1}{\chi^2} - \frac{1}{\chi^2_{\max}}\right). \tag{50}$$

In the Febex project the measurements for the low range of suction for confined bentonite have been fitted by means of a van Genuchten type expression. The Febex data used here correspond to the wetting experiment of a confined sample with the dry density range of ρ_{dry} = 1600…1650 kg/m^3. The Kelvin suction curves by means of our model (50) and the Febex model are plotted in Figure 1 for the range of $\chi \in$ [0.5, 1.0]. The used parameter values are given in Table 1.

The thermohydraulic model

By neglecting inertial terms we get the following conservation equations from (9)-(11). The state variables are chosen to be liquid water saturation χ, temperature T, and vapour fraction ζ. The total pressure is assumed to be constant $P = P_0$, and gravitation is neglected. The model consists of the conservation of the mass of the water species,

$$\frac{\partial}{\partial t}\left(\rho_l + \rho_v\right) + \nabla \cdot \left[\overline{\rho}_l \xi_l \mathbf{V}_l + \overline{\rho}_v \xi_v \mathbf{V}_v\right] = 0 \tag{51}$$

and the thermal energy conservation

$$c\frac{\partial T}{\partial t} - \left(e_v - e_l\right)\left(\frac{\partial \rho_l}{\partial t} + \nabla \cdot \left(\overline{\rho}_l \xi_l \mathbf{V}_l\right)\right) + \nabla \cdot \mathbf{q} = 0 \,, \tag{52}$$

where $c = \sum_k \rho_k c_k$.

The constitutive relations are reduced to the Clausius-Clapeyron equation

$$\ln\frac{\zeta}{\zeta_0}=\frac{M_\mathrm{v}}{RT}\left[L_0\frac{T-T_0}{T_0}+\left(c_\mathrm{v}^p-c_\mathrm{l}^p\right)T\ln\frac{T}{T_0}\right]-a\left(\frac{1}{\chi^2}-\frac{1}{\chi_\mathrm{max}^2}\right), \tag{53}$$

vapour state equation

$$P_0=\bar{\rho}_\mathrm{v}\frac{RT}{M_\mathrm{v}}, \tag{54}$$

Darcy's law for liquid

$$\xi_\mathrm{l}\mathbf{V}_\mathrm{l}=\frac{k_\mathrm{l}}{\mu_\mathrm{l}}\bar{\rho}_\mathrm{l}\frac{R}{M_\mathrm{v}}2a\frac{1}{\chi^3}\left[\chi\left(1-\chi/\chi_\mathrm{max}\right)\nabla T-T\nabla\chi\right], \tag{55}$$

Fick's law for vapour, which yields

$$\xi_\mathrm{v}\mathbf{V}_\mathrm{v}=-\beta_\mathrm{g}D\nabla\zeta, \tag{56}$$

Fourier's law for heat flow

$$\mathbf{q}=\sum_\mathrm{k}\mathbf{q}_\mathrm{k}=-\sum\nolimits_\mathrm{k}\xi_\mathrm{k}\lambda_\mathrm{k}\nabla T\equiv-\lambda\nabla T, \tag{57}$$

and to the internal energy difference of the water species

$$e_\mathrm{v}-e_\mathrm{l}=L\left(T_0\right)+\left(c_\mathrm{v}^p-c_\mathrm{l}^p\right)\left(T-T_0\right), \tag{58}$$

which in the case of constant pressure equals to the enthalpy difference, i.e., the latent heat. In addition, the relation between saturation and relative humidity is given by equation (48).

Thermohydraulic simulation of the Febex in situ test

General

The Febex in situ experiment is a part of a multi-task program to investigate the near-field behavior of high level waste repository in crystalline rock. The experiment is based on the Spanish reference concept for disposal, in which the waste canisters are placed in horizontal drifts and surrounded by a barrier of highly-compacted bentonite. In the test, cylindrical heaters simulate the heat production of the waste canisters.

The thermohydraulic behaviour of the Febex in situ test buffer (see Figures 2 and 3) are simulated in 1D domain of $r\in[R_1, R_2]$ = [0.485, 1.14] m considering the bentonite buffer as the only material present. The simulation covers the radial distributions of relative humidity and temperature for the sections E1 and E2 in the directions RD1, RD2, RD3, and RD4, and the evolutions of relative humidity and temperature in 3 points (E1H, E1C, and E1G) of section E1 in the direction RD4.

The initial condition for saturation is χ_init = 0.54 and the constant porosity is η_0 = 0.45. These correspond to the values w = 14.4 % of the gravimetric water content, ρ_dry = 1690 kg/m^3 of the dry density, and RH_0 = 38 % of the initial relative humidity. The initial value for the temperature is that of the surrounding rock, i.e., T_init = T_r = 12 $^\mathrm{o}$C.

The simulated sequence consists of three periods: 1) days between –180…0 d corresponding to the period between the construction of the system and the starting of the heaters, 2) days between 0…53 d corresponding to the heater adjustment period, and 3) days between 53…1000 d corresponding to the period of controlled heating during which the temperature of the hottest point on each heater is kept at 100 °C.

1. Between –180…0 d the buffer saturates isothermally at $T = T_r$. It is assumed that, on average, the system has been fully constructed for six months before day 0. The boundary conditions for saturation are no-flow of moisture $\rho_l \mathbf{V}_l + \rho_v \mathbf{V}_v = 0$ at the heater $r = R_1$ and full saturation $\chi = \chi_{max}$ at the rock $r = R_2$, respectively.

2. The heater adjustment during the period between 0…53 d is approximated by a linear increase of heater temperature from the initial value of 12 °C to the final value assessed by the measured results for each case. The calibrated values in both the directions RD3 and RD4 are $T(R_1)$ = 93 °C and 96 °C for the sections E1 and E2, respectively, $T(R_1)$ = 99 °C in the direction RD2 for both the sections E1 and E2, and $T(R_1)$ = 80 °C in the direction RD1 for both the sections E1 and E2. The temperature boundary condition at the rock $r = R_2$ is of the Robin type $\mathbf{q} \cdot \mathbf{n} = H(T - T_r)$ with the calibrated value H = 1.9 W/(m^{2}K) of the heat transfer coefficient. The boundary conditions for saturation are the same as for the period 1.

3. The period between 53…1000 d is simulated by keeping the heater temperature $T(R_1)$ constant for each considered section and direction as explained above for period 2. The other boundary conditions are the same as for the period 2.

The results for the fully coupled system are calculated by the Finite Element Method program ELMER (CSC, 2003) in co-operation with the Finnish IT Center for Science. The 1D mesh consists of 41 equally spaced nodes and 40 linear elements. A constant time step of 1 d is used for every considered case.

Parameters

For specific heat of the solid phase and for heat conductivity and liquid permeability of the bentonite, respectively, the following empirical relations are employed

$$\begin{aligned} c_s &= 1.38(T - 273.15) + 732.5, \\ \lambda &= \lambda_{eff}(\chi) = A_2 + \frac{A_1 - A_2}{1 + e^{(\chi - x_0)/dx}}, \\ k_l &= k_l(\chi) = k_{sat}\chi^3, \end{aligned} \tag{59}$$

where A_1 and A_2 [W/(Km)] are the thermal conductivities for dry and fully saturated medium, respectively, x_0 [-] is the saturation for which the thermal conductivity is the average value between the extreme values, dx [-] is a parameter, and k_{sat} [m^2] is the permeability of the fully saturated medium.

For diffusivity of vapour-air mixture we use the relation (Vargaftik, 1975)

$$D = D_{\mathrm{ref}} \left(T / T_{\mathrm{ref}} \right)^n . \tag{60}$$

Summary of the parameter values is given in Table 1.

Heater power

Power production of both the heaters are estimated from the calculated 1D temperature and humidity profiles. The power of a heater [W] is

$$P_{\mathrm{h}} = P_{\mathrm{in\,t}} + P_{\mathrm{out}} , \tag{61}$$

where

$$P_{\mathrm{in\,t}} = \frac{d}{dt}\left(\rho_{\mathrm{h}} e_{\mathrm{h}} V_{\mathrm{h}} \right) + \sum_{\mathrm{k}\in\{\mathrm{s,l}\}} \frac{d}{dt} \int_{V_{\mathrm{buffer}}} \rho_{\mathrm{k}} e_{\mathrm{k}} dV = \left(\rho V c \right)_{\mathrm{h}} \frac{dT_{\mathrm{h}}}{dt} + 2\pi L \sum_{\mathrm{k}\in\{\mathrm{s,l}\}} \frac{d}{dt} \int_{R_1}^{R_2} \xi_{\mathrm{k}} \tilde{\rho}_{\mathrm{k}} c_{\mathrm{k}} T r dr \tag{62}$$

is the rate of change of the internal energy of the system consisting of the heater and the buffer, and

$$P_{\mathrm{out}} = \int_S \mathbf{n} \cdot \mathbf{q} dS = 2\pi R_2 L H \left(T\left(R_2 \right) - T_{\mathrm{r}} \right) \tag{63}$$

is the total heat flux escaping the buffer at the rock boundary. L = 5.05 m is the half length of the liner. The heater properties are approximated by assuming the whole interior of the buffer to consist of iron (c_{h} = 4500 J/(kg K) , ρ_{h} = 7900 kg/m^3) with an infinite heat conductivity and the volume V_{h} = 1.3 m^3 per heater, estimated with the aid of the given information on the material inside the buffer (liner, casings, heating elements). Vaporization is neglected because the subsequent condensation occurs inside the buffer. Also, internal energy change of the gaseous components is neglected. Because the approach is in 1D the heat flux escaping the ends of the heaters in the direction of the x-axis is not considered and the result is an estimate of the lower bound of the heating power.

Results

The simulated and measured results for the evolution of relative humidity and temperature at the points E1H, E1C, and E1G are illustrated in Figures 4 and 5, respectively. Figure 6 shows the radial distributions of relative humidity and temperature for section E1 in both the directions RD3 and RD4. Figure 7 shows the radial distributions of relative humidity and temperature for section E2 in both the directions RD3 and RD4. Figure 8 shows the radial distributions of relative humidity and temperature for both the sections E1 and E2 in the direction RD2. Figure 9 shows the radial distributions of relative humidity and temperature for both the sections E1 and E2 in the direction RD1. The heater power calculated by the results for the temperature and saturation profiles in the section E1 and direction RD4 is illustrated in Figure 10.

Discussion

The presented thermohydraulic simulations are essentially simplified 1D predictions of the relative humidity by means of calibration of the temperature boundary conditions. The actual asymmetrical geometry, behaviour of the heater, liner or rock, and the mechanical behaviour of the buffer are not considered. Other simplifications in the modelling are the neglecting of the convection heat transfer, the pressure variation due to the vaporisation by assuming an infinite gas mobility, the dependence of dynamic viscosity of liquid on temperature, the dependence of liquid density on temperature and pressure, and the effect of the structure of the bentonite to the gas diffusion. An included feature that could have been omitted is the effect of vaporisation on the temperature field, which was found essentially negligible.

The main simplifications associated with the simulation are the simulation of the heater adjustment period between 0…53 d by a linear increase of temperature against time, and the use of a full saturation boundary condition at the rock boundary.

When the performance of the heaters is simulated by means of temperature boundary conditions, the lack of temperature data constitutes a source of uncertainty. Other main uncertainties associated with the simulation are related to the actual initial moisture distribution in the buffer and to the effect of the construction gaps and the instrumentation. The initial moisture content at any particular point of the buffer is not known. The buffer consisting of 5331 bentonite blocks of individual properties with gaps between them in the beginning is neither homogenous nor isotropic. The average initial gravimetric water content has a variation of 13.07…14.87 % between the different block types used. According to the present model this corresponds to the range of 29…42 % for the initial relative humidity. Additionally, the moisture content of every block has changed because of the ventilation during the construction phase. Liquid and vapour may actually move more freely near the measuring points than in the simulation causing more rapid wetting and drying than expected. In the beginning the liquid water and, especially, the vapour move preferably along the gaps between the bentonite blocks. The measuring instruments break the homogeneity of the buffer especially near the measuring points. The channels of the cables constitute preferable routes for fluid flow with a larger permeability than in an intact buffer.

Fitting of the model against the suction experiment is done only by means of the wetting curve. There are no measurements in the region below $\chi = 0.50$. The suction parameter fit could be made better by introducing a more complicated adsorption function.

The largest discrepancy between the measured and simulated results can be seen in the case of relative humidity evolution at the centre of the buffer, i.e., at the point E1C in Figure 4, after the starting of the heaters at day 0. First a rapid condensation is measured followed by a rapid vaporisation after a sufficient temperature increase. In the simulation the same effect of consecutive wetting and drying is seen in considerably less extent at the region nearer the heater, e.g., at the point $r = 0.70$ m depicted in Figure 4. We suggest that this discrepancy is due to the gaps and instrumentation present in the actual case.

Despite the simplifications and uncertainties the simulation results and the measurements are fairly consistent. The model succeeds in describing the essential features of the thermohydraulic behaviour, i.e., heat transfer, vaporisation, flow of liquid water, gas diffusion, and suction induced by adsorption.

References

CSC - The Finnish IT Center for Science, 21st January 2003, *ELMER*, [WWW document] http://www.csc.fi/Elmer/.

Frémond, M., and Nicolas, P., *Macroscopic thermodynamics of porous media*, Continuum Mechanics and Thermodynamics 1990, 2:119-139.

Hartikainen, J., and Mikkola, M., *Thermomechanical model of freezing soil by use of the theory of mixtures*, In Proceedings of the 6th Finnish Mechanics Days, Aalto, J., and Salmi, T., (eds), 1997, 1–26.

Nicolas, P., *Liquid-vapour phase change in porous media*, Mathematical Models for Phase Change Problems, International Series of Numerical Mathematics, Vol. 88, Birkhäuser Verlag Basel, 1989.

Nicolas, P., *Modélisation mathématique et numérique des transferts d'humidité en milieu poreux*, PhD Thesis, Paris University VI, 1992.

Schmidt, E., *Properties of Water and Steam in SI-Units*, Springer, Berlin, 1989.

Vargaftik, N. B., *Tables on the thermophysical properties of liquids and gases - in normal and dissociated states: English transl. - 2. ed*, Wiley, New York, 1975.

Ziegler, H., *An Introduction to Thermomechanics*, North-Holland Publishing Company, 1977.

Ziegler, H., Wehrli, C., *The derivation of constitutive relations from the free energy and dissipation function*, In *Advances in Applied Mechanics*, volume 25, pages 183-238, New York, 1988.

Tables and Figures

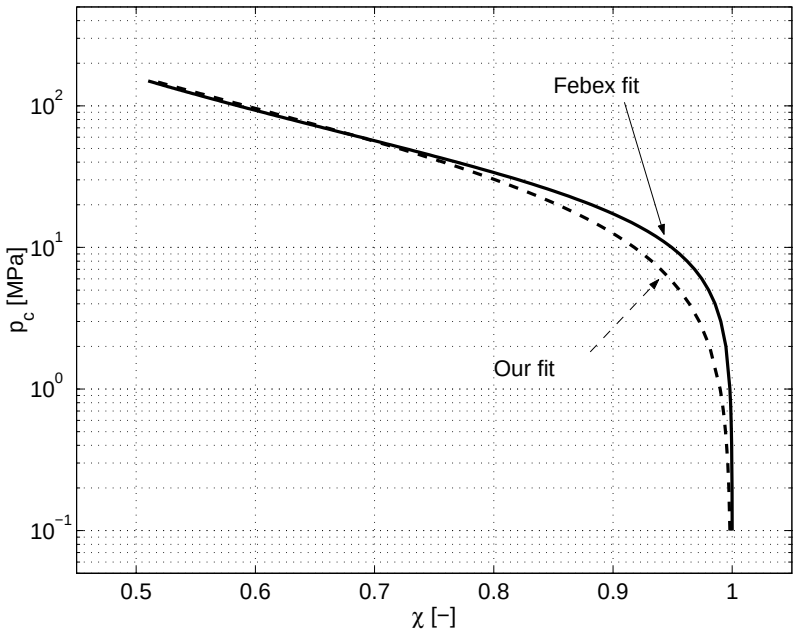

Figure 1: The suction curve (50) (dashed) and the one used in the Febex experiments (solid). The wetting experiment of a confined sample with ρ_{dry} *= 1600…1650 kg/m*^{3}.

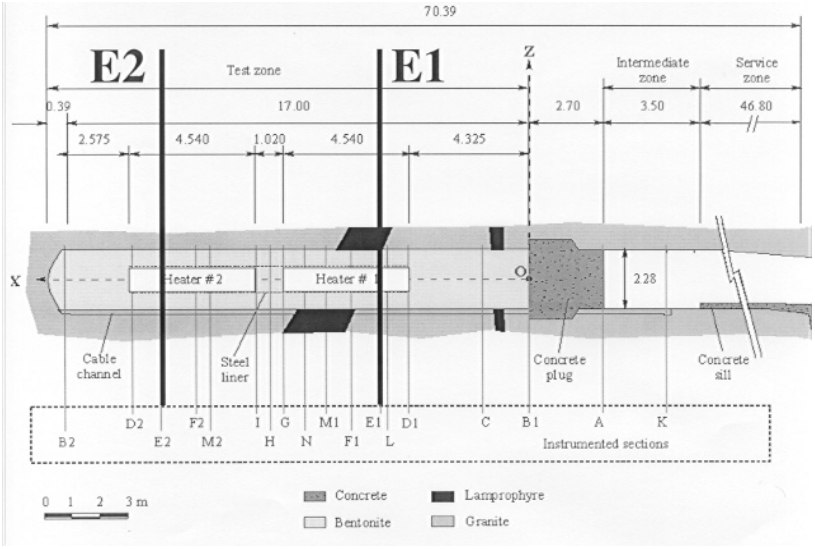

Figure 2: The profile of the Febex in situ experiment and the definitions of the simulated sections E1 and E2.

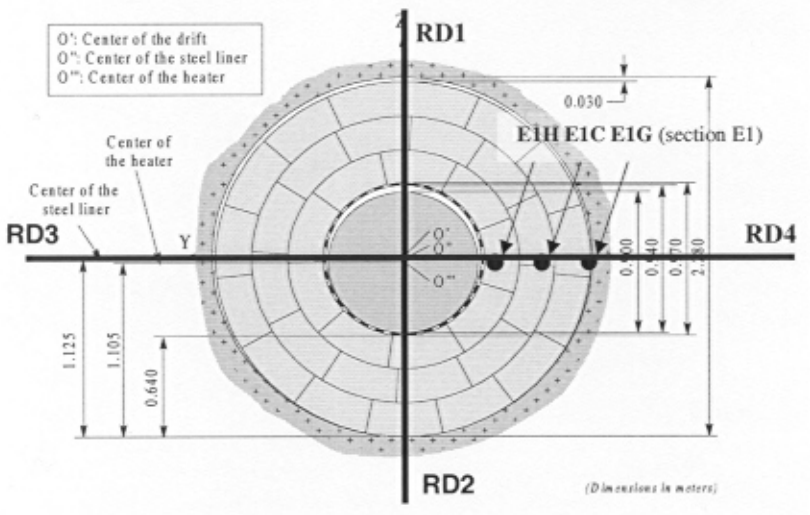

Figure 3: A typical Febex cross section. Definition of the directions RD1, RD2, RD3, and RD4. The points E1H, E1C, and E1G of the section E1 correspond to r = 0.52, 0.81, and 1.10 m, respectively, in the 1D simulation.

Table 1: Summary of the used parameter values.

Initial and reference		**Literature**			**Calibration**		
Name	Value	Name	Value	Source	Name	Value	Case
T_0	293.15 K	R	8.314 J/(mol K)		a	0.4	suction experiment
P_0	0.1013 MPa	M_v	0.018 kg/mol		H	1.9 W/(m^{2}K)	
χ_{init}	0.54	μ_l	$1.0 \cdot 10^{-3}$ kg/(s m)	(Schmidt, 1989)	$T(R_1)$	93 °C	E1; RD3, RD4
η_0	0.45	ζ_0	0.023	(Schmidt, 1989)	$T(R_1)$	96 °C	E2; RD3, RD4
χ_{max}	0.999	D_{ref}	$0.216 \cdot 10^{-4}$ m^2/s	(Vargaftik, 1975)	$T(R_1)$	99 °C	E1, E2; RD2
ρ_{dry}	1690 kg/m^3	T_{ref}	273 K	(Vargaftik, 1975)	$T(R_1)$	80 °C	E1, E2; RD1
T_r	12 °C	n	1.8	(Vargaftik, 1975)			
Laboratory test		$\bar{\rho}_l$	998 kg/m^3	(Schmidt, 1989)			
Name	Value	c_v^p	$1.87 \cdot 10^3$ J/(kg K)	(Schmidt, 1989)			
A_1	0.57 W/(K m)	c_l^p	$4.18 \cdot 10^3$ J/(kg K)	(Schmidt, 1989)			
A_2	1.28 W/(K m)	$L(T_0)$	$2.45 \cdot 10^6$ J/kg	(Schmidt, 1989)			
x_0	0.65	c_h	$4.50 \cdot 10^3$ J/(kg K)				
dx	0.10	ρ_h	7900 kg/m^3				
k_{sat}	$2.0 \cdot 10^{-21}$ m^2	V_h	1.3 m^3				

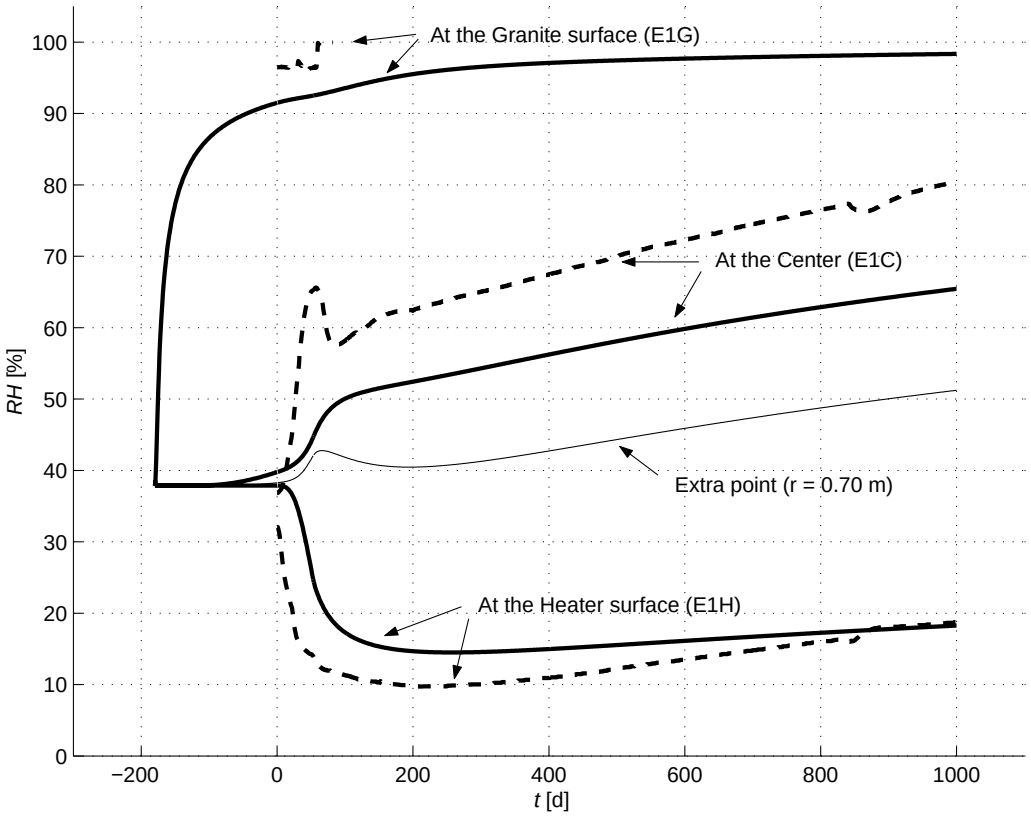

Figure 4: Evolution of relative humidity at the points E1H, E1C, and E1G. Dashed curves show the measured values and solid curves the simulation result. The thin solid curve shows the simulated extra point r = 0.70 m.

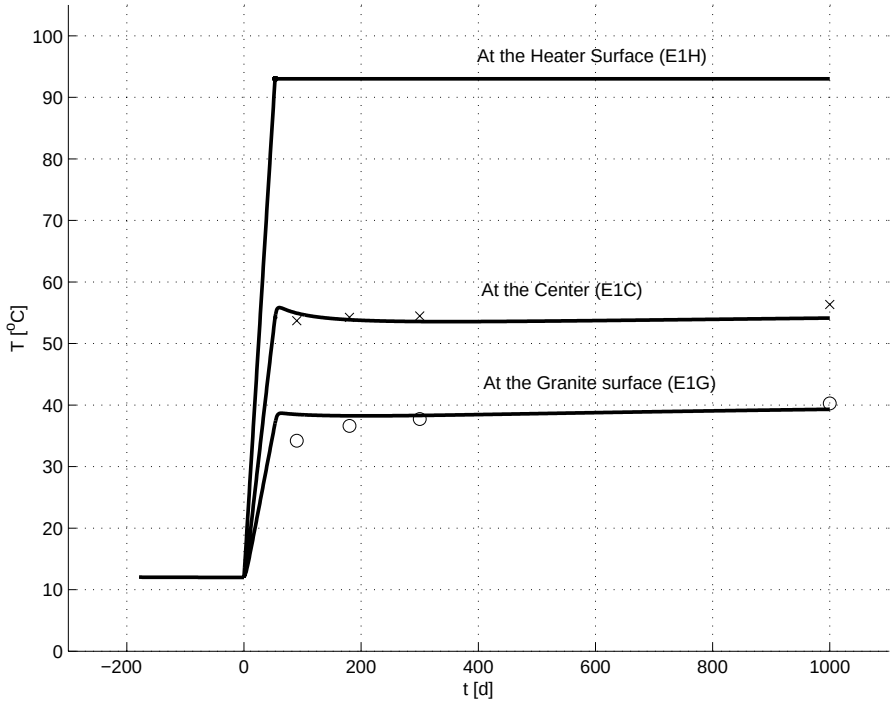

Figure 5: Simulated (curves) and measured (symbols) evolution of temperature at the points E1H, E1C, and E1G.

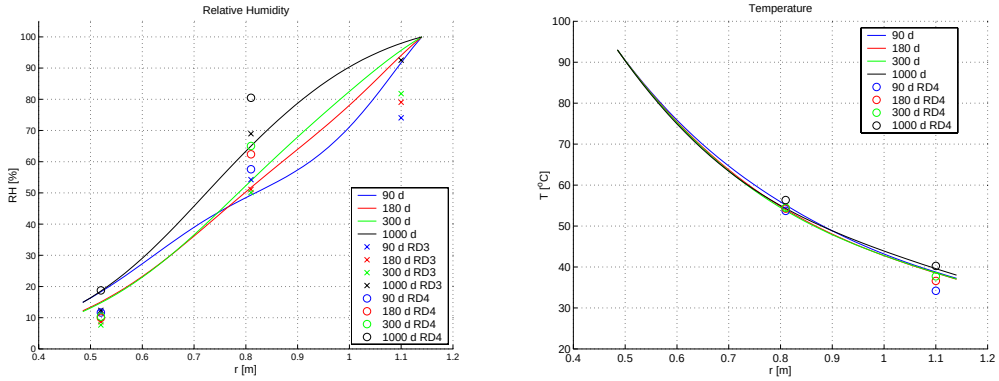

Figure 6: Simulated (curves) and measured (symbols) radial distributions of relative humidity (left) and temperature (right) at 90, 180, 300, and 1000 d for the section E1 in the directions RD3 and RD4.

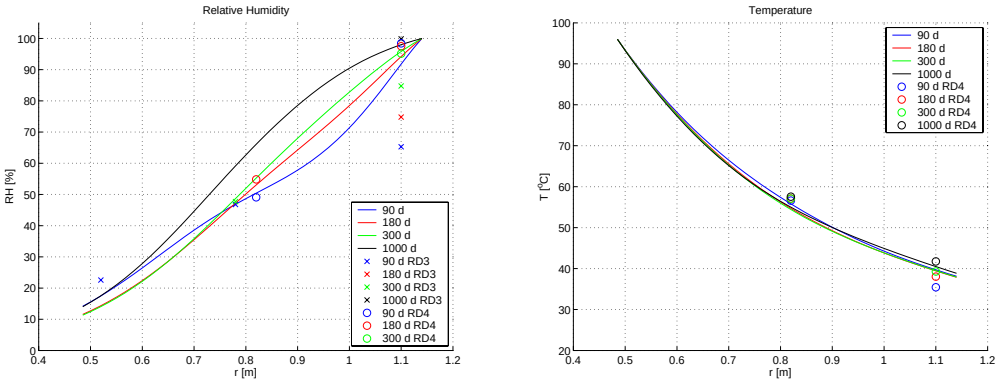

Figure 7: Simulated (curves) and measured (symbols) radial distributions of relative humidity (left) and temperature (right) at 90, 180, 300, and 1000 d for the section E2 in the directions RD3 and RD4.

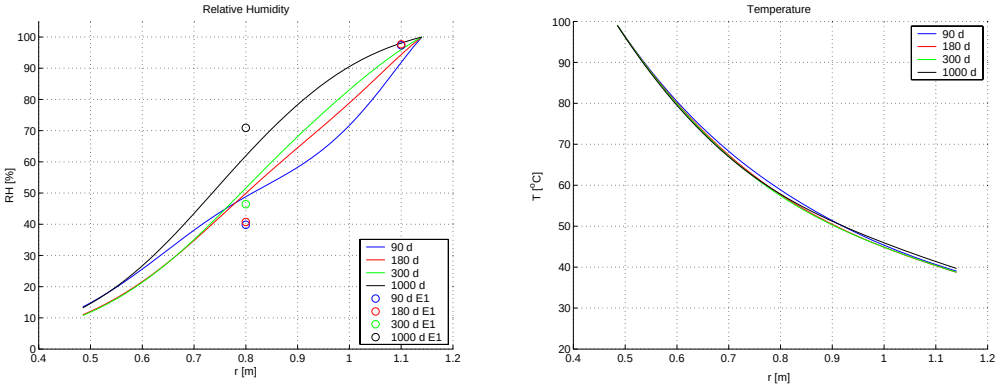

Figure 8: Simulated (curves) and measured (symbols) radial distributions of relative humidity (left) and temperature (right) at 90, 180, 300, and 1000 d for the sections E1 and E2 in the direction RD2.

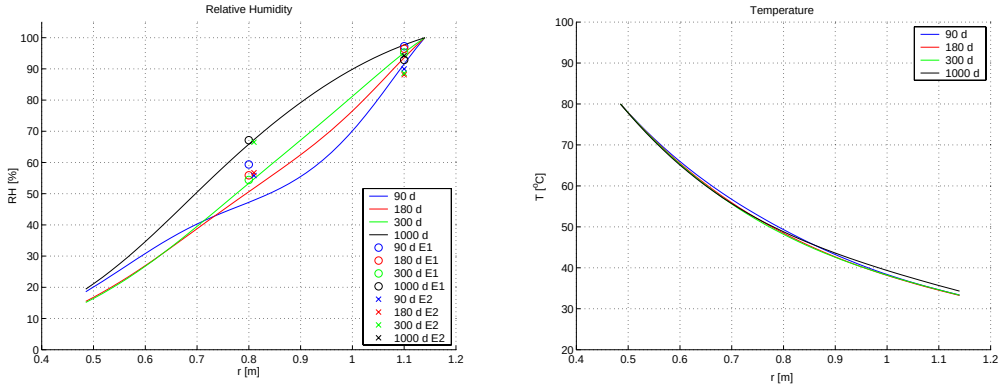

Figure 9: Simulated (curves) and measured (symbols) radial distributions of relative humidity (left) and temperature (right) at 90, 180, 300, and 1000 d for the sections E1 and E2 in the direction RD1.

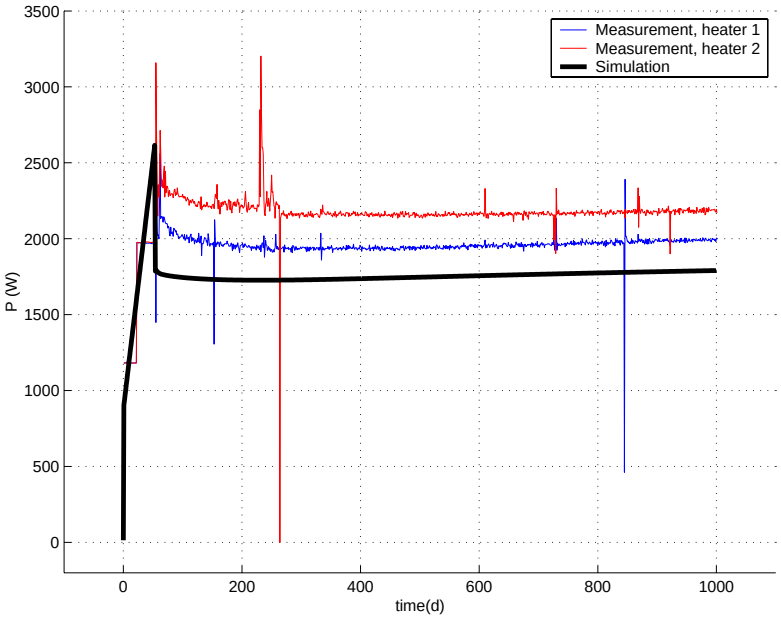

Figure 10: Simulated and measured power of the heaters.

DECOVALEX III

The THM Upscaling Bench Mark Test

Progress Report

28 May 2003

Johan Öhman and Auli Niemi
Uppsala University, Sweden

Juha Antikainen,
Helsinki University of Technology, Finland

Research Sponsored by Finnish Radiation and Nuclear Safety Authority

Preface

This progress report describes the work done as STUK (Finnish Radiation and Nuclear Safety Authority) contribution to DECOVALEX III, Bench Mark Test 2. The general approach and hydrological simulations are by Johan Öhman and Auli Niemi (Uppsala University, Sweden) and the thermo-mechanical simulations by Juha Antikainen (Helsinki University of Technology, Finland). We wish to thank STUK, especially Dr. Esko Eloranta for his support and DECOVALEX secretariat especially Dr. Johan Andersson (Streamflow AB) and Dr. Leslie Knight (Nirex) for the help with the data.

Table of Contents

1. Introduction and general approach

Understanding the hydrological conditions in the surrounding bedrock is a central element for the safe disposal of high-level nuclear waste. It is well known that only a part of the geologically observable fractures – or of their surface areas - are water conducting. Due to this strong heterogeneity, predicting the conductivity distribution of fractures and fracture networks is a highly demanding task even when predicting the present situation. In related site characterization, fracture conductivities, flow rates, travel times and other relevant hydraulic parameters are therefore often expressed through probability distributions rather than as fixed, deterministic values.

Furthermore, in the final disposal situation the thermo-hydro-mechanical conditions in the bedrock change due to tunnel excavation and heat generation from the waste. These thermo-hydro-mechanical processes and their quantitative modelling are investigated in the DECOVALEX III project. This progress report addresses the modelling of one of the problem scenarios in DECOVALEX III, namely the upscaling of THM-processes or Bench Mark Test 2 (Decovalex III, 2000).

We summarize our objectives as to:

(i) evaluate the significance of the THM-processes to the performance assessment, taking into account the heterogeneity of the rock
(ii) develop a procedure to upscale the essential THM processes and variables to be used in larger scale models
(iii) evaluate the uncertainties related to the evaluation of THM-processes and their upscaling in comparison to the uncertainty due to hydrological heterogeneity alone.

In this progress report we (i) first describe the general approach used and (ii) show the results obtained.

1.1 General approach

The general approach can be described as follows:

(i) First the flow and transport properties of the rock are analysed at the small scale by means of a hydraulic fracture network model. For this we use the FracMan fracture generation program (Derschowitz *et. al*., 1998) along with MAFIC flow and transport software (Miller *et. al*., 1998). The models allow treatment of complex fracture geometries and hydraulic conductivity distributions. Our approach is probabilistic, i.e. large number of network realizations will be generated and the conductivity characteristics of the small scale blocks are studied by determining the directional hydraulic conductivity versus angle plots that allow examination of the validity of continuum approximation.

(ii) Based on the results of the previous step, either a continuum or non-continuum approach is selected for the large-scale flow and transport model. In this case continuum approximation turns out to be valid and results from the small scale simulations in the previous step are used as input for the large-scale model. GSLIB (Deutsch and Journel, 1998), which is a geostatistical software package, is used for generating correlated non-parametric conductivity fields and the TOUGH2 (Pruess et al., 1999) code is used for flow calculations.

(iii) Next, the effect of mechanical and thermo-mechanical changes due to repository excavation and filling as well as the thermal load from the waste are simulated with the UDEC model (Itasca, 2000). Here somewhat more simplified fracture geometries are used, as this is a two dimensional model and do not allow as complex geometries as the above flow models. The result will give changes in fracture apertures at various locations and for various fracture orientations, which results will be transferred into to flow model. Next the steps (i) and (ii) will be repeated to see the significance of the THM effect e.g. in relation to the hydrology induced uncertainty.

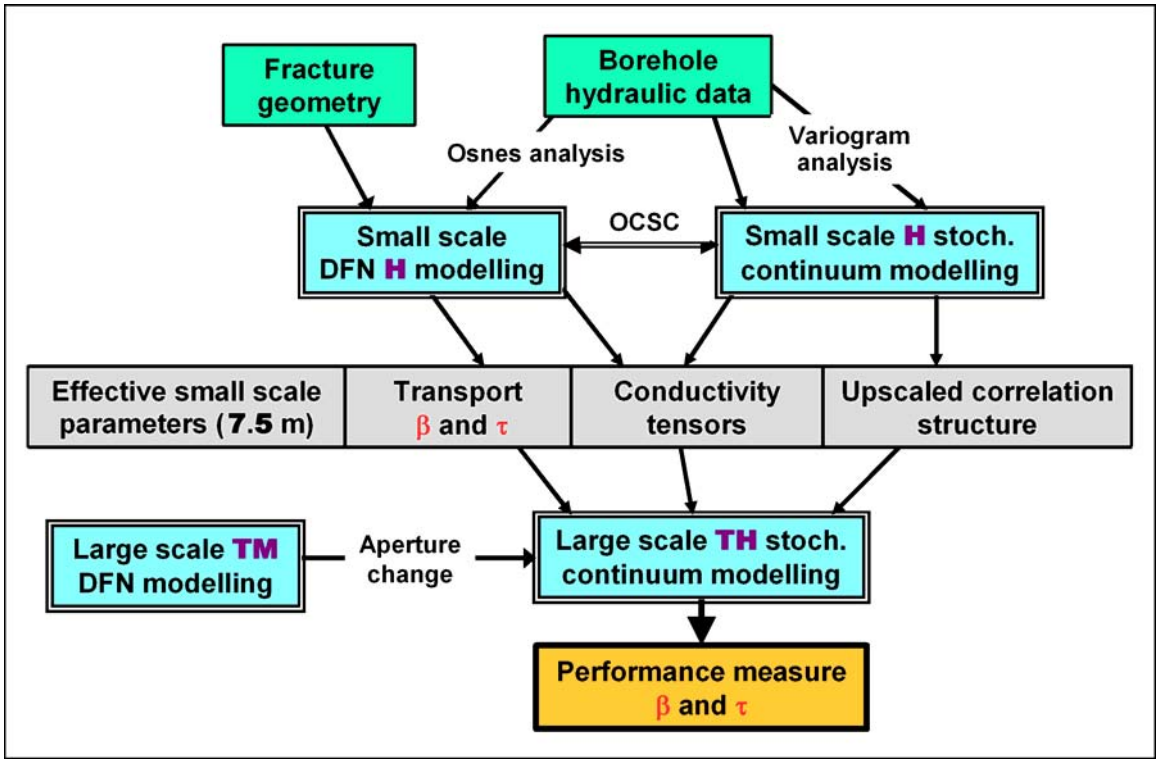

Figure. 1-1. *A general overview of the approach taken.*

1.2 Outline of report

In the following chapters we will first describe the hydraulic upscaling simulations and the implications of the results in terms of large scale modelling (section 2). In the following section (3) variograms from borehole data are used to upscale correlation structures for the obtained effective conductivities. Sections 4 and 5 outline the approach taken for transport modelling. Next, the thermo-mechanical simulations are summarized in section 6. Finally, we show the impact of TM effects on transport properties at the large scale (section 7).

2. Hydrological upscaling by means of fracture network modelling

2.1 Analysis of transmissivity data

We follow the general approach taken by Nirex, based on their extensive investigations at the Sellafield site, that for the rock in question (Burrowdale Volcanic Group (BVG)) the effective permeability is governed by a large number of low transmissive fractures and that matrix flow is negligible and can be ignored (Nirex 1997d).

Fracture transmissivity distribution and the frequency of conductive fractures are determined from hydraulic packer test data by using an approach by Osnes et al. (1988). The method has been numerically implemented in the fracture generation code (Dershowitz et al., 1998) as a separate analysis module. The method assumes that the net transmissivity of a tested interval, T_i, is equal to the sum of the transmissivities of all conductive fractures, T_{ij}, that intersect the packer interval *i*

$$T_i = \sum_{j=1}^{n_i} T_{ij} \,, \tag{2.1}$$

where T_i is the measured transmissivity for the interval *i*, n_i is the number of conductive fractures that intersect *i*, T_{ij} is the transmissivity of the j^{th} conductive fracture within *i*. In the Osnes method, n_i is stochastically generated from a Poisson distribution with an expected value of ***n***, which is a parameter found by iteration. The interval transmissivities in the packer test are assumed to be influenced by a number of interconnected fractures. The individual fracture transmissivity, T_{ij}, as seen by the packer test is actually a network transmissivity that is related to the fracture transmissivities, T_{fi}, for a number of *m* interconnected fractures.

$$T_{ij} = \frac{m}{\sum_{i=1}^{m} \frac{1}{T_{fi}}} \,. \tag{2.2}$$

The number of interconnected fractures, *m*, in such a network transmissivity is set to 3. The transmissivity data from 100 short interval pulse tests (Figure. 2-1) was analysed in the Osnes module. Each interval was 1.56 m long. The minimum interval transmissivity was set to 10^{-15} m^2/s. Any value smaller than this is considered a *no flow* interval.

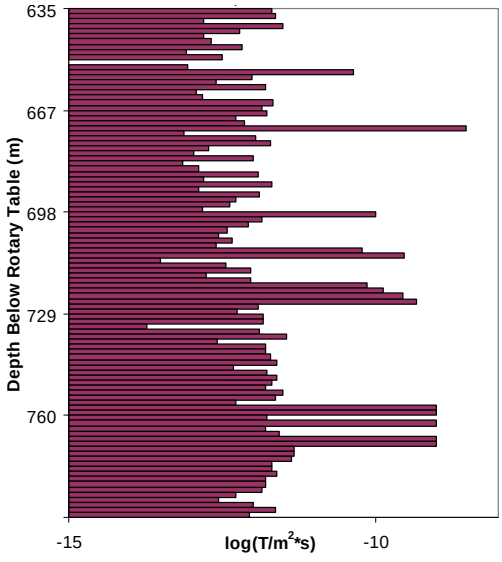

Figure. 2-1. *Transmissivity data from packer test consisting of 100 contiguous 1.56 m interval pulse tests carried out in the lower formation.*

The Osnes method finds the most likely values for the following three unknown parameters; the frequency of conductive fractures, $\boldsymbol{P_{10}^{cond}}$, and a lognormal distribution describing fracture transmissivity, by $\boldsymbol{\mu_{logT}}$ and $\boldsymbol{\sigma_{logT}}$. These values are found by

iteratively searching for the best fit between the packer test data and a distribution of Monte Carlo simulated T_i values. The fit is evaluated by Chi-Squared, χ^2, (the weighted average difference between PDFs) and Kolmogorov-Smirnov, *K-S*, (the single largest absolute difference between the CDFs) tests.

In the iterative process of finding the values for the three parameters $\boldsymbol{P_{10}^{cond}}$, $\boldsymbol{\mu_{logT}}$ and $\boldsymbol{\sigma_{logT}}$, that produce the least χ^2 sums and smallest K-S values, the value of $\boldsymbol{P_{10}^{cond}}$ was allowed to vary from 0 to 5.53, which is the *total* 1D vertical fracture frequency and found from projecting the mean perpendicular spacings of all four fracture sets to a vertical scanline (see Table 2-1.) The vertical fracture frequency is only used as the upper limit, since all fractures are not likely to be conductive. When starting the iterative fitting process using the initial value for $\boldsymbol{P_{10}^{cond}} = 0$, it rapidly converges to a value larger than 2. On the other hand when starting with the initial value for $\boldsymbol{P_{10}^{cond}} = P_{10,vertical} = 5.53$, it decreases to a value below 4.7. The measured data and modelled fits from an Osnes iteration for $\boldsymbol{P_{10}^{cond}} = 2.49$ is shown in Figure 2-2. The optimization of the Osnes analysis, described more in detail in Öhman and Niemi (2003), yields the parameter combination $\boldsymbol{P_{10}^{cond}} = 2.25$, $\boldsymbol{\mu_{logTf}} = -12.7$ and $\boldsymbol{\sigma_{logTf}} = 1.2$.

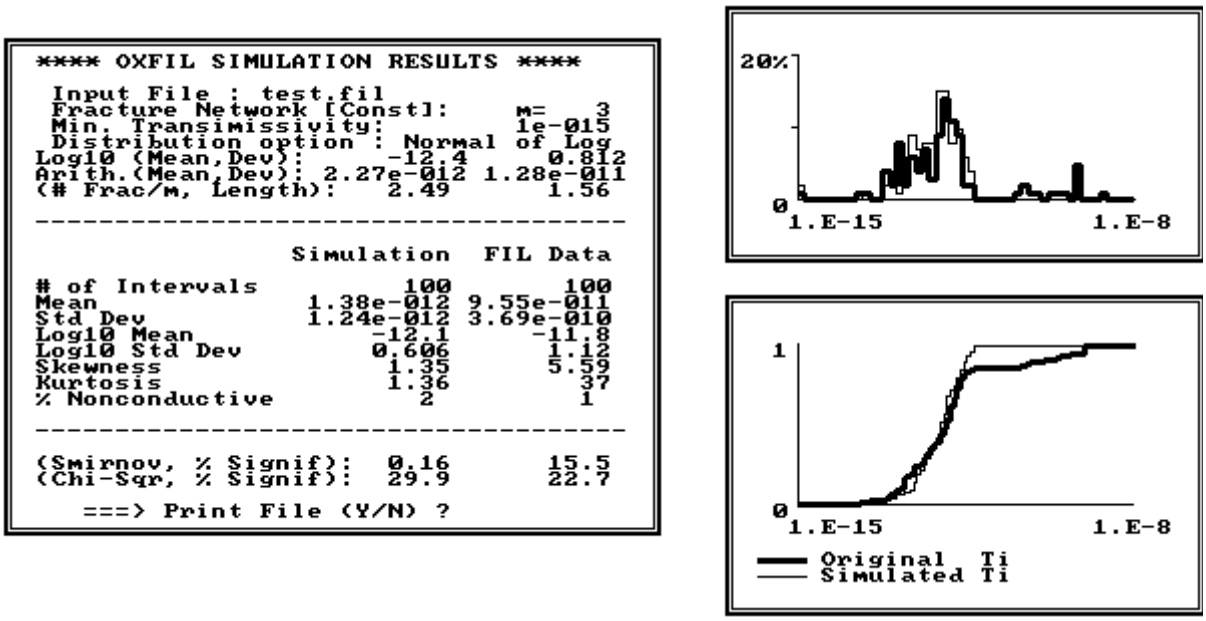

Figure. 2-2. *Result from one Monte Carlo simulation, $P_{10}^{cond} = 2.49$ fractures/m.*

2.2 Generating fracture network realisations

The BART Beacher model in the FracMan software was used to generate 150 realisations from the available discontinuity data for the lower Formation. The BART Beacher model requires the following information:

1. fracture orientation (defined by trend, plunge and the Fisher κ value)
2. 3D fracture intensity of conductive fractures (P_{32}^{cond})
3. fracture size distribution (here defined by a 3D power law distribution of fracture radii, under the assumption of circular fractures)
4. termination percentage ($\%_{term}$)
5. fracture transmissivity distribution (defined by N(μ_{logT}, σ_{logT}), previous section)

2.2.1 Fracture geometry data

The fracture geometry data is reported by Nirex (1997 c) and compiled by Andersson and Knight (2000) is shown in Table 2.1.

Table 2.1. *Fracture geometry Data*

Fracture Set	[1)]Mean dip (º)	[1)]Dip direction (º)	[1)]Fisher, κ	[1)]Perpendicular spacing, S_f (m)	[2)]Total 3D intensity, P_{32} (m^2/m^3)	[3)]Conductive 3D intensity, P_{32}^{cond} (m^2/m^3)
1	08	145	5.9	0.29	2.91	1.09
2	88	148	9	0.26	3.24	1.22
3	76	021	10	0.28	3.01	1.13
4	69	087	10	0.31	2.74	1.02

[1)]Nirex (1997c)
[2)] Calibrated with the FracMan software, based on data on perpendicular fracture spacing, S_f.
[3)] Determined based on P_{32} and hydraulic data.

2.2.2 Intensity of conductive fractures, P_{32}

In the problem definition 2D fracture intensity, P_{21}, [m/m^2] is given, as 4.8 m/m^2 with an upper limit of 10 and a lower limit of 2 m/m^2 for a cut-off length, $L_{cut\text{-}off}$, of 0.5 m. The BART Beacher model requires a fracture intensity value for conductive fractures, P_{32}^{cond}, which is defined as the fracture area per rock volume [m^2/m^3]. First, the total fracture intensity, P_{32}, for each fracture set was calibrated by trial and error, i.e. to generate a number of large realisations and use FracMan sampling features to examine the network properties and match those with discontinuity values given in the problem definition. The calibration strategy aimed to match three parameters: a) the mean perpendicular spacing for each set, b) the total 2D horizontal fracture intensity, P_{21},= *4.8* [m/m^2], and c) the total 1D vertical fracture frequency, $P_{10,vertical}$ = 5.53 (see Figures. 2-3a-c.).

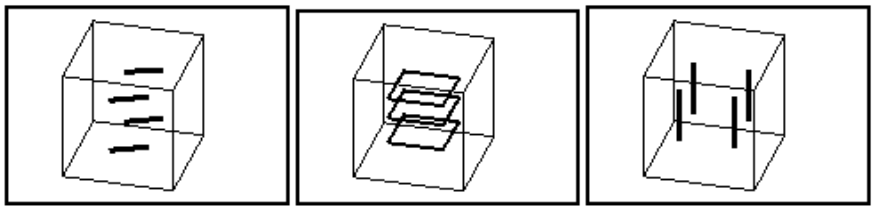

Figures. 2-3a-c*. FracMan sampling features used to calibrate the P_{32} values; boreholes perpendicular to a single fracture set, horizontal traceplanes and vertical boreholes for entire realisations.*

The mean perpendicular spacing (a) was evaluated *for each* fracture set by examining the number of fractures, that is intersected by 4 boreholes (*perpendicular* to the fracture set orientation) having a total length of 20 m. Having calibrated P_{32} values to match the perpendicular spacing for all four sets individually, the next step was to examine entire realisations with respect to available data. The P_{21} (b) for were monitored (using 3 horizontal 25 m^2 tracemaps) and $P_{10,vertical}$ (c) was evaluated (by the total number of fracture intersections by 4 *vertical* boreholes having a total length of 20 m). The P_{32} values were determined for each set so that the parameters a), b) and c) were well fitted on average for 10 realisations, even though each single realisation shows stochastic variation (see Table. 2-1.). It is important to keep in mind that the obtained P_{32} values correspond to geologically observed fractures, not the hydraulic active subset of the fracture network that we intend to generate in the model.

Next, the intensity of conductive fractures, P_{32}^{cond}, were calculated as a subset of the total fracture intensity, P_{32}, using the ratio between P_{10} and P_{10}^{cond}, found in section 2.1. This is done using a linear relationship between P_{10}, P_{21} and P_{32} suggested by Dershowitz and Herda (1992),

$$\frac{P_{10}^{cond}}{P_{10}} = \frac{2.25}{5.53} = \frac{P_{21}^{cond}}{P_{21}} = \frac{P_{32}^{cond}}{P_{32}}. \tag{2.3}$$

2.2.3 Fracture size distribution

The fracture radii distribution of the 3D fracture network origins from a cumulative power-law fracture trace length distribution for a 2D surface, compiled by Andersson and Knight (2000),

$$N(L) = 4\,L^{-2.2}, \tag{2.4}$$

where $N(L)$ is the number of fractures per m^2 having a fracture length larger than L. The length distribution in (3) is determined from analysis of one-dimensional scan-lines, two-dimensional trace maps from outcrops and aerial photography lineaments and reported by Nirex (1997x), and is valid for fracture lengths between 0.5 and 250 m.

In section 2.2.2 it was found that 60 % of the fractures were regarded as non-conducted and hence excluded from the fracture network generation. Studying tracemaps of the realisations implies that the removed (non-conductive) fractures probably are predominantly short fractures, since short fractures are likely to have lower connectivity and smaller apertures. Under this assumption, we increase the cut-off trace length from 0.5 m to 0.83 m which corresponds to a 45 % fracture intensity reduction, according to

$$\frac{P_{32}^{cond}}{P_{32}} = \frac{P_{21}^{cond}}{P_{21}} = \frac{\int_{L_C}^{250} L\,\frac{d\left(N^{cond}(L)\right)}{dL}}{\int_{0.5}^{250} L\,\frac{d\left(N(L)\right)}{dL}}. \tag{2.5}$$

The remaining 15 % fracture intensity reduction is taken from the entire trace length population.

Cut-off trace lengths for a 2D surface are then related to fracture cut-off radii using a method by Pigott (1997), which gives a cut-off radius of 0.65 m. According to Barton (1995) a 3D fractal dimension can be extrapolated from a 2D fractal dimension, simply by adding 1.0. Although the 2D fractal dimension is given as the exponent -2.2 [$^{+}/_{-}$ 0.2] (see 3.), the value –3.0 was used (rather than –3.2) as the 3D power law exponent, since it is the minimum value allowed in the FracMan code.

2.2.4 Fracture intersection termination

The percentage of fractures that terminate in an intersection with another fracture, $\%_{term}$, was evaluated by dividing the total observed number of terminations in *other fractures* by the total number of *all* observed fracture terminations,

$$\%_{Term} = \frac{2\sum TT + \sum TU + \sum TR}{2\sum TT + \sum TU + 2\sum TR + 2\sum RR + \sum RU} = 73.1\% . \qquad (2.6)$$

Given this input, the BART Beacher model will generate 26.9 % of the fractures from uniformly located fracture centers, while the remaining 73.1% fractures are generated from locations uniformly distributed *on the surfaces of existing fractures*, to ensure that the clustering properties are represented in the realisation.

2.4 Modelling effective conductivity at small scale

The aim is to investigate conductivity anisotropy in different directions of flow. If conductivity of the fractured rock can be described by an ellipsoid, the conductivity of such a network can then be simplified by a symmetric tensor and modelled by means of continuum approximation [Long et al. (1982); Cacas et al. (1992); Niemi et al. (2000)].

2.4.1 Conceptual model and simulations

A cubic fracture network of 7.5 × 7.5 × 7.5 m^3 was cut out from the center of a 20 × 20 × 20 m^3 realisation, using the FracMan module MeshMaster (Dershowitz, *et. al*., 1998), shown in Figures 2-4a and b. The fracture networks are cut out every 15 ^{o} direction, θ, from 0 ^{o} to 165 ^{o}, in a vertical cross section parallel to the large scale modelling plane. The conductivities for orientations 180 ^{o} to 345 ^{o} are symmetrical (but opposite direction) to the previous directions and hence not examined. The scale of the investigated network is chosen because this realisation volume contains the maximum number of fractures that can be handled by the FracMan code.

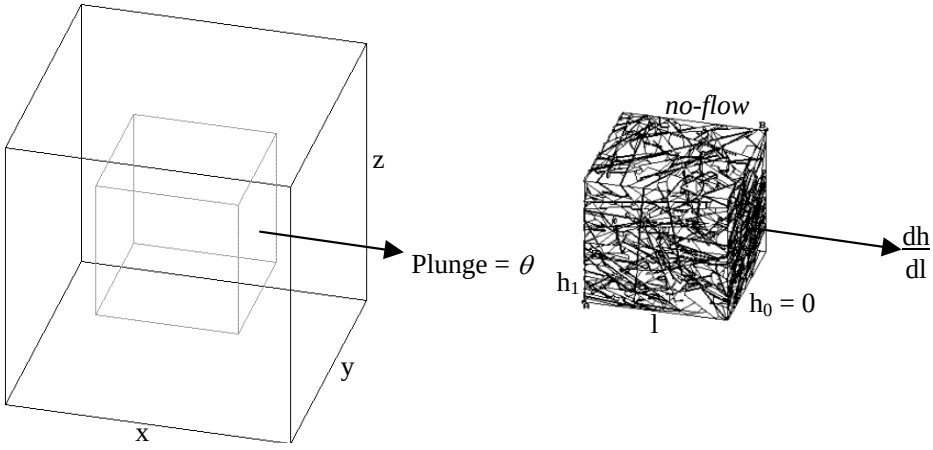

Figures. 2-4a and b. *Fracture networks are cut out at different directions from a realization. A hydraulic gradient is applied in the direction of cutting, θ.*

For each fracture network a specified head pressure, h_1, was applied on one side and h_0 = 0 m to the opposite side, thus obtaining a hydraulic gradient, *dh/dl*, in the direction of cutting, θ. The remaining 4 sides were assigned no-flow boundary conditions. A discrete fracture mesh was edited using the FracMan module EdMesh (Lee, *et. al*., 1999). The flow field for each directional angle from 0 ^{o} to 165 ^{o} was then simulated using the FracMan module MAFIC (Miller, *et. al*., 1998) and the corresponding directional conductivities, $K(\theta)_{sim}$, were calculated from Darcy's Law:

$$Q(\theta) = -K(\theta)_{sim} \cdot A \cdot \frac{dh}{dl}. \quad (2.7)$$

A certain amount of fractures had to be cut out in order for MAFIC to handle the large amount of data. Cutting out all fractures with a T_f less than 5 *10^{-14} m^2/s reduced the amount of data to such an extent that solution could be obtained for all rotated networks.

2.4.2 Results from small scale hydraulic modelling

For each of the 150 realizations, the directional conductivities, $K(\theta)_{sim}$, obtained from (2.7), were fitted to a two-dimensional symmetric conductivity tensor for continuum media, Harrison and Hudson (2000), which can be described by the three unknown parameters K_1, K_2 and ξ,

$$K(\theta)_{tensor} = K_1 \cos^2(\theta+\xi) + K_2 \sin^2(\theta+\xi), \quad (2.8)$$

Where θ is a counterclockwise angle from the horizontal and ξ is the clockwise angle from the horizontal to the direction of major principal conductivity, K_1. The fit was done by finding the smallest root of mean of squares between the simulation result, $K(\theta)_{sim}$, and the ideal continuum tensor, $K(\theta)_{tensor}$, in an iterative manner. To facilitate comparisons between realizations, the dependency on magnitude was removed by normalizing each fit with respect to the major and minor principal conductivities (K_1 and K_2), according to

$$RMS_{Norm} = \frac{\sqrt{\frac{1}{n}\sum_{n=1}^{12}\left(K(\theta)_{tensor} - K(\theta)_{sim}\right)^2}}{\frac{K_1 + K_2}{2}}, \quad (2.9)$$

An example of a root-mean-squares fit to a conductivity tensor is shown in Figure 2-5 below.

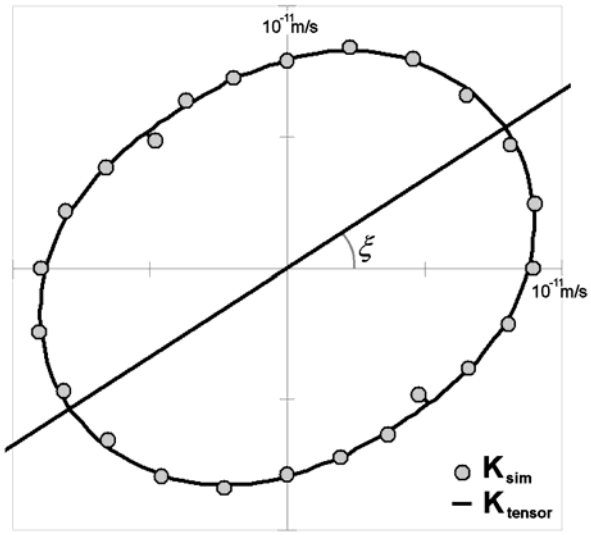

Figure. 2-5. *Fitting a conductivity tensor to simulated directional conductivity values for one realization. K_1 = 9.6 10^{-12} m/s, K_2 = 7.2 10^{-12} m/s, ξ = -35°.*

All normalized fits were then classified into the following three different categories according to how well the conductivity characteristics could be represented by a continuum tensor.

A) $RMS_{Norm} \geq 0.4$ corresponds to a poor agreement between a continuum behavior and the modeling result from the network simulation. A continuum tensor cannot be used to describe the conductivity of these realizations. 5% of the realizations fell into this category.

B) $0.4 > RMS_{Norm} > 0.2$ corresponds to an intermediate region where the behavior is not completely captured by the continuum model but can still with some accuracy be approximated by a tensor. 15% of the realizations were classified into this category.

C) $RMS_{Norm} \leq 0.2$ corresponds to a good agreement between the network simulation result and the continuum approximation and the behavior can be well reproduced by means of a continuum tensor. A vast majority of the realizations (80%) fell into this category.

One example of each category are shown in Figures 2-6a-c, and a summary of all continuum classifications are shown in Figure 2-7.

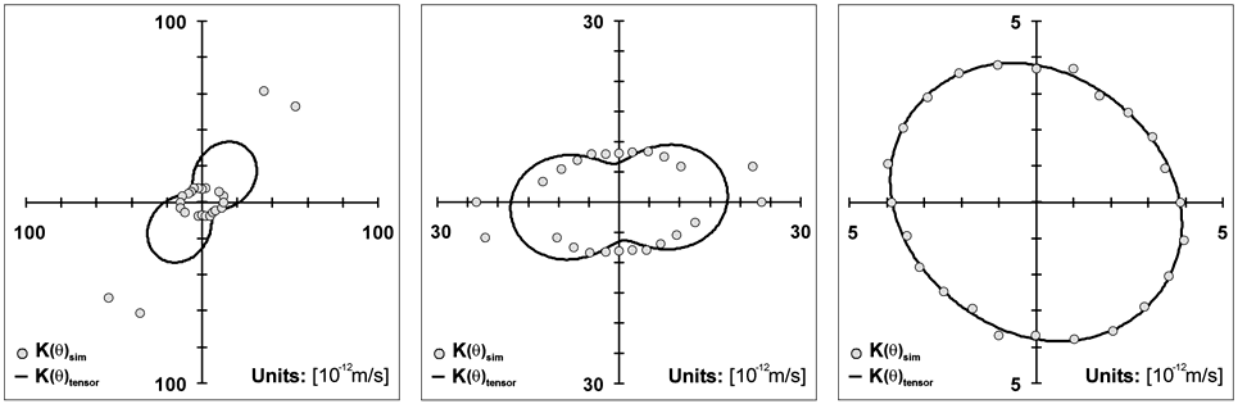

Figures. 2-6a-c*. Examples of continuum-appearance for three fracture network realizations classified as, A, B and C (RMS_{Norm} is 0.86, 0.26 and 0.02), respectively.*

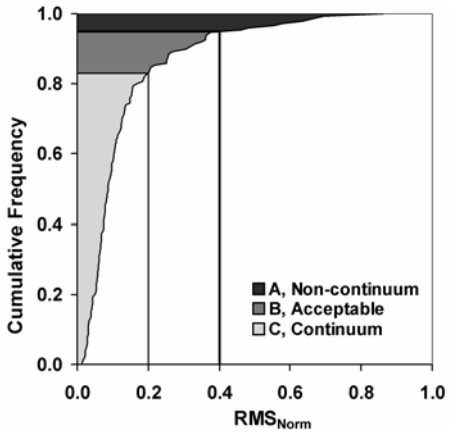

Figure. 2-7*. Summary of continuum-appearance for 150 fracture networks.*

The obtained direction of major principal conductivity, ξ, was found to be a uniform distribution of angles, ie. no dominating direction of high conductivity was found.

Studying the anisotropy K_1/K_2 versus ξ, shows that the horizontal conductivity is somewhat larger in general. Obtained principal conductivity values are shown in Figures 2-8a and b below. The obtained effective conductivities were joined into one probability distribution, $G(K)$, to be used as input for large scale simulations.

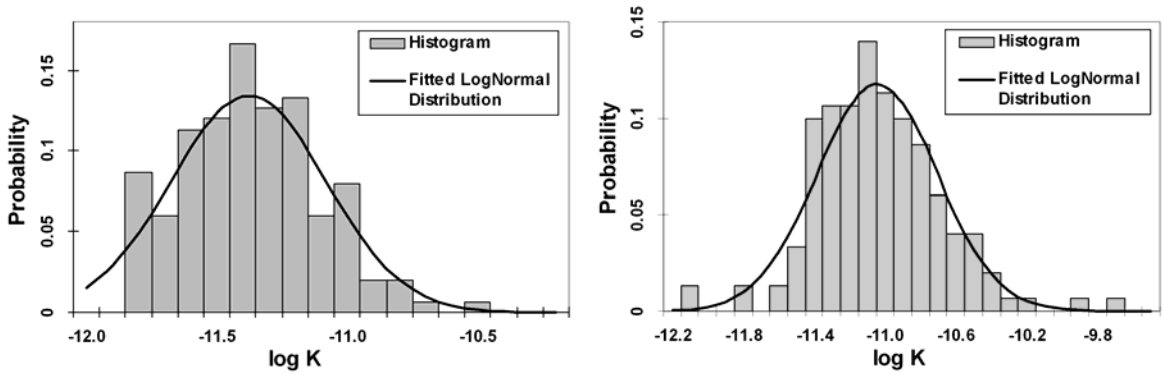

Figures 2-8a and b. *Histograms and fitted lognormal probability distributions of obtained minor principal conductivity (left) and major principal conductivity (right).*

3. Upscaling correlation structures

3.1 Traditional variogram analysis

Correlation structures of the hydraulic borehole data was analysed using GSLIB. As shown in Figures 3-1a and b, the raw data variogram could be fitted to either an exponential model

$$\gamma(h) = 0.52 + 0.48\left[1 - \exp\left(\frac{-3h}{18\,m}\right)\right], \tag{3.1}$$

or a combined exponential and hole effect model

$$\gamma(h) = 0.6 + 0.2\left[1 - \exp\left(\frac{-3h}{30\,m}\right)\right] + 0.2\left[1 + \cos\left(-\pi\frac{h}{22\,m}\right)\right]. \tag{3.2}$$

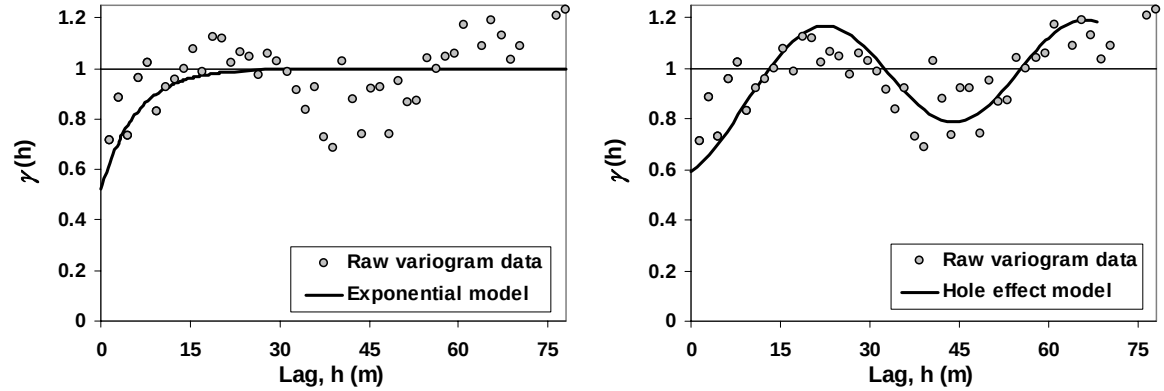

Figures 3-1a and b. *Raw variogram of transmissivity data fitted to an exponential model (left) and a combined hole effect model (right). Lag spacing is equal to packer interval.*

Generating 2D stochastic realisations from these two variograms and analysing them, shows that the input variograms are satisfactorily reproduced by variograms of output. Visual comparisons between the realisations and the original borehole data, reveals that the realisations appear unsatisfactorily "more spatially correlated" than the original data, especially for the lowest permeability values. This indicates that a more sophisticated correlation method should be used.

3.2 Indicator variogram analysis

Studying the permeability histogram, which is generated from the borehole data, indicates that the frequency distribution has a somewhat bimodal appearance. This may in turn indicate that the obtained raw variograms, Figure 3-1a and b, reflect the spatial distribution of two separate permeability populations, rather than the variogram of one homogeneous population. Permeability values less than 10^{-18} are referred to as "Background permeability" (14 %) and those above as "Flowing features" (86 %).

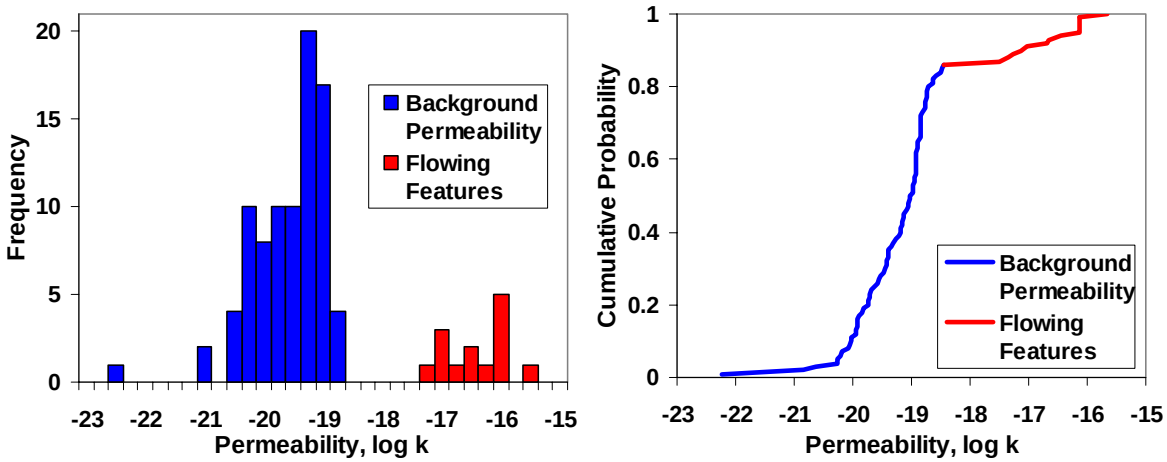

Figures 3-2a and b. *Histogram (left) and cumulative probability (right) of permeability data divided into the populations "Background permeability" and "Flowing Features".*

In order to refine the correlation structures, the background permeability and flowing features are treated as two separate distributions. The borehole data is dissembled into three spatial distributions; indicator values, background permeability and flowing features, as shown in Figure 3-3. The indicator values are set to 1 for a flowing feature and 0 for background permeability. The background permeability distribution origins from the borehole data, but excludes all permeability values above 10^{-18}, and vice versa for the flowing feature distribution.

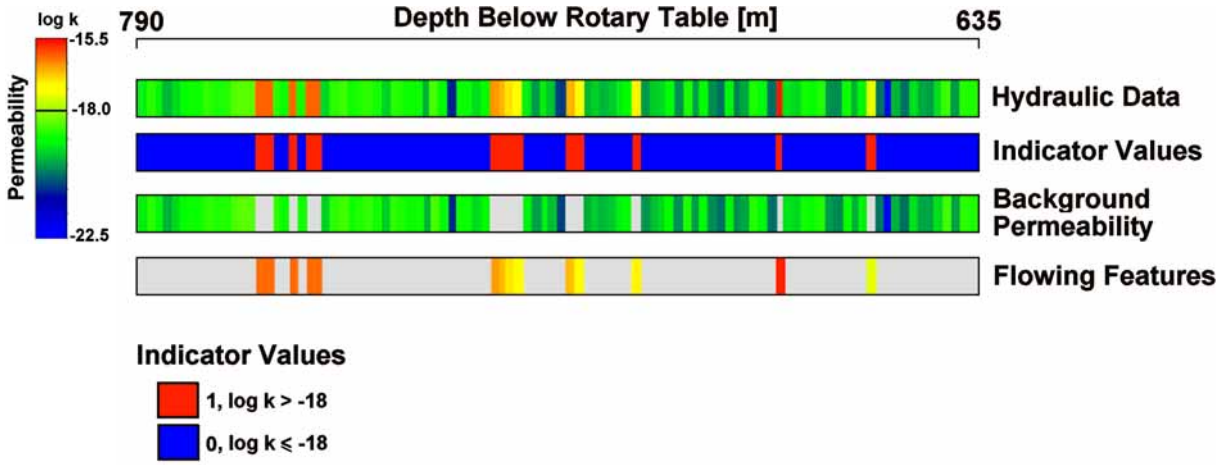

Figure 3-3. *The original borehole data is dissembled into the three spatial distributions, indicator values, background permeability and flowing features.*

Variograms could then be obtained for each of these three distributions, as shown in Figures 3-4a-c. In Figure 3-4a the indicator variogram is compared to the variogram for original the original borehole data. In Figure 3-4b the raw variogram of background permeability is found to be uncorrelated and represented by a pure nugget while in Figure 3-4c the raw variogram for flowing features is fitted to an exponential model. It should be pointed out that large lag spacing must be used for the flowing features variogram in order to obtain representative points, since the measurements are scarce. The close resemblance for the indicator variogram to the original variogram, in Figure 3-4a, and the absence of this resemblance in Figures 3-4b and c supports that indeed the original variogram is dictated by the spatial distribution of two separate permeability populations, rather than reflecting the spatial distribution of one single homogeneous population. The indicator variogram can be fitted with either (3.1) or (3.2). The variance for the total permeability population is 1.25, while for the separate populations flowing features and background permeability it is only 0.303 and 0.365, respectively.

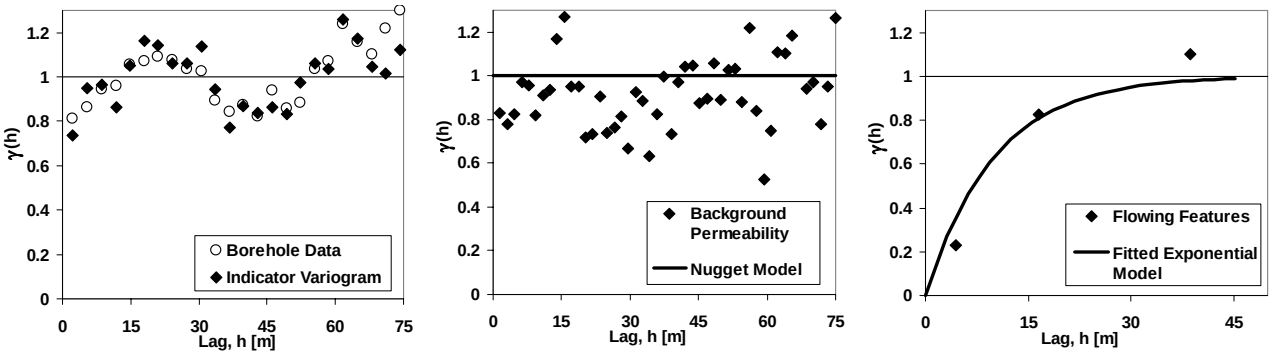

Figures 3-4a-c*. Obtained normalised variograms for indicator values, background permeability and flowing features.*

3.3 Generating stochastic indicator correlated realizations

Having found the more detailed correlation structures, 2D realisations were generated by assembling separate stochastic realisations of indicator values, background permeability and flowing features. The assembly of a total realisation was done just like the original borehole data was previously disassembled, but in the reverse order.

First separate realisations of flowing features and background permeability were generated using the variogram models shown in Figure 3-4b and c. Next a third realisation of indicator values, generated from the exponential variogram model (3.1), was used to decide whether permeability values should be selected from the background or the flowing features realisation in generating the final realisation.

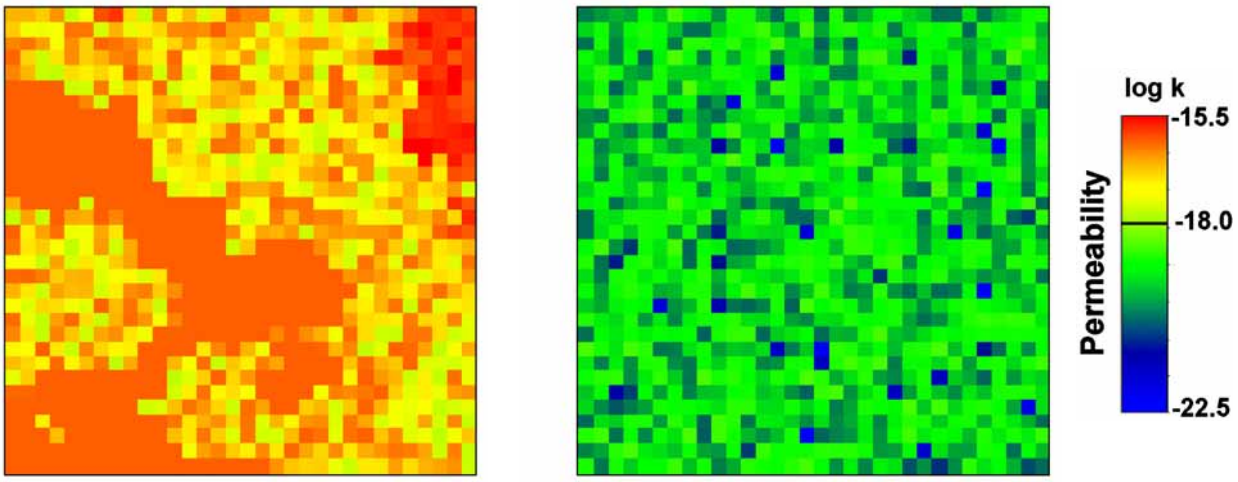

Figure 3-5a and b. *Stochastic 2D realisations of exponentially correlated flowing features (left) and uncorrelated background permeability (right).*

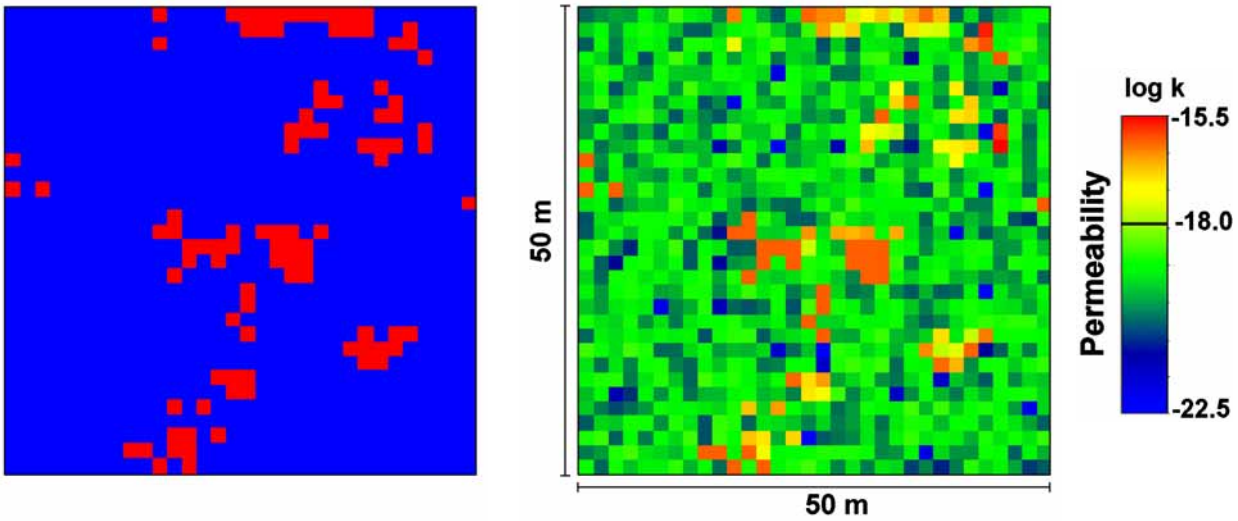

Figure 3-5c and d. *Stochastic 2D realisation of indicator values (left) and the total, assembled, realisation (right).*

Again, the raw variogram of the assembled realisation is validated to the original borehole variogram, but now visual comparisons between the realisations and the original borehole data has improved considerably, as compared to the first attempt based on the simple correlation. The main difference between the two approaches is that in the first, more simple method all spatial correlation is lumped into a single variogram, while in the latter, more complex approach, the internal correlations of both permeability populations are treated separately.

3.4 Upscaling correlation structures for scale of continuum approximation

The obtained correlation structures in the section above are valid for the support scale at the packer interval (1.56 m). In order to produce realisations for transport simulations on the large scale, that are based on results from the DFN simulations, correlation structures must be found that operate on the scale of effective conductivity (7.5 m). Therefore variograms derived from borehole permeability, at the packer scale, must be upscaled to variograms valid for the scale of continuum approximation. Two cases are considered:

i) An exponential variogram model in both vertical and in horizontal directions.

ii) A combined hole effect model in the vertical direction and an exponential model in the horizontal direction. (The reason for using two different models is that using the hole effect model in both directions is not a legitimate positive definite variogram.)

One hundred quadratic 2D realisations, having a side length of 50 m, were generated using the indicator correlation approach described in the previous section. Each permeability realisation was discretized into 36 quadratic elements of 7.8 × 7.8 m^2, as shown in Figures 3-6a and b. Flow simulations were carried out for each element, both in x- and z-direction, using TOUGH2. The derived effective permeability for each element was evaluated by Darcy's law. Next, permeability values within each element are replaced by its effective permeability value. One grid is generated for effective permeability in x-direction and one for effective permeability in z-direction, as shown in Figures 3-7c and d.

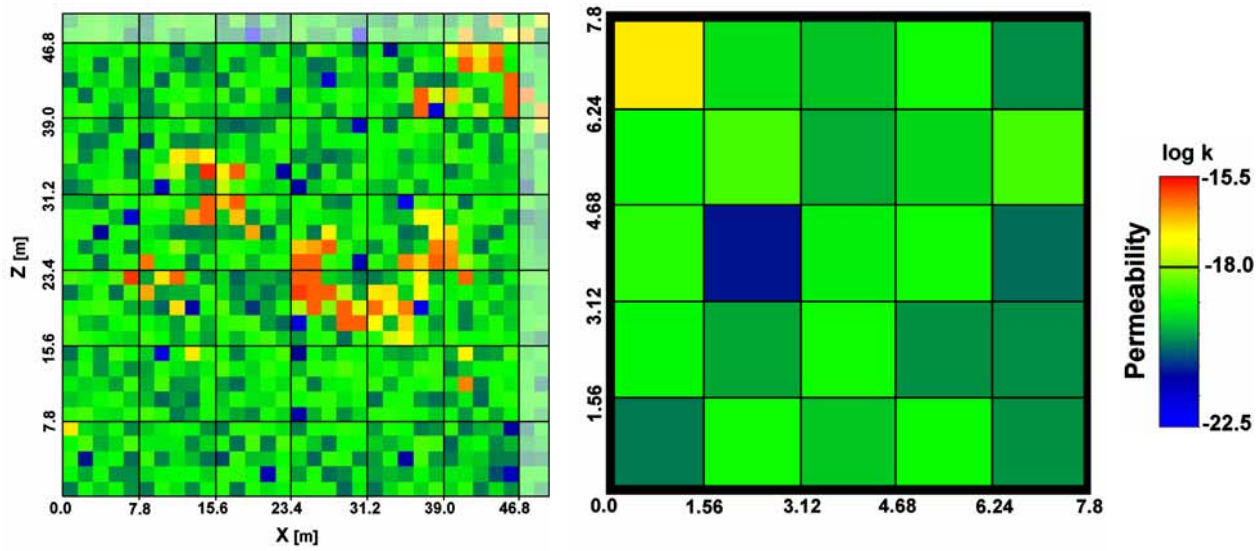

Figures 3-6a and b. *A stochastic realisation is discretized into 36 elements (7.8 × 7.8 m^2).*

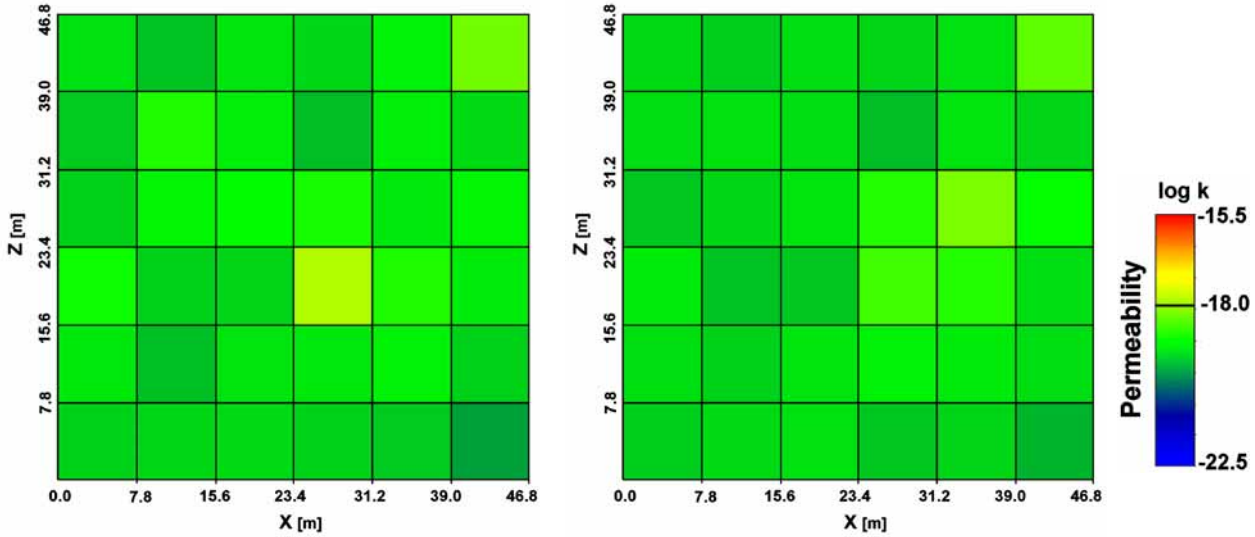

Figures 3-7a and b. *Grids of effective permeability at the element scale are constructed. The left grid contains effective permeability values in x-direction, while the right grid is for effective values in z-direction.*

3.5 Results

Finally, the spatial correlation, in x- and z direction, was examined for each grid of effective permeability, such as Figure 3-7a and b. The resulting raw variograms and fitted models are shown in Figure 3-8 for case i) and Figures 3-9a and b for case ii).

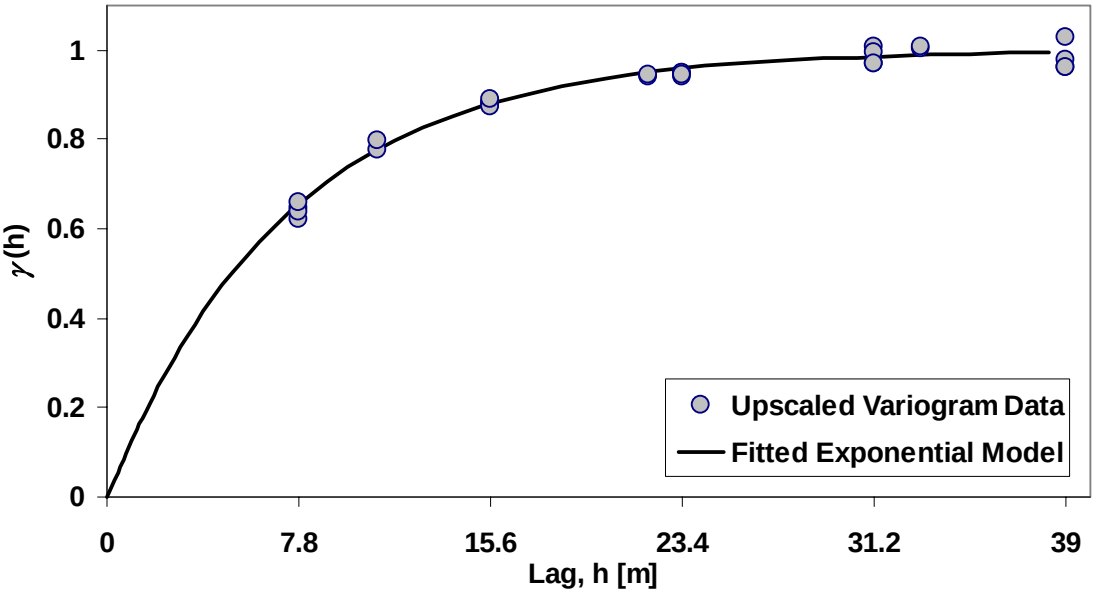

Figure 3-8. *Upscaled variograms for effective permeability in case i).*

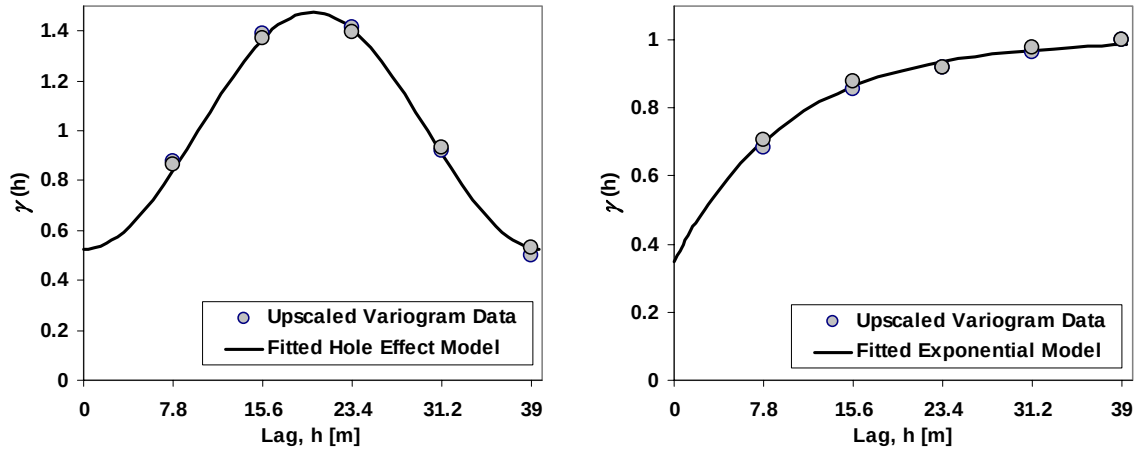

Figures 3-9a and b. *Upscaled variograms for effective permeability in case ii). Upscaled variogram in z-direction (left) and x-direction (right).*

4. Particle tracking at the small scale

In order to obtain distributions of transit times, τ, and transport resistance, β, Cvetkovic (1998), that are needed as input for the large scale particle tracking, we performed particle tracking for fracture networks at the scale of continuum approximation. The small scale particle tracking was done in a similar way as for upscaling the hydraulic conductivity (in the previous section). 30 new cubic network realizations were generated with a side length of 40 m. In each realisation a flow region ($15 \times 7.5 \times 7.5$ m^3) was gradually rotated in a vertical cross section parallel to the large scale modelling plane. A hydraulic gradient of 0.05, which corresponds to the average regional gradient, was imposed over the flow region. No-flow conditions were applied to the boundaries parallel to the large scale modelling plane. A cubic transport region, with side length 7.5 m, was defined at the centre of the flow region, as shown in Figure 4-1.

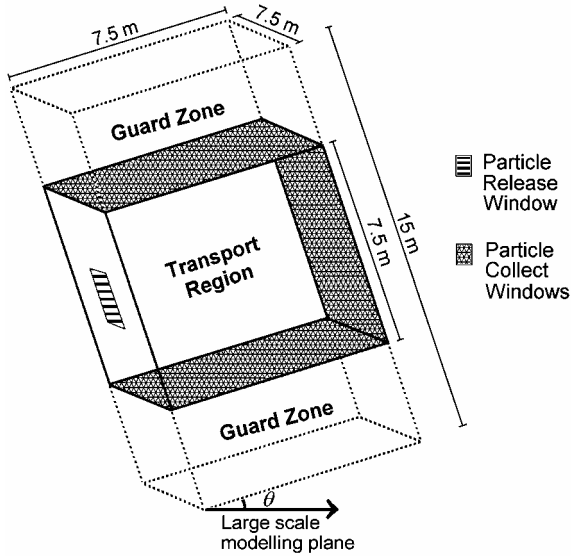

Figure 4-1. *Flow and transport regions vertically rotated in the large scale model plane.*

The purpose for a somewhat larger flow field, in the transverse direction, than the transport region is to have 'guard zones', Jackson, et. al. (2000), and reduce the risk of

allowing particles taking shortcuts to adjacent boundaries. At time t = 0, 10 000 particles were released at nodes within a 2 × 2 m^2 surface, at the centre of the 15 × 7.5 m^2 inflow boundary. The number of particles released is proportional to node flux, which corresponds to an initial constant concentration at the release window. The particles are collected at the remaining sides of the transport region, as shown in Figures 4-2a and b. In total, over 3 million particle travel times were obtained. Perfect mixing at fracture intersections and parallel plate fractures are assumed. A molecular diffusion of 10^{-9} m^2/s was assumed.

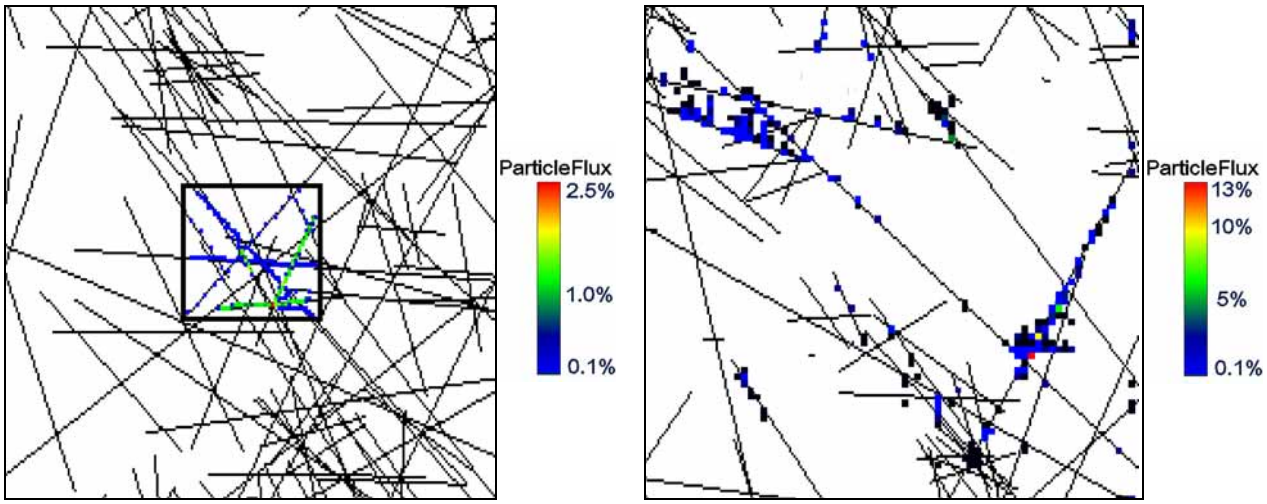

Figures 4-2a and b. *Particle release window (left) and the opposite collect window (right) for one realization.*

As particle tracking on the large scale will be conducted on a heterogeneous conductivity field, we are searching for a general distribution of transit times that can be used for a range of effective conductivity values. We assume that the effective porosity in a high conductivity rock volume is larger, than it is in a low conductive rock volume. Since the particle tracking is conducted under the assumption of parallel plate fractures, effective porosity is the product of P_{32}^{cond} and aperture b. The P_{32}^{cond} value for the flow regions varies somewhat for different realizations and orientations. Following 'the cubic law', Romm (1966), under the assumption of constant P_{32}^{cond} value, the effective porosity is proportional to $K_{eff}^{1/3}$. The assumption may not necessarily be true, since the P_{32}^{cond} value can vary between different transport regions, but on the large scale it is important for modelling a depth trend and THM changes, since these correspond to spatial trends in fracture aperture, only. Under this assumption, the transit time becomes dependent on $K_{eff}^{2/3}$, as opposed linearly dependent on K_{eff}.

In order to obtain a conductivity dependent transit time distribution, to be used as input for heterogeneous conductivity fields in the large scale particle tracking, each travel time was multiplied by the directional conductivity of the transport region to the power of 2/3 and joined into a single probability distribution, $G(\tau K_{eff}^{2/3})$. Similarly, a linearly conductivity scaled distribution for travel resistance, $G(\beta K_{eff})$, was obtained.

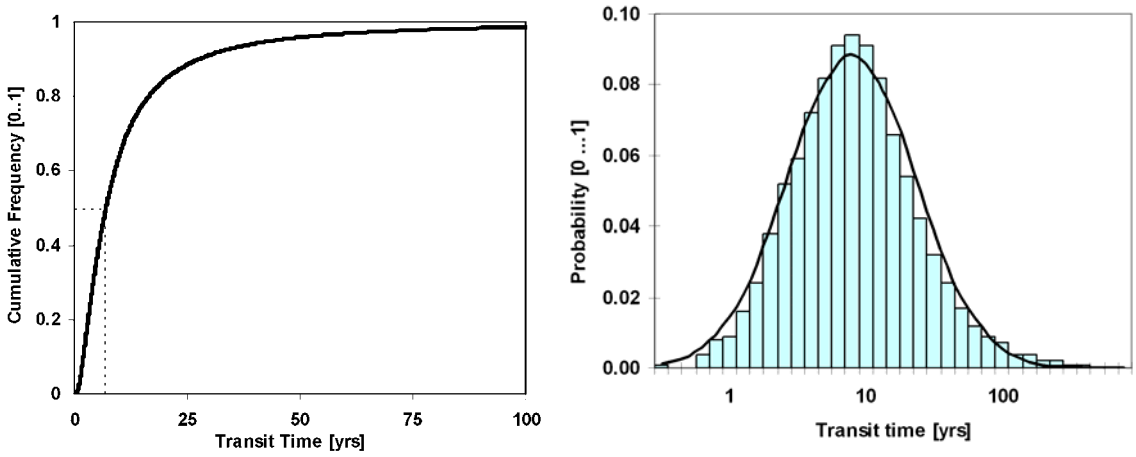

Figure 4-3a and b. *Obtained cumulative and probability transit time distributions applied for geometric mean conductivity (7×10^{-12} m/s) and dh/dx = 0.05. Figure 4-3a is shown on linear scale, while 4-3b is on log-scale.*

5. Particle tracking at the large scale

5.1 Modelling setup

The large scale modelling domain, shown in Figure 5-1, was discretized into cubic blocks with side length 7.5 m, to be consistent with the upscaled hydraulic input data, obtained in section 2. Element conductivity was stochastically assigned from the obtained probability distribution $G(K_{eff})$, and correlated with the upscaled exponential variogram described in section 3.

The region to the left of the fault zone, $0 < \times < 2475$ m, was discretized into coarser elements, having a side length of 45 m. These elements were assigned a separate conductivity distribution, which has been upscaled to 45 m by separate stochastic continuum simulations. The reason for a coarser grid is to save simulation time, since no particle tracking will take place within this region. The coarseness has little impact on the large scale flow due to the geometry of the modelling region and the conductive fault zone.

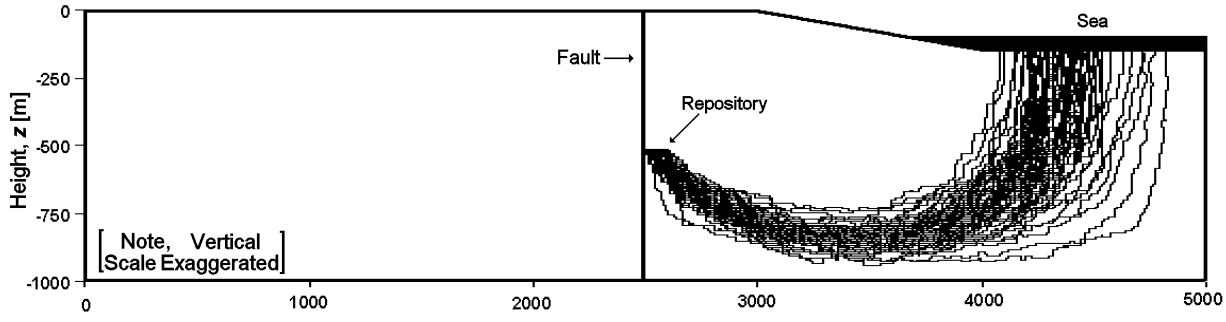

Figure 5-1. *Domain for large scale stochastic continuum transport simulations (5 km x 1 km). The region to the left of the fault is dicretized into large elements. The remaining region is discretized into elements of effective conductivity scale.*

The hydraulic upscaling, described in section 2, was carried out for the lower formation, since both the borehole hydraulic data and the loading/unloading fracture aperture measurements are measurements form the lower formation. However, high upscaled

permeability values (40 m scale) are given for the top 50 m of the upper formation. Lacking detailed information about the upper formation, we have decided to superimpose a conductivity depth trend for the upper formation.

Figure 5-2a shows all available data (Near surface BVG and undifferentiated BVG conductivities at the 40 m scale and borehole data measured at the 1.56 m scale). The Figure also includes the depth trend of fracture transmissivity that is observed in *in-situ* TM modelling (which is a function of overburden weight). Figure 5-2b shows the geometric mean and standard deviation of obtained effective conductivity at the 7.5 m scale in the lower formation, as described in section 2, and it also shows the conductivity depth trend superimposed for the upper formation. The depth trend is unable to reach the high conductivity values of the Near surface BVG. The most probable reason for this is that the core data used for the loading/unloading fracture aperture measurements origin from depths larger than 800 m.

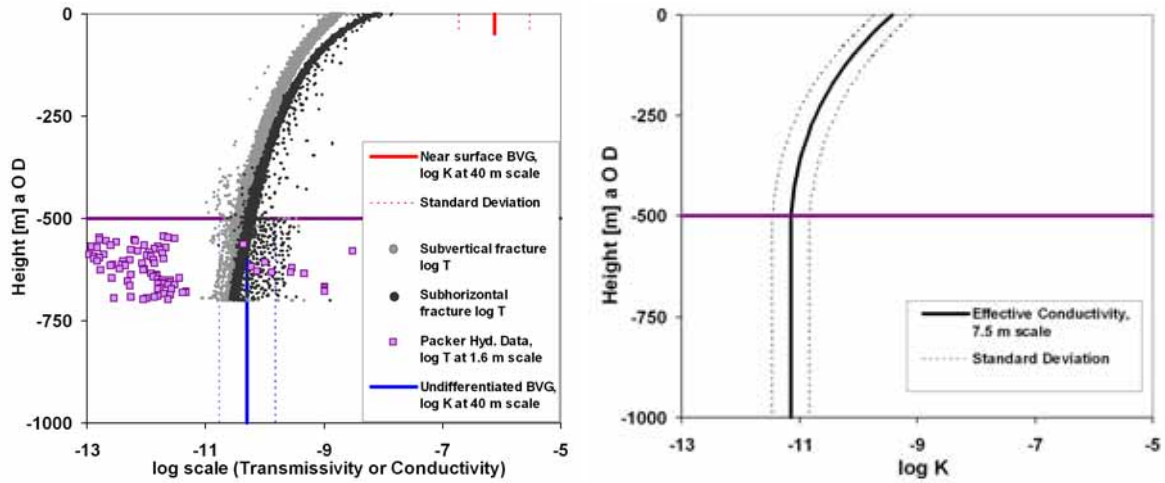

Figures 5-2a and b. *Available data and results from TM simulations indicating higher conductivity values in the upper formation (left) and applied conductivity depth trend for large scale simulations.*

Using head fields and vertical and horizontal flux fields extracted from steady state solutions of large scale simulations, the particle tracking was performed according to the following scheme, shown in Figure 5-3. First a particle is released at the nodal point, the centre, of a random element within the repository region. The particle then moves from the present element, in direction i, to an adjacent nodal point with probability, P_i, proportional to the fraction of the total outward directed flux in that direction, Q_i^{out}, as defined in Equation 5.1 below.

$$P_i = \frac{Q_i^{out}}{\sum_i Q_i^{out}} \qquad (5.1)$$

The effective conductivity of the rock volume for the movement, K_{eff}, is calculated from the flux, Q_i, the local hydraulic gradient, $\Delta H/\Delta x$, and the cross section area, A, using Equation 5.2 below.

$$K_{eff} = \frac{Q_i}{\frac{\Delta H}{\Delta x} A} \tag{5.2}$$

The transit time for the movement, τ, is randomly taken from the conductivity independent distribution for transport times, $G(\tau K_{eff}^{2/3})$, previously obtained from the small scale modelling and scaled with $K_{eff}^{2/3}$, from Equation 5.2, and the deviation between the regional hydraulic gradient of 0.05 and the local hydraulic gradient, ΔH/Δx, as shown in Equation 5.3.

$$\tau = \frac{G\left(\tau K_{eff}^{2/3}\right)}{\left(K_{eff}\right)^{2/3}} \frac{0.05}{\frac{\Delta H}{\Delta x}} \tag{5.3}$$

The particle keeps moving through 7.5 m blocks until reaching the sea, which is the only outflux boundary. The total travel time is calculated as the sum of transit times for each movement. For every large scale realization 100 000 particles were released, yielding a distribution of total travel times. Transport resistance, β, was calculated in a similar way, except linearly scaled with K_{eff}.

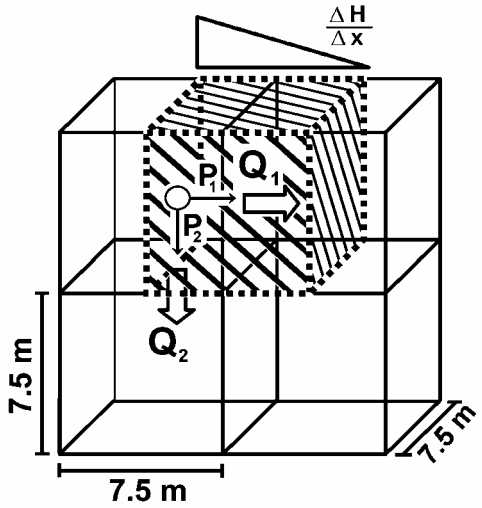

Figure 5-3. *Illustration of particle tracking scheme for an element with two outward fluxes. The effective conductivity region for a horizontal movement is shown striped.*

5.2 Results

Transport simulations were carried out for cases of homogenous effective conductivity, stochastic heterogeneous conductivity, correlated conductivity fields. Results from these cases also compare the effect of including the depth trend. The depth trend is found to increase travel times, even though it causes hydraulic conductivity to increase with height. The reason is that the depth trend changes the flow field such that the plume is forced downwards, and thus takes a longer route.

Results from one stochastic realization are shown in Figures 5-4a and b below. Average travel times are on the order of 10 000 years.

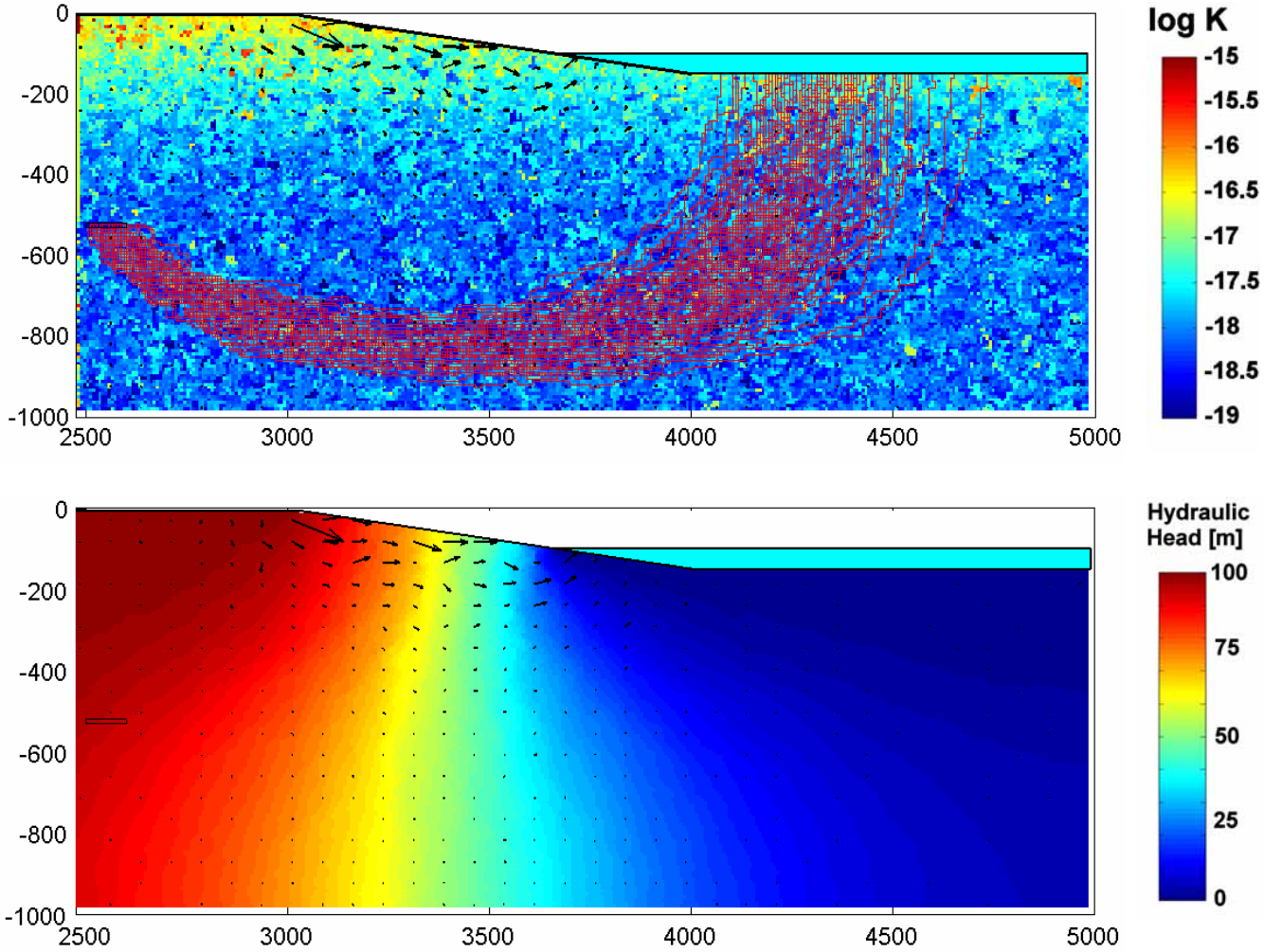

Figure 5-4a and b. *Simulated particle pathways for one large scale correlated stochastic conductivity realization (above) and corresponding head and flux fields (below).*

6. Mechanical and thermo-mechanical simulations

This chapter describes the mechanical and thermo-mechanical simulations that have been performed. The aim was to get an estimate of the changes in joints hydraulic aperture due to the repository excavation and filling with swelling material. Changes in hydraulic aperture are then related to changes in fracture transmissivity, using the 'cubic law', and transferred to the 3D fracture networks, described in section x. The TM effects on effective conductivity can then be evaluated by repeating the small scale flow simulations for these modified networks.

The effect on installation of a slowly decaying heat source, representing the array of waste canisters, was modelled as a separate case. The geometry of the fracture system was greatly simplified for enhance the computational efficiency. The obtained normal stress values were stored for hydraulic modelling.

6.1 Input data interpretation

The assumptions and simplifications made in mechanical modelling are:
- 2D modelling of 3D- reality (joint directions, infinite length of the model)
- assumption of linear elasticity of intact rock
- simple rock joint models
- repository excavation and filling is not modelled in detail

These simplifications can be justified with our aim to understand the modelling process rather than model any specific real-world case in detail.

6.2 Boundary conditions

The 2D model is oriented in the direction of maximum horizontal stress. Thus, the minimum horizontal stress is perpendicular to the model. The *in-situ* stresses depend on the depth D [m], (Nirex 1997e):

$\Phi_{vertical}$	0.02494D+0.26622	MPa
Φ_{Hmin}	0.019961D-0.31619	MPa
Φ_{Hmax}	0.03113D+1.88747	MPa

In the model, the displacements are prevented in normal direction of model outer boundaries and freely allowed in the direction of the boundaries. The top of the model is free. The model width is 1100 m and the height 700 m (Figure 6-1). The model size was reduced from the original 5 km x 1 km size to speed up the modelling.

The thermal boundaries are adiabatic (insulated) on the sides of model and the temperature is fixed at top and at bottom of the model. The surface and seawater temperature is 11 ^{o}C and the adiabatic lapse rate is 6.2 ^{o}C/km. A separate thermal model, 2.1 km wide and 1 km high was used for modelling heating periods longer than 3 years.

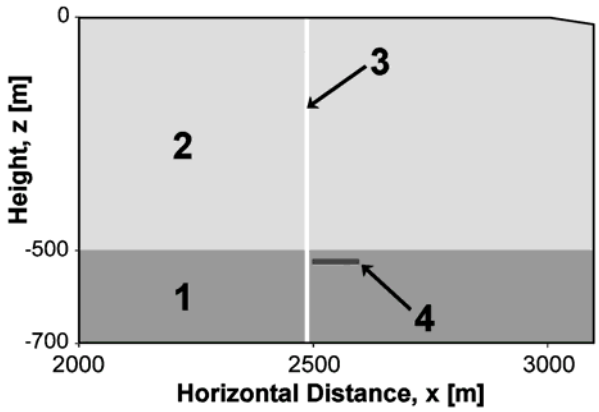

Figure 6-1. *Thermo-mechanical modelling domain, 1100 × 700 m. The materials are: 1) Bulk Longlands Farm Member, 2) Altered Longlands Farm Member, 3) fault zone (thickness 5 m) and 4) the repository (100 m x 10 m)*

6.3 Rock jointing

There are four fracture sets in the each rock types modelled. One of these sets is close the modelling plane and is therefore excluded from the modelling. The three other sets are not exactly perpendicular to the modelling plane, and 3D-2D -conversion is needed. Here the selected conversion method is to "rotate" the fracture set dip directions to the perpendicular position (Figure 6-2), which leaves the dips of the fracture sets unchanged.

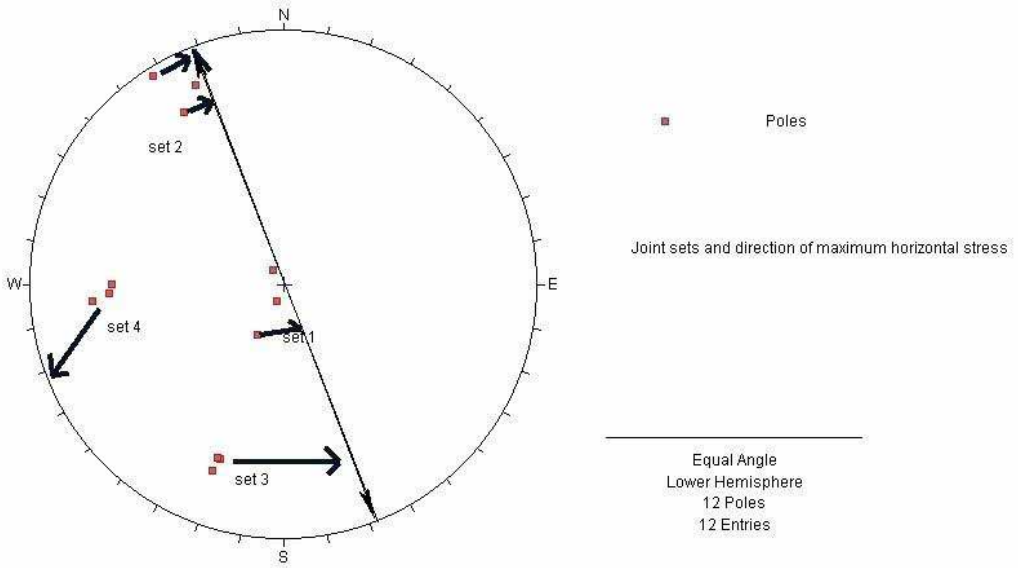

Figure 6-2. *The modelling plane is directed parallel to the direction of the maximum horizontal stress. The fracture set 4 is almost parallel to the modelling plane, and can be excluded in modelling. The other sets are "rotated" to perpendicular direction to the modelling plane while keeping the dip unchanged.*

The mean joint spacing is used for modelling the rock structure. When a large number of joints and rock blocks are modelled, they are rather generated automatically than defined individually. The modelling code (UDEC) prefers convex-shaped distinct elements to the

concave shapes, when the numerical stability of the solution is considered. Joints with infinitive length produce only convex shapes, and thus very long joints are the obvious starting point for model generation. Because the Fault Zone thickness is only 5 m, it was modelled with two vertical fractures 5 m apart and one flat dipping joint set.

6.4 Intact rock properties

The intact rock properties (Table 6-1) were selected from provided data. The wire line data was used for Young's Modulus and Poisson's Ratio, because the core data was available only for Formation 1. The mean values for all three rock types were used for modelling.

Table 6-1. *Intact rock properties*

Material properties	Formation 1 Bulk Longlands	Formation 2 Altered Longlands	Fault Zone
UCS (MPa)	157.0	39.6	128.4
Young's Modulus (GPa)	69.08	46.93	62.62
Poisson's Ratio	0.263	0.287	0.262
Bulk modulus K (GPa)	48.58	36.72	43.85
Shear modulus G (GPa)	27.35	18.23	24.81
Density (kg/m^3)	2750	2650	2730

6.5 Joint properties

The initial (non-scaled) joint properties (Table 6-2) were estimated with provided data. The mean values were used also here. The concept of instantaneous cohesion and friction (Hoek *et. al*., 1995) was used for values of joint cohesion and friction angles. These values were obtained as secant values between the minimum and maximum in-situ rock stress values on modelling plane at repository depth. Because it was not possible to model the vast number of joints in reality in large-scale model, the joint normal and shear stiffness were scaled in modelling with the ratio between joint spacing (actual joint spacing / modelled joint spacing). The ratio used here was 1/50.

Table 6-2*. Initial joint properties*

Joint properties	Formation 1 Bulk Longlands	Formation 2 Altered Longlands	Fault Zone
Normal stiffness (GPa/m)	434	434	434
Shear stiffness (GPa/m)	434	434	434
Basic friction angle (E)	33.0	33.1	31.4
JRC_{300}	3.85	4.2	4.22
JCS_{300} (MPa)	112.21	55.3	103.81
Apparent cohesion (MPa)	0.69	0.74	0.74
Apparent friction angle (E)	34.6	33.5	33.0

The test data provided contained conductive aperture - normal stress curves for two core samples. Only the apparently consistent parts of the curves were used. The maximum and

minimum aperture curves were plotted (Figure 6-3), and an approximation for normal stress - conductive aperture relationship was constructed (6.1),

$$b = \frac{27}{(\sigma_n+1)^{0.66}} \ , \tag{6.1}$$

where b is hydraulic aperture [μm] and σ_n is normal stress [MPa]. The approximation falls well within the test results, and produces a positive aperture value for any compressive normal stress.

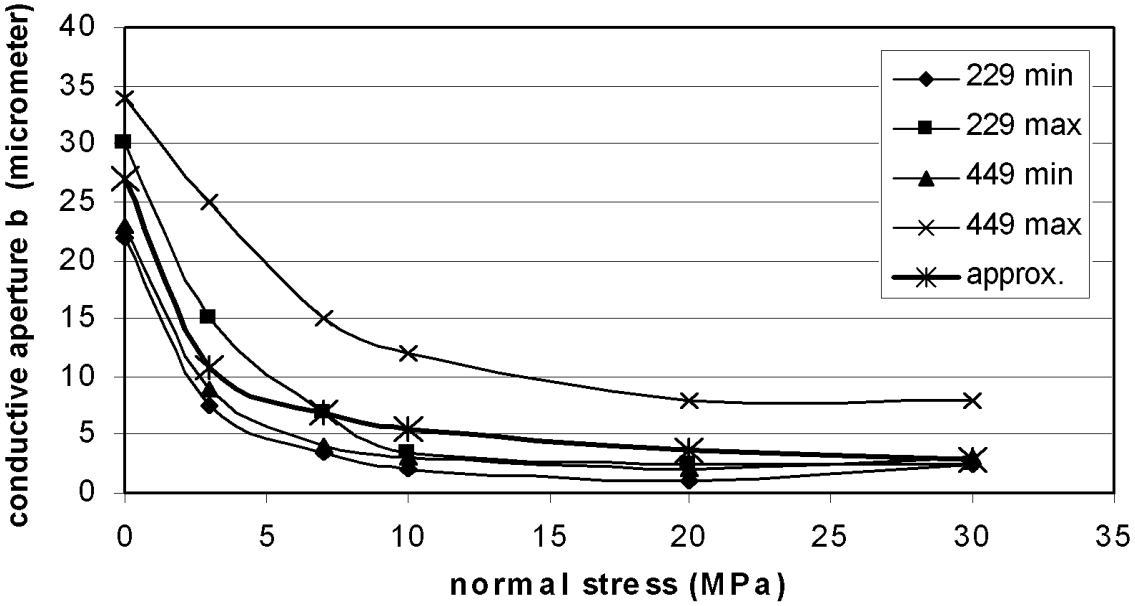

Figure 6-3. *The normal stress – conductive aperture curves for samples 229 and 449 and the approximation used for aperture calculations.*

6.6 Modelling

The model (Figure 6-1) consists of 5853 fully deformable, elastic 2D distinct element blocks and 21077 finite difference zones (elements). First the model was cycled to equilibrium state. Then the excavation of the repository was modelled by reducing the material stiffness and in-situ rock stress to 75% of the initial values in the repository area. The 75% value of remaining stiffness and rock stress is a rough estimate based on assumption that the repository excavations are parallel to the modelling plane and excavation ratio of 25%. The excavations are supposed to be designed to prevent any inelastic rock deformation. In this phase of modelling, the joint normal and shear displacement record is reset. This has no effect on the calculation of stresses.

The thermal modelling was executed as a separate run of the distinct element model. The heating power of the waste is uniformly distributed across the entire repository area, resulting initial power value 0.6 W/m^3. For first three years time the power remains practically constant, and fixed power of 0.6 W/m^3 was used in the modelling. A decaying total heating power was determined for longer modelling times (Figure 6-4).

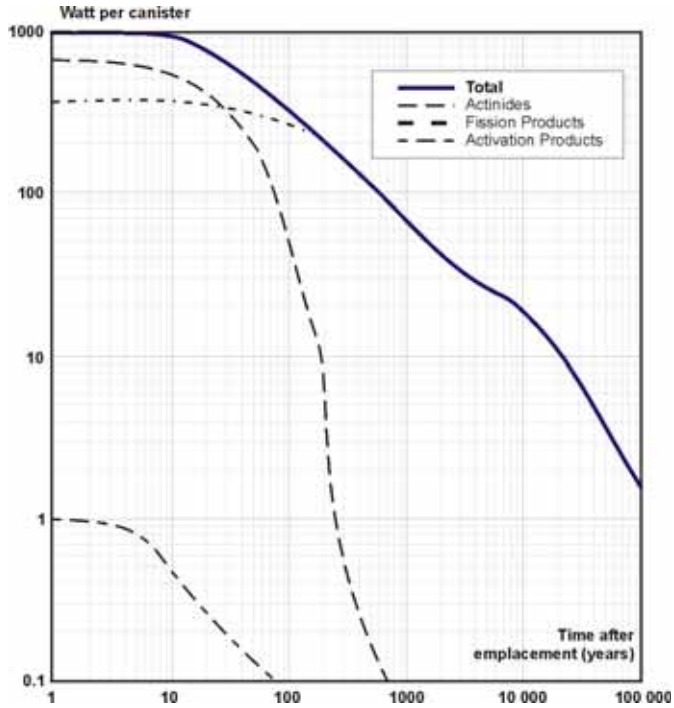

Figure 6-4. *Heat evolution versus time for a single canister, extracted from Andersson and Knight (2000).*

Because the fully coupled thermo-mechanical model has very short critical timestep length, the computation of long time periods needed here is very ineffective. Thus for time periods longer than 3 years one-directional coupling was applied. Because the rock stresses or displacements have virtually no effect on temperature distribution (in this case, at least), this simplification is justified. The temperature distribution was calculated first with simple, 2.1 km x 1.0 km size continuous model. Then the resulting temperature distribution was transferred into coupled distinct element model, and the resulting normal and shear stresses in the modelled joints was calculated.

6.7 Results

The excavation of the repository and the 2 MPa swelling pressure of filling material have only minor effect on the stress state around the repository area. Anyway, one must remember that the details of the repository were not modelled. The secondary stresses due to excavation and also due to swelling pressure of the fill can have significant effects in the scale of deposition tunnels and holes, depending on the detailed design.

The decaying heat power increases the temperatures of the rock first and later the temperature decreases towards to the original value. The temperature evolution varies at different locations (Figure 6-5a). At and near the repository the temperature elevation is fast, and so is also the decaying (Figure 6-5b and Figure 6-6a). At locations further away from the repository, temperature changes are smaller and rather uniform (Figure 6-6b and Figure 6-6c).

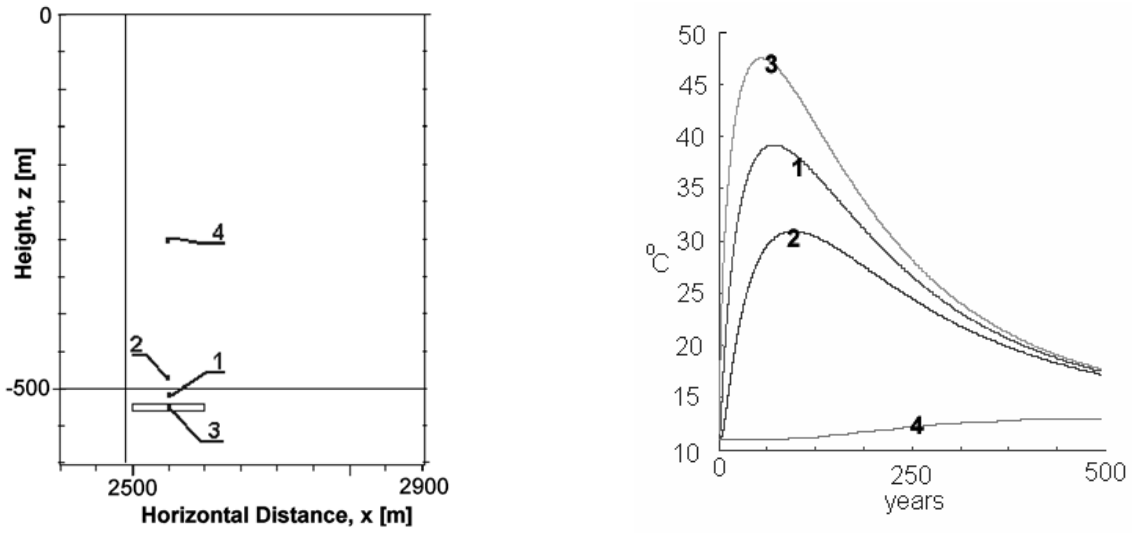

Figure 6-5a and b. *Temperature history recording points (left) and temperature evolution at those points during first 500 year heating.*

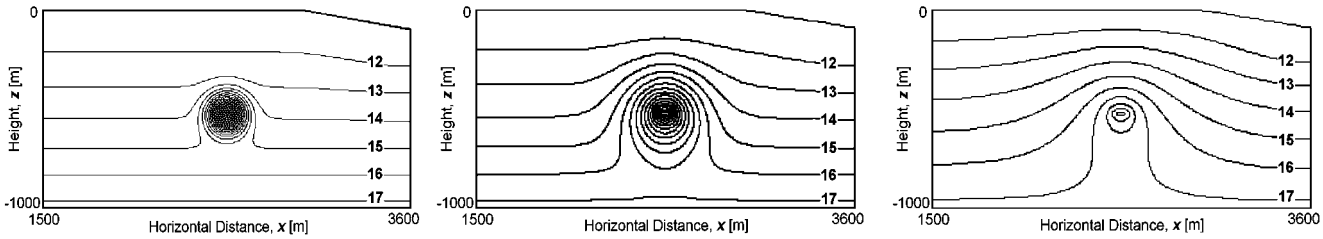

Figure 6-6a-c. *Temperature contours (℃) around the repository after 100, 500 and 10 000 years heating, respectively.*

The effect of long-term heating is visible at the vicinity of the repository. Because the thermal expansion of the rock increases the compressive stresses near the repository, the apparent apertures decrease about 10-15% during first 100 year heating (Figure 6-7).

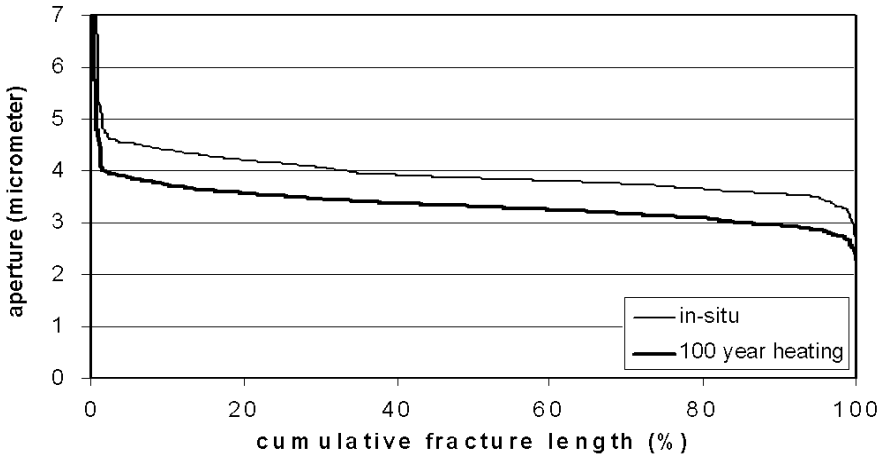

Figure 6-7. *Effect of heating on fracture aperture within 20 m distance from the repository.*

The change in hydraulic aperture can then be related to change in fracture transmissivity, ΔT [%], as shown in Figure 6-8a for the case of excavation and swelling of backfilling material and in Figure 6-8b at 100 years of heating. Changes within the fault zone were excluded from this analysis, since no detailed hydraulic upscaling has been done for the fault. Also, transmissivity changes inside the repository were excluded, as bentonite properties will be applied for this region in the large scale modelling.

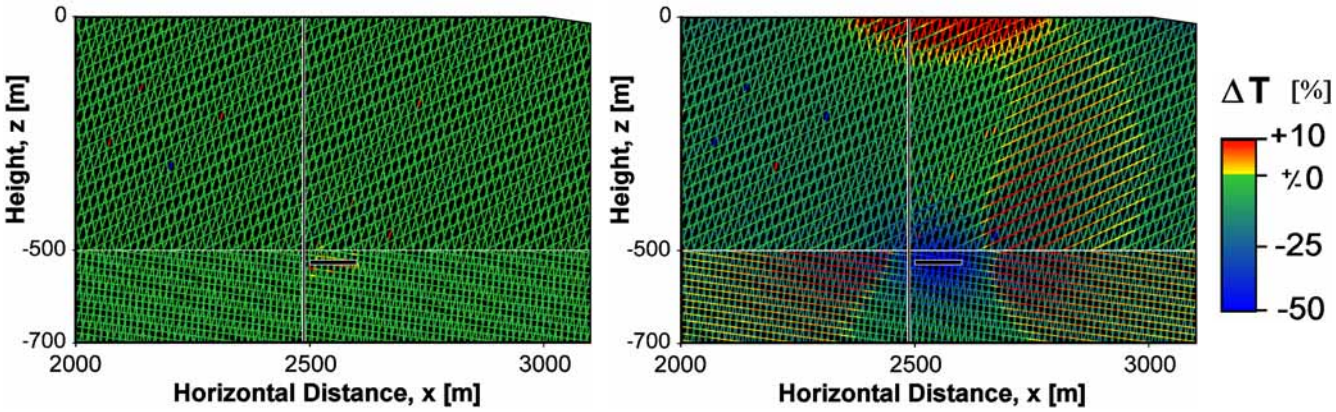

Figure 6-8a and b. *Mechanical effect (left) and thermo-mechanical effect (right) related to change in fracture transmissivity, ΔT [%].*

As can be seen in Figure 6-8a, the M effects due to repository excavation and swelling of back filling material are small, which is why we focus on TM effects at 100 years of repository heating in the lower formation. The changes in fracture transmissivity in Figure 6-8b can be approximated as a function of radial distance from the repository centre, *r*, are shown in Figure 6-9.

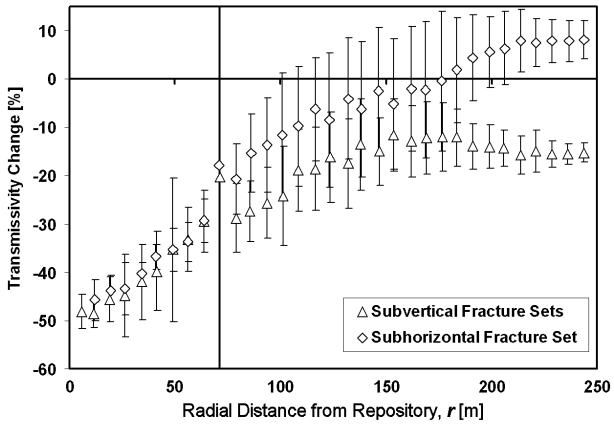

Figure 6-9. *Fracture transmissivity change due to 100 years of heating, as a function of repository distance, divided into 7.5 m intervals.*

A distortion can be seen at *r* = 70 m, which is caused by two fractures, partly inside the fault zone. The most interesting locations for further study was decided to be at *r* = 15 m, where transmissivity is reduced by a factor 2, and at *r* = 180 m, where sub-vertical fracture transmissivity is slightly decreased, while sub-horizontal fractures show a slight increase.

7. Impact of TM effects on transport parameters

7.1 TM effects on small scale conductivity

The statistics for transmissivity change at the two locations r = 15 m and r = 180 m, as discussed in the previous section, were transferred to 10 small scale fracture network realisations. The realizations were selected so as to represent different cases of anisotropy and classification of continuum-appearance. Since the 2D TM modelling excluded the fracture set parallel to the large modelling plane, no changes were applied for this set in the 3D hydraulic modelling. The small scale upscaling procedure was then repeated for these modified fracture networks, as described in section 2, to evaluate the TM impact on directional conductivities. The results are shown below in Figures 7-1a and 7-1b.

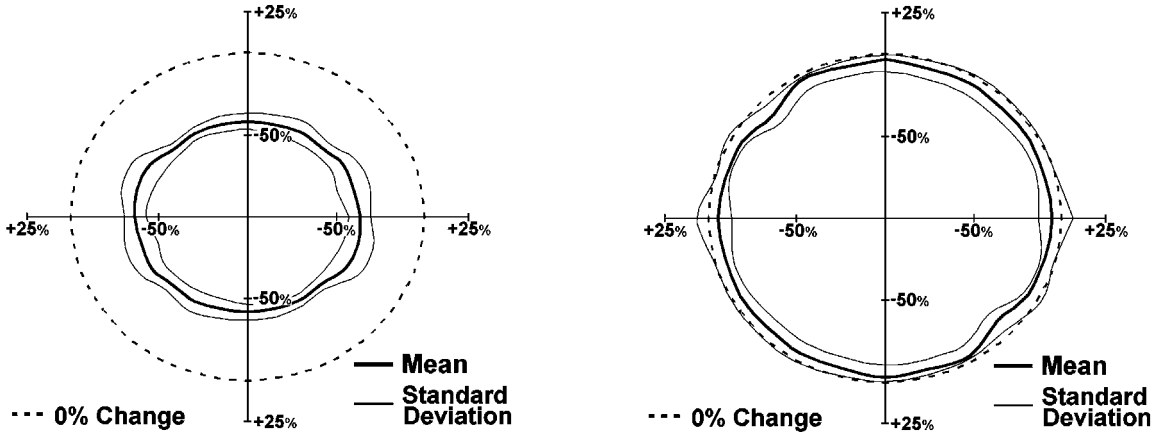

Figures 7-1a and b. *Change in directional conductivity for 10 small scale realizations at 15 m distance from the repository (left) and at 180 m distance (right).*

As can be seen in the Figures above, the effect of 100 years heating reduces the effective conductivity at the 7.5 m scale by 40 % near the repository and by 5 % at 180 m distance. Close to the repository, the results only show small changes in continuum behaviour. The most probable reason for the slight discontinuum increase is that transmissivity was halved for three sets, but left unchanged for the fourth. At 180 m distance no changes in continuum appearance can be observed. Even though sub-horizontal and sub-vertical fractures are given different transmissivity changes at 180 m distance, as shown in Figure 6-9, no anisotropy increase can be observed in Figure 7-1b. This is probably due to the fact that fracture sets have a large deviation around the mean angle.

The effective conductivity seems to follow the overall fracture transmissivity reduction. Figure 7-2 shows changes in effective conductivity, average fracture transmissivity change (disregarding orientations for fracture sets) and a fitted trend. Assuming the excluded fracture set to undergo similar transmissivity change, as do the modelled sets, it seems likely that the changes in effective conductivity should follow the trend in Figure 7-2.

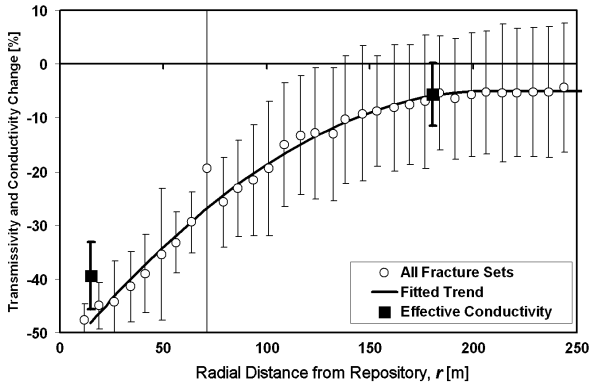

Figure 7-2. *Change in fracture transmissivity, a fitted trend and resulting effective conductivity, for repository distance divided into 7.5 m intervals.*

7.2 TM effects on large scale particle tracking

The trend in effective conductivity change, shown in Figure 7-2, was superimposed to large scale transport simulations as a "permanent conductivity change", which yields an upper estimate of TM impact on travel times and transport resistance. Average transit time and transport resistance, for the quantiles: 0-10%, 10-20%, 20-40%, 40-60% and 60-100%, were calculated for 100 000 released particles. Our results for 10 large scale realizations indicate that the transit time increase at the most by 5%, while the transport resistance increases by approximately 8 % as shown in Figures 7-3a and b.

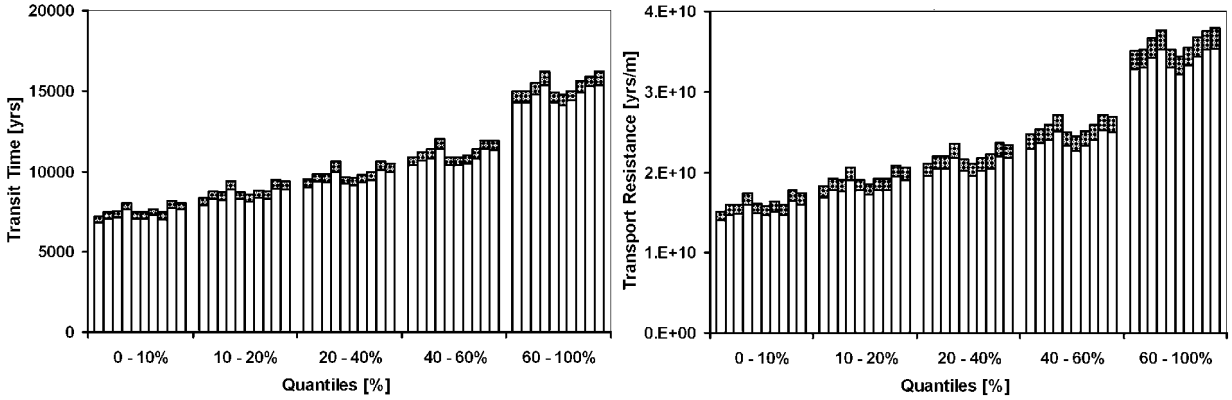

Figures 7-3a and b. *TM effect on transit time (left) and on transport resistance (right) for 100 000 particles tracked in10 large scale realizations. The TM effects are marked as shaded in the Figures.*

TM effects on the transport properties were also studied separately at a 50 m radial distance from the repository, as shown in Figures 7-4a and b and Figures 7-5a and b. The transport resistance calculated at a 50 m radial distance may increase as much as 25 %, as shown in Figure 7-5b.

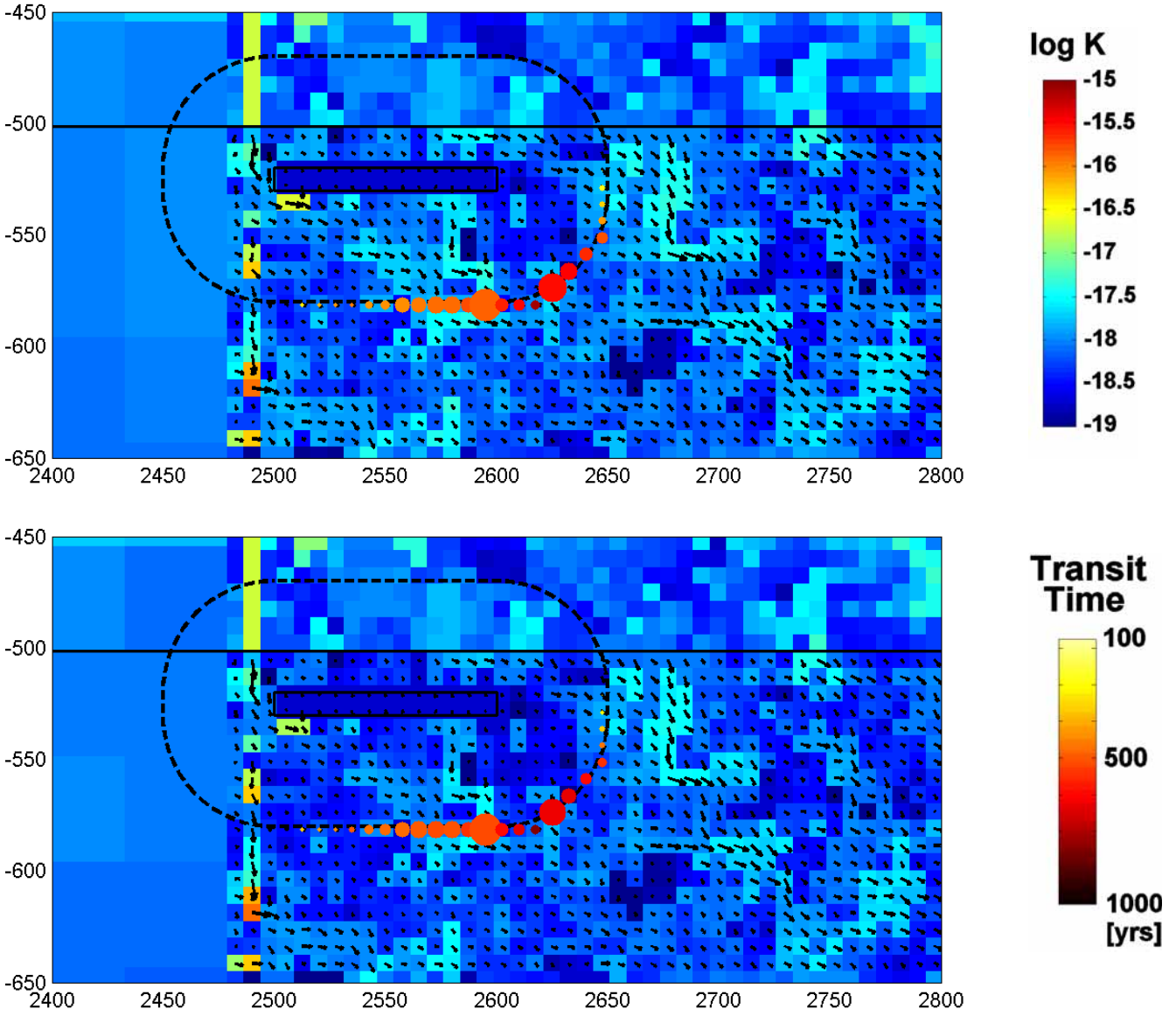

Figures 7-4a and b. *Transit times for100 000 particles collected at 50 m distance from the repository, excluding TM effects (above), and including TM effects (below). The dot size corresponds to number of particles collected, while colour corresponds to mean transit time.*

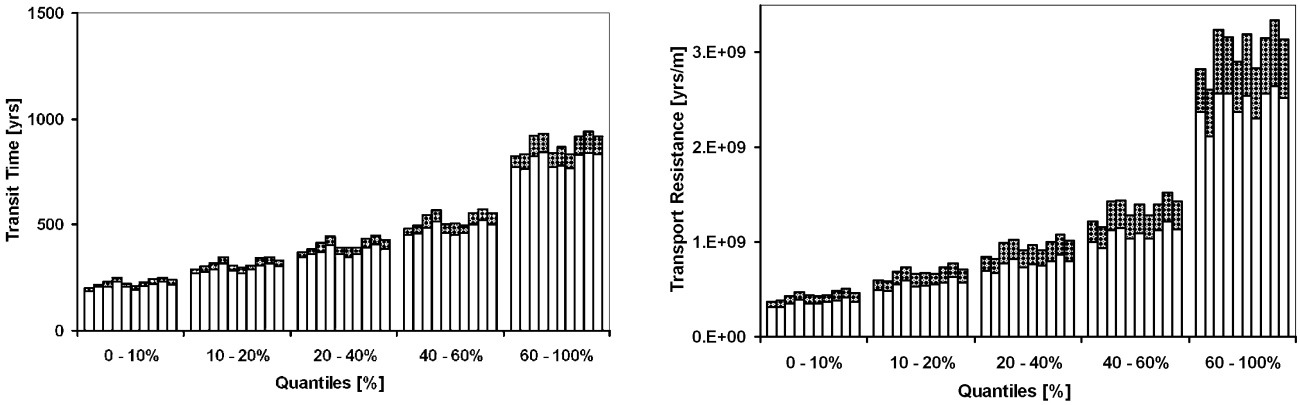

Figures 7-5a and b. *TM effect on transit time (left) and transport resistance (right) at 50 m distance from the repository, for 100 000 particles tracked in10 large scale realizations.*

8. Concluding remarks

The previous sections present the work done to solve the upscaling THM Bench Mark test for DECOVALEX III. The results demonstrate that based on the available data a range of hydraulic properties can be derived for the hydraulic fracture networks. The continuum-appearance, in section 2, was found to depend on (i) which of the possible hydraulic characteristics are assumed for the fracture transmissivities and (ii) what block scale is used in the network flow simulations. In this approach, we have neglected the fact that at least 5 % of the network realizations proved to be of non-continuum type. The correlation structure derived from the variogram analysis, in section 3, can be approximated by at least two different models.

Results from mechanical simulations, in section 6, indicate that aperture changes due to excavation and bentonite swelling are negligible. The thermo-mechanical simulations including heat emission from the disposed waste show a larger effect on fracture aperture.

Transferring the TM effects on hydraulic properties in the large scale transport model indicates that the impact is small, in comparison to the intrinsic uncertainties in modelling hydraulic flow in fractured rock.

References

Andersson, J. and J. L. Knight, The THM Upscaling Bench Mark Test 2 - Test Case Description.- Knight, J. L. (ed.), United Kingdom Nirex Limited, Harwell, 2000.

Armitage P., D. Holton., N. L. Jefferies, B. J. Myatt, and P. M. Wilcock, Groundwater flow through fractured rock at Sellafield, Final report, E.C. publications, Nuclear Science and Technology Series, EUR 16870 EN, 1996.

Baecher, G. B., N. A. Lanney and H. H. Einstein, Statistical Description of Rock Properties and Sampling, Proceedings of the 18th U.S. Symposium on Rock Mechanics, American Institute of Mining Engineers, 5C1-8, 1977.

Barton, C. C., Fractal Analysis of Scaling and Spatial Clustering of Fractures, Fractals in Earth Sciences, Plenum Press, New York, 1995.

Cacas, M. C., E. Ledoux, G. de Marsily, B. Tillie, B. Barbreau, A. Durand, B. Feuga and P. Peaudecerf, Modeling fracture flow with a stochastic discrete fracture network: Calibration and validation, 1, The flow model, Water Resour. Res., 26(3), pp. 479-489, 1990.

Decovalex (2000): Decovalex III, Bench Mark Test 2, Understanding the impact of Upscaling THM processes on Performance Assesment, alternatively known as THM Upscaling Bench Mark test, Test Case Description. 6.12.2000. Decovalex Secretariat (http://www.decovalex.com/).

Dershowitz 1998a, W, G. Lee, J. Geier, T. Foxford, P. LaPointe and A. Thomas, FracMan Interactive Discrete Feature Data Analysis, Geometric Modelling and Exploration Simulation, User Documentation, Golder Associates Inc., Seattle, Washington, 1998.

Dershowitz 1998b, W., G. Lee, Th. Eiben, and E. Ahlstrom, MeshMaster Discrete Fracture Mesh Generation Utility for use with FracMan User Documentation Version 1.550, Golder Associates Inc., 1998.

Dershowitz, W. S. and H. H., Herda, Interpretation of fracture spacing and intensity, Rock Mech., pp. 757-766, 1992.

Deutsch, C. V. and A. G. Journel, Geostatistical Software Library and User's Guide, Second edition, Oxford University Press, 1998.

Fisher, N., T. Lewis and B. Empleton, Statistics of Directional Data, Cambridge University Press, Cambridge, U. K., 1987.

Harrison J. P. and J. A. Hudson, Engineering Rock Mechanics: Part 2. Illustrative examples, Pergamon, Elsevier Science Ltd., The Boulevard, Longford Lane, Kidlington, Oxford OX5 1 GB, UK, 2000.

Hoek, E., Kaiser, P.K. & Bawden, W.F. 1995. Support of Underground Excavations in Hard Rock. A.A.Balkema, Rotterdam. Pp. 54-56.

Lee, G., W. Dershowitz, J. Geier, and E. Ahlstrom, EdMesh Discrete Fracture Mesh Editor User Documentation, Version 1.420, Golder Associates Inc., Redmond, Washington USA, Golder Associates Inc., 1999, February 17, 1999.

Long, J. C. S., J. S. Remer, C. R. Wilson and P. A. Witherspoon, Porous Media Equivalents for Networks of Discontinuous Fractures, Water Resour. Res., 18, pp. 645-658, 1982.

Miller, I., G. Lee and W. Dershowitz, MAFIC Matrix/Fracture Interaction Code With Heat and Solute Transport User Documentation, Version 1.6, Golder Associates Inc., Redmond, Washington, November 30, 1999.

Neuman, S. P., Stochastic continuum presentation of fractured rock permeability as an alternative to REV and fracture network concepts, in Proceedings of the 28th U.S. Symposium on Rock Mechanics, edited by I. W. Farmer, et al., pp. 533-561, A. A. Balkema, Brookfield, Vt., 1987.

Niemi, A., K. Kontio, and A. Kuusela-Lahtinen, Hydraulic characteri-zation and upscaling of fracture networks based on multiple-scale well test data, Water Resour. Res., 36(12), pp. 3481-3497, 2000.

Nirex. 1997a. The lithological and discontinuity characteristics of the Borrowdale Volcanic Group at outcrop in the Craghouse Park and Latterbarrow areas, Nirex Report SA/97/029.

Nirex 1997b. Evaluation of heterogeneity and scaling of fractures in the Borrowdale Volcanic group n the Sellafield area. Nirex Report SA/97/028.

Nirex. 1997c. Data summary sheets in support of gross geotechnical predictions. Nirex Report SA/97/052.

Nirex 1997d. An assessment of the post-closure performance of deep waste repository at Sellafield: Volume 1 – Hydrogeological model development – Conceptual basis and data, Nirex Report S/97/12.

Nirex 1997e. Assesment of the in-situ stress field at Sellafield., Nirex Report S/97/003.

Osnes, J. D., A. Winberg and J. Andersson, Analysis of Well Test Data – Application of Probabilistic Models to Infer Hydraulic Properties of Fractures, Topical Report RSI-0338, RE/SPEC Inc., Rapid City, South Dakota, 1988.

Öhman, J. and Niemi, A. 2003a. Upscaling of Fracture Hydraulics by Means of an Oriented Correlated Stochastic Continuum Model, Water Resourc. Res. (Accepted).

Pigott, A. R, Fractal relations for diameter and trace length of disc-shaped fractures. Journal of Geophysical Research, Vol. 102, No. B8, pages 18 121 - 18 125, 1997.

Pruess, K., C. Oldenburg and G. Moridis, TOUGH2 User's Guide, Version 2.0, Earth Science Division, Lawrence Berkeley National Laboratory University of California, Berkeley, California 94720, 1999.

HELSINKI UNIVERSITY OF TECHNOLOGY
Rock Engineering
Juha Antikainen 2003-10-20

Decovalex III
BMT 2: The THM Upscaling Bench Mark Test
Modelling the mechanical response of rock on repository excavation, filling and heating

1. Aims

The test case is described in Decovalex III Bench Mark Test "Test case description, Version 5, 15/11/2000" (Andersson & Knight 2000). The aim of thermo-mechanical modelling is to evaluate the changes in joint normal stress due to repository heating. The numerical results have been sent for further processing to Johan Öhman, University of Uppsala. Some calculated hydraulic aperture results are presented in this report just for demonstration the overall effect of heating.

2. Input data interpretation

A rock mechanical model is always a simplification of the reality. In this particular case, the major simplifications made in mechanical modelling are:
- 2D-modelling of 3D- reality (joint directions, infinite length of the model)
- assumption of linear elasticity of intact rock
- simple rock joint models
- repository excavation and filling are not modelled in detail

These simplifications can be justified with our aim to understand the modelling process rather than model any specific real-world case in detail.

2.1 Boundary conditions

The 2D model is oriented in the direction of maximum horizontal stress. Thus, the minimum horizontal stress is perpendicular to the model. The in-situ stresses change with depth D (m):

$\Phi_{vertical}$ 0.02494D+0.26622 MPa
Φ_{Hmin} 0.019961D-0.31619 MPa
Φ_{Hmax} 0.03113D+1.88747 MPa

In the model, the displacements are prevented in normal direction of model outer boundaries and freely allowed in the direction of the boundaries. The top of the model is free. The model width is 1100 m and the height 700 m. The model size was reduced from the original 5 km x 1 km size to speed up the thermal modelling. The thermal boundaries are adiabatic (insulated) on the sides of model and fixed temperature at top and at bottom of the model. The surface and sea water temperature is 11°C and the adiabatic lapse rate is 6.2^{oC}/km.

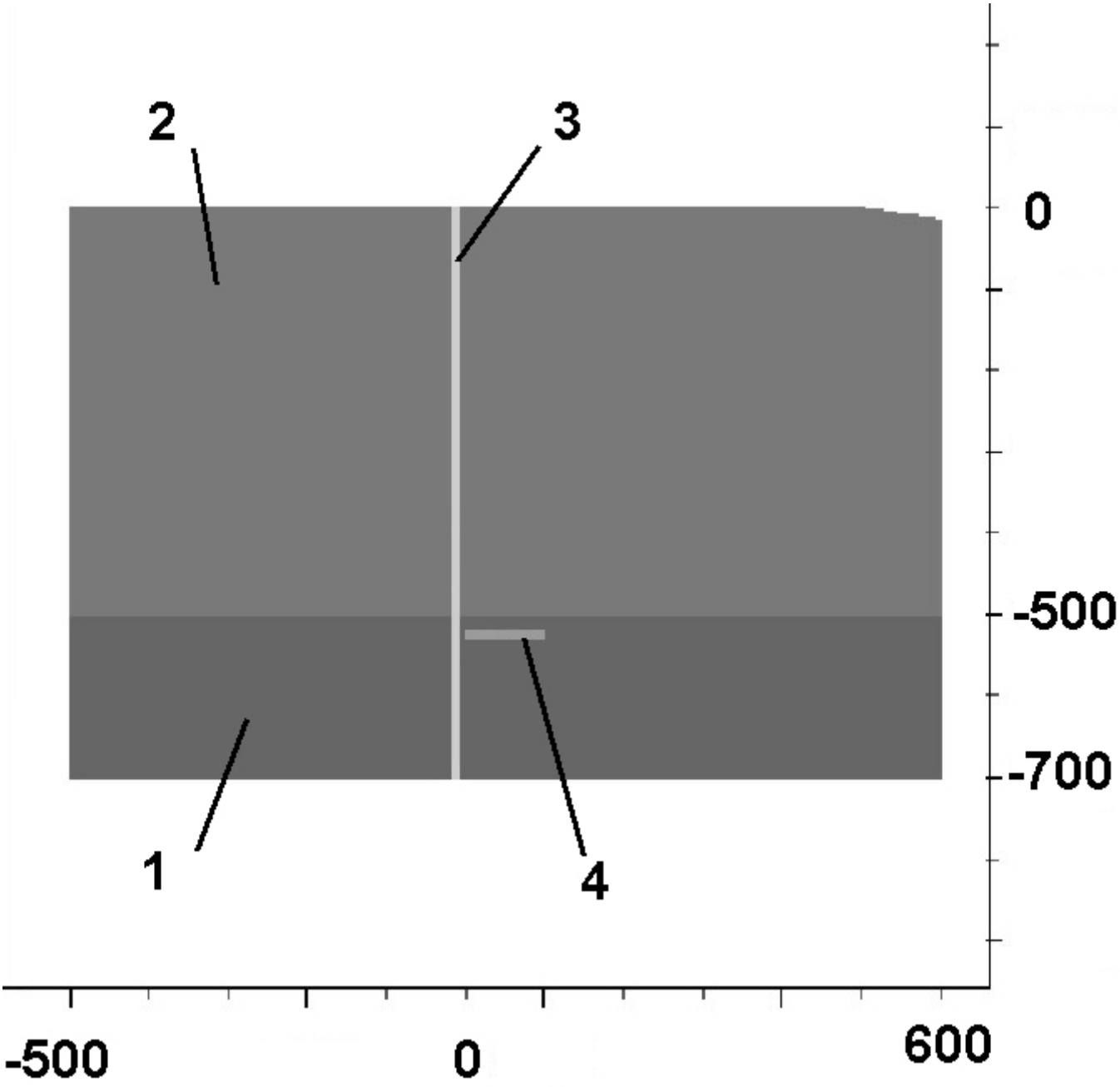

Figure 1. The size of the model is 1100 m by 700 m (Figure in scale).
Materials: 1 Bulk Longlands Farm Member
2 Altered Longlands Farm Member
3 Fault Zone (thickness 5 m)
4 Repository (100 m x 10 m)

2.2 Rock jointing

There are four fracture sets in the each rock types modelled. One of these sets is close the modelling plane and is therefore excluded from the modelling. The three other sets are not exactly perpendicular to the modelling plane, and 3D-2D -conversion is needed. Here the selected conversion method is to "rotate" the fracture set dip directions to the perpendicular position (Figure 2). So the dips of the fracture sets remain unchanged.

The mean joint spacing is used for modelling the rock structure. When a large number of joints and rock blocks are modelled, they are rather generated automatically than defined individually. The modelling code (UDEC) prefers convex-shaped distinct elements over the concave shapes, when the numerical stability of the solution is considered. Joints with infinitive length produce only convex shapes, and thus very long joints are the obvious starting point for model generation. Here infinitive joint length is assumed within each geological unit.

2.3 Intact rock properties

The intact rock properties (Table 1) were selected from provided data. The wireline data was used for Young's Modulus and Poisson's Ratio, because the core data was available only for Formation 1. The mean values for all three rock types were used for modelling.

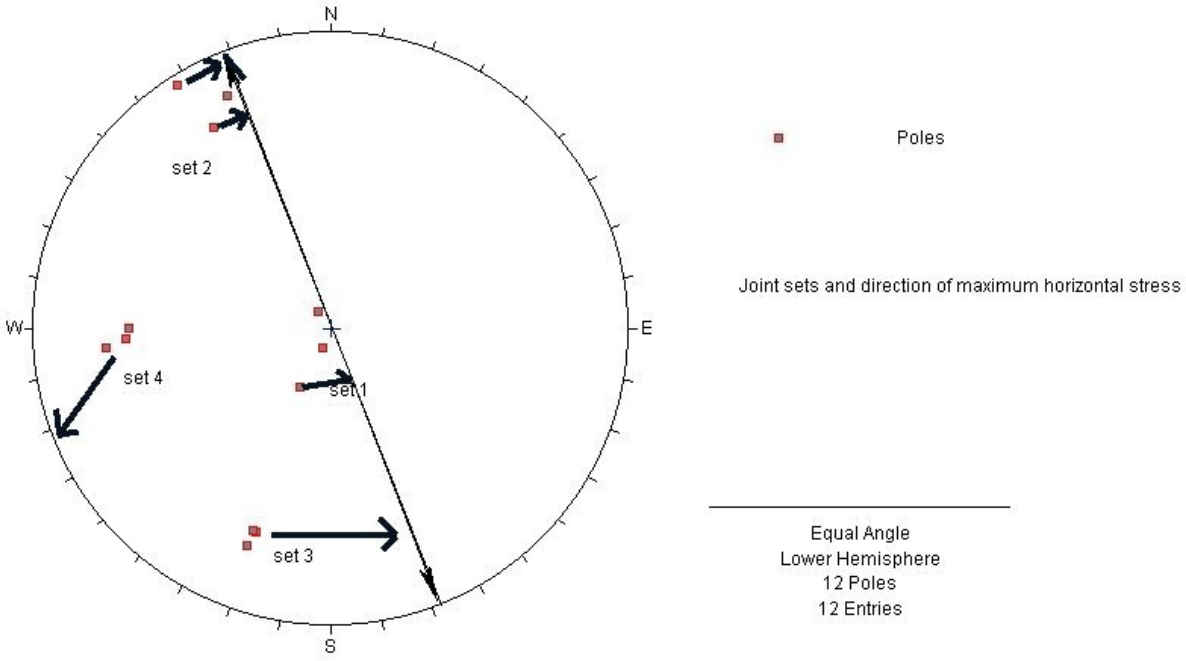

Figure 2. The modelling plane is directed parallel to the direction of the maximim horizontal stress. The fracture set 4 is almost parallel to the modelling plane, and can be excluded in modelling. The other sets are "rotated" to perpendicular direction to the modelling plane while keeping the dip unchanged.

Table 1. Intact rock properties

Material properties	Formation 1 Bulk Longlands	Formation 2 Altered Longlands	Fault Zone
UCS (MPa)	157.0	39.6	128.4
Young's Modulus (GPa)	69.08	46.93	62.62
Poisson's Ratio	0.263	0.287	0.262
Bulk modulus K (GPa)	48.58	36.72	43.85
Shear modulus G (GPa)	27.35	18.23	24.81
density (kg/m^3)	2750	2650	2730
thermal conductivity (W/mK)	2.29	2.29	2.29
specific heat capacity (J/kg/K)	798	798	798
thermal expansion coefficient	1×10^{-5}	1×10^{-5}	1×10^{-5}

2.4 Joint properties

The initial (non-scaled) joint properties (Table 2) were estimated with provided data. The mean values were used also here. The concept of instantaneous cohesion and friction (Hoek et.al. 1995) was used for values of joint cohesion and friction angles. These values were obtained as secant values between the minimum and maximum in-situ rock stress values on modelling plane at repository depth. Because it was not possible to model the vast number of joints in reality in the model, the joint normal and shear stiffness were scaled in modelling with the ratio between joint spacings (actual joint spacing / modelled joint spacing). The ratio used here was 1/50.

The hydraulic (conductive) apertures of the joints were calculated as a function of normal stress affecting across a joint. According the test data, the effect of shear displacement on the hydraulic apertures is very limited in the shear displacement range realised in the model. Thus the effect of joint shear displacement was omitted in calculation of the conductive apertures. The test data provided contained conductive aperture - normal stress curves for two samples. Only the apparently consistent parts of the curves were used. The maximum and minimum aperture curves were plotted (Fig. 3), and an approximation of normal stress - conductive aperture relationship was constructed (Eq. 1). The approximation fells well within the test results, and produces a positive aperture value for any compressive normal stress.

Table 2. Initial joint properties

Joint properties	Formation 1 Bulk Longlands	Formation 2 Altered Longlands	Fault Zone
Normal stiffness (GPa/m)	434	434	434
Shear stiffness (GPa/m)	434	434	434
Basic friction angle (E)	33.0	33.1	31.4
JRC_{300}	3.85	4.2	4.22
JCS_{300} (MPa)	112.21	55.3	103.81
Apparent cohesion (MPa)	0.69	0.74	0.74
Apparent friction angle (E)	34.6	33.5	33.0

$$e = \frac{27}{(\sigma_n + 1)^{0.66}} \qquad (Eq.\,1)$$

where:

e = *equivalent conductive aperture* (μm)

σ_n = *normal stress* (MPa)

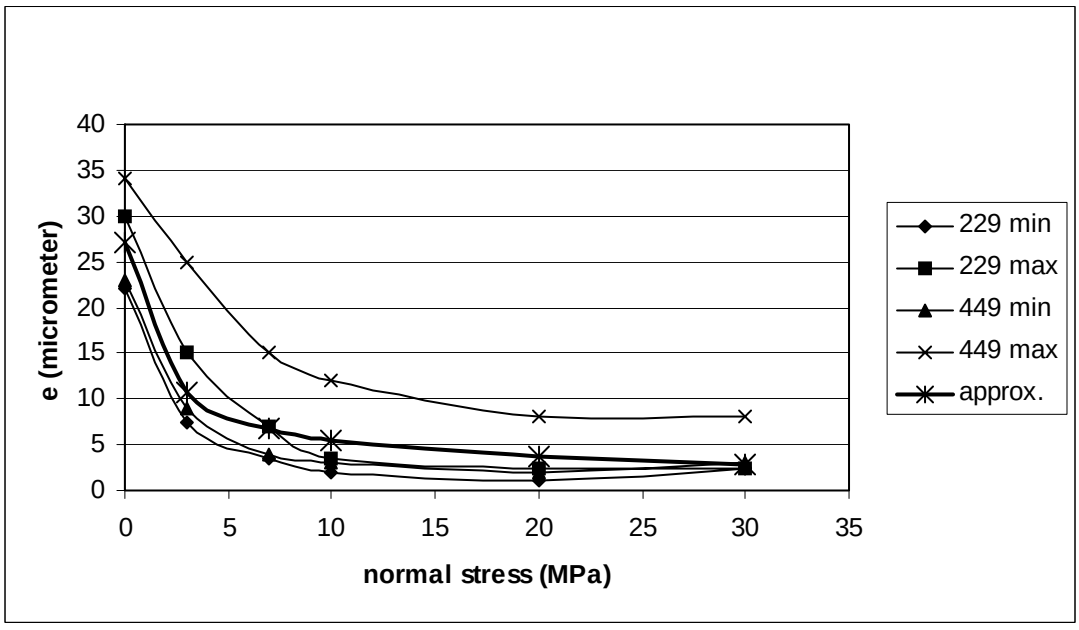

Figure 3. The normal stress - conductive aperture curves for samples 229 and 449 and the approximation used for aperture calculations.

3. Modelling

The model (Figure 1) consists of 5853 fully deformable, elastic 2D distinct element blocks and 21077 finite difference zones (elements). First the model was cycled to equilibrium state. Then the excavation of the repository was modelled by reducing the material stiffness and in-situ rock stress to 75% of the initial values in the repository area. The 75% value of remaining stiffness and rock stress is a rough estimate based on assumption that the repository excavations are parallel to the modelling plane and excavation ratio of 25%. The excavations are supposed to be designed to prevent any inelastic rock deformation. In this phase of modelling, the joint normal and shear displacement record is reset. This has no effect on the calculation of stresses.

The swelling pressure of bentonite was modelled by applying stepwise increasing pressure inside the entire repository area. The maximum applied swelling pressure was 2 MPa. Assuming 25% extraction ratio for the repository area, an 8 MPa actual swelling pressure inside the hypothetical excavations is required for same effect. The composition of the fill and the geometrical details of the repository was not defined and consequently not used in modelling. Anyway, the 8 MPa maximum pressure is much higher than the actual mixture used to fill any larger excavations inside the repository is likely to produce. The swelling pressure was modelled as a separate case, because the temporal development of swelling pressure was not defined.

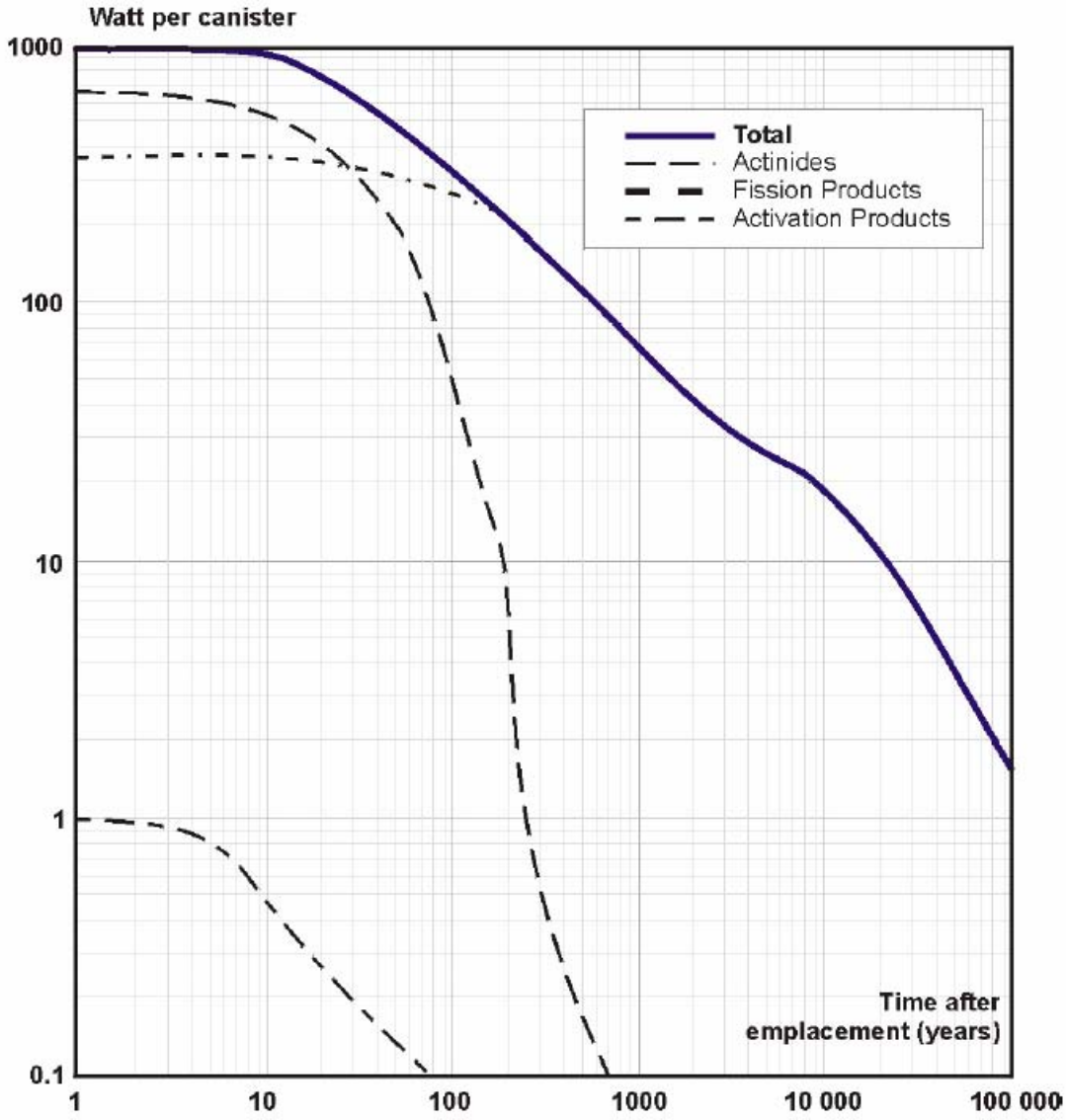

Figure 4. Heat evolution versus time for a single canister (extracted from BMT2 definition in Andersson & Knight 2000).

The thermal modelling was executed as a separate run of the distinct element model. The heating power of the waste is uniformly distributed across the entire repository area, resulting initial power value 0.6 W/m^3. For first three years time the power remains practically constant, and fixed power of 0.6 W/m^3 was used in the modelling. A decaying total heating power was determined for longer modelling times (Figure 4).

Because the fully coupled thermo-mechanical model has very short critical timestep length, the computation of long time periods needed here is very ineffective. Thus for time periods longer than 3 years one-directional coupling was applied. Because the rock stresses or displacements have virtually no effect on temperature distribution (in this case, at least), this simplification is justified. The temperature distribution was calculated first with simple, 2.1 km x 1.0 km size continuous model. Then the resulting temperature distribution was transferred into coupled distinct element model, and the resulting normal and shear stresses in the modelled joints was calculated.

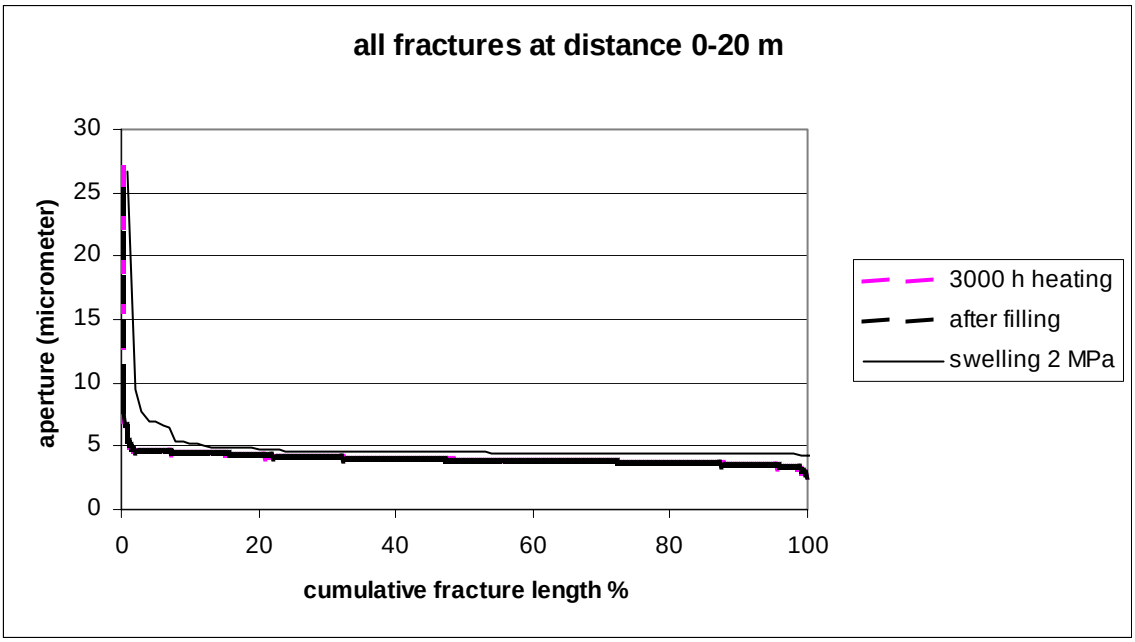

Figure 5. The apparent joint conductive apertures near the repository (fracture zone and fractures behind the fracture zone excluded) with two separate scenarios:
I: 2 MPa swelling pressure applied inside the repository
II: 0.6 W/m3 heating power applied 3000 hours. The effect of heating is very small.

4. Results

The modelling shows small, but clear coupling between the joint aperture and the swelling pressure in the proximity of the repository. The effect of heating is almost invisible, but still existent during the first months (Figure 5). At longer distances the swelling pressure or relatively short time heating has practically no effect on the joint apertures.

The applying of the decaying heat power source initially increases the rock mass temperature, and later the temperature decreases towards the original in-situ value. The temperature evolution varies at different locations (Figure 6). At and near the repository the temperature elevation is fast, and so is also the decaying (Figure 7). At locations further away the repository, temperature changes are smaller and rather uniform (Figures 8-10). The effect of long-term heating is clear at the vicinity of the repository, and the apparent fracture apertures are about 10-15% smaller after 100 years heating (Figure 11). The reason for the change is the increased normal stress across the fractures due to the thermal expansion of rock.

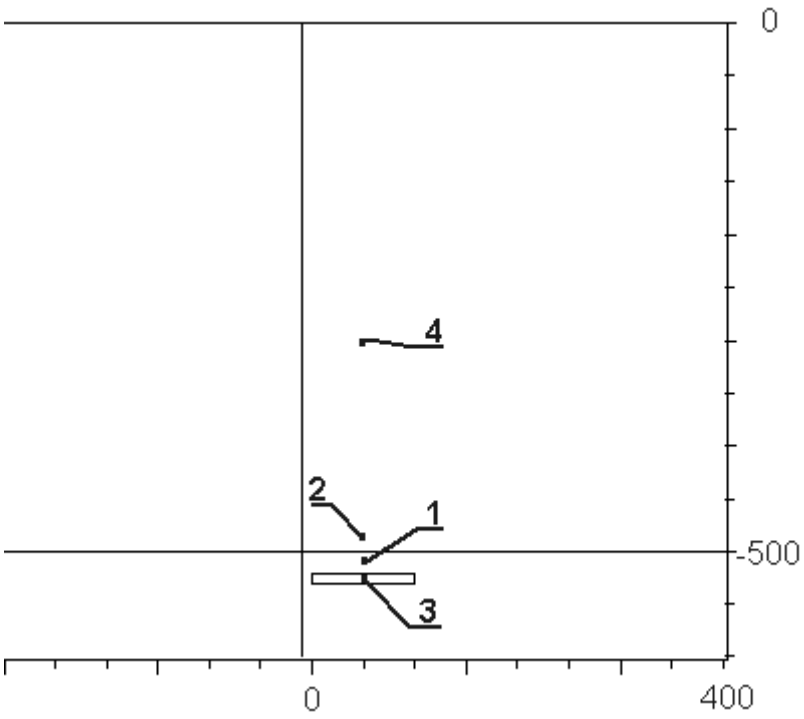

Figure 6. Temperature history locations.

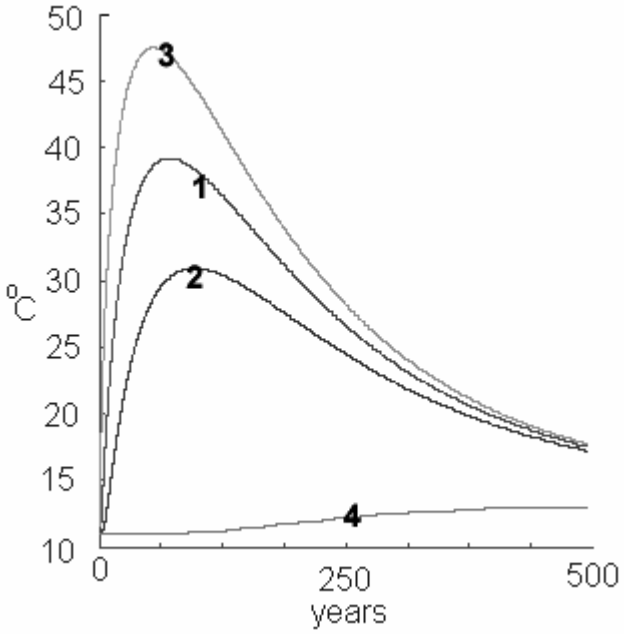

Figure 7. Temperature histories during first 500 year heating

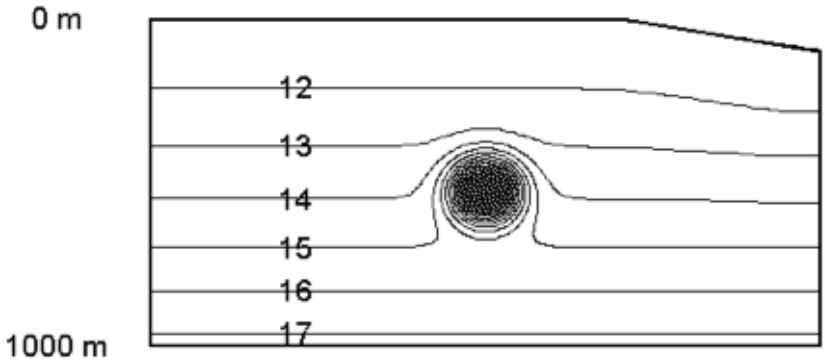

Figure 8. The thermal model. Temperature contours around the repository after 100 year heating (°C). Model width 2100 m.

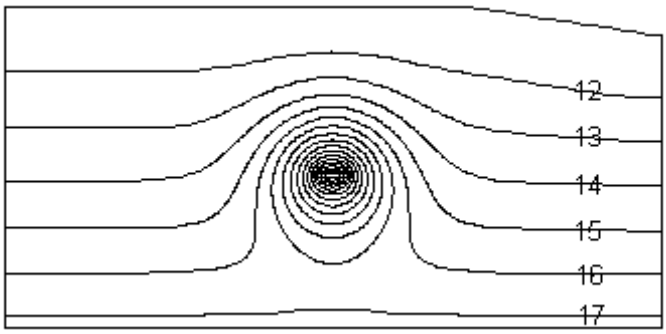

Figure 9. Temperature contours around the repository after 500 year heating (°C).

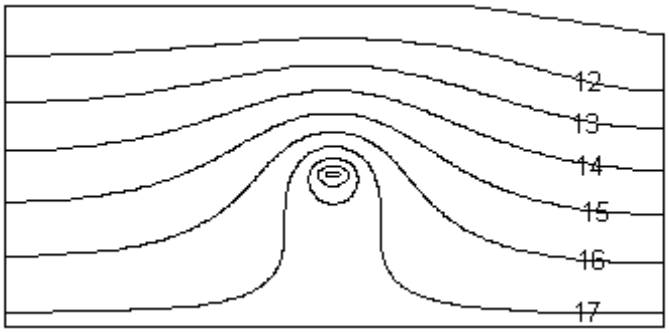

Figure 10. Temperature contours around the repository after 10'000 year heating (°C).

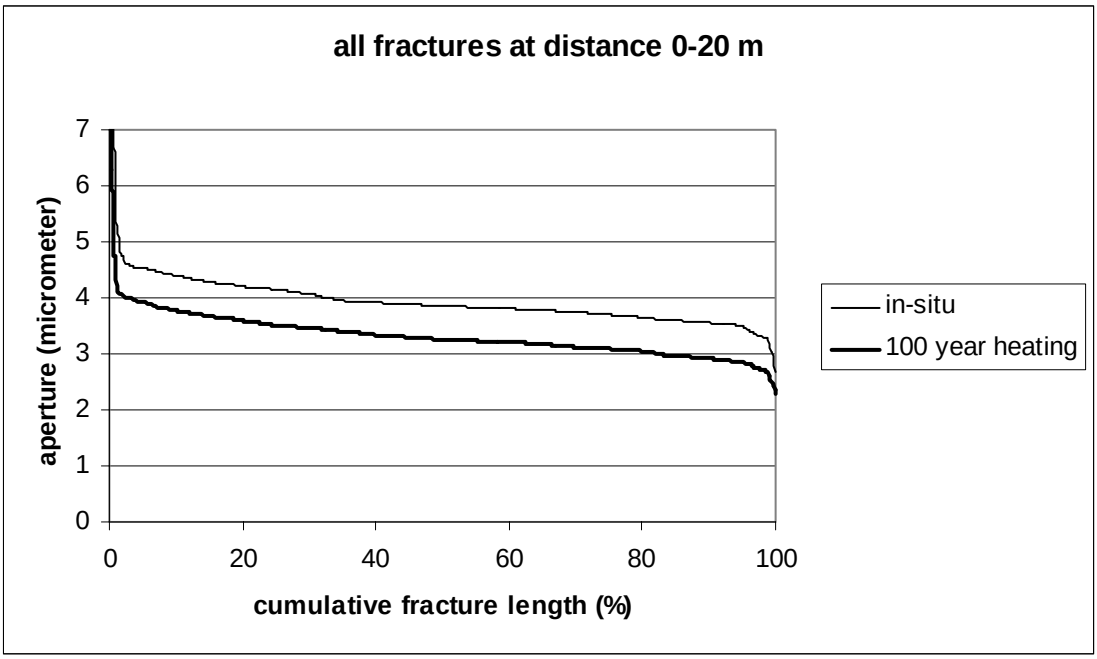

Figure 11. Effect of heating on fracture apertures within 20 m of repository.

References:

Andersson, J. and J. L. Knight 2000. The THM Upscaling Bench Mark Test 2 - Test Case Description.- Knight, J. L. (ed.), United Kingdom Nirex Limited, Harwell.

Hoek, E., Kaiser, P.K. & Bawden, W.F. 1995. Support of Underground Excavations in Hard Rock. A.A.Balkema, Rotterdam. Pp. 54-56.

Helsinki University of Technology
Laboratory of Structural mechanics

Teknillinen korkeakoulu
Rakenteiden mekaniikan laboratorio

Espoo 2004

PERMAFROST MODELLING IN DECOVALEX III FOR BMT3

Juha Hartikainen

This work is conducted by Dr Esko Eloranta on behalf of STUK, Radiation and Nuclear Safety Authority Finland

TEKNILLINEN KORKEAKOULU
TEKNISKA HÖGSKOLAN
HELSINKI UNIVERSITY OF TECHNOLOGY

1 Introduction

1.1 Background

This research has been undertaken as part of the Glaciation Bench Mark Test, the Bench Mark Test 3 (BMT3) of the international project DECOVALEX III (Chan et al., 2001). The BMT3 is a synthetic exercise constructed from geological and hydrogeological characteristics of a Northern Hemisphere site that is subjected to a prescribed time sequence of climatically driven environmental impacts upon its surface. A generic spent-fuel repository is assumed to be located in a hard rock mass, which consist of low-permeability, low-porosity competent rock matrix, traversed by fractures and a number of major fracture zones. The repository is further assumed to be located at sufficient high latitude that the hypothetical site can be assumed to have experienced past glaciation/deglaciation cycles and can be expected to undergo future glaciation within the future time frame (10000 - 100000 years).

1.2 Objectives

The work concerns with thermo-hydro-mechanical impacts of processes associated with perennial ground freezing and thawing in periods of glaciation/deglaciation on the long term performance of a hypothetical post-closure repository. The objectives of the work are:

1. to study by mathematical and numerical modelling the long-term evolution of a fractured rock mass in which a generic repository is located, as it undergoes a glaciation/deglaciation cycle in a time frame of 100000 years;
2. to assess the impact of the glaciation/deglaciation cycle on the coupled thermo-hydro-mechanical responses of the repository system and on its long-term performance in waste isolation;
3. to investigate/demonstrate the technical feasibility of deep geological disposal in hard rocks by exploring the possibility to further improve the scientific basis for safety assessment.

The focus of the work has been on understanding processes associated with permafrost development and perennial ground freezing and on studying their potential significance to Performance Assessment (PA).

1.3 Overview of key issues

A comprehensive review of issues associated with permafrost and related processes is given in the literature, e.g., Washburn 1979, Williams 1989 and French 1996. The relevant issues concerning this study are outlined in the following.

Henceforth permafrost is defined as ground in which temperature remains below zero-isotherm (0 °C) continuously for more than two years. Furthermore, perennial ground

freezing and perennial ground thawing signify permanent freezing of water in ground and permanent melting of ice in ground, respectively.

Nowadays permafrost occupies approximately 25 % of the Earth's continental land area (French, 1996) and the greatest reported depth of permafrost is in excess of 1400 m in Siberia (Washburn, 1979). Aggradation and degradation of permafrost as well as perennial freezing and thawing of ground is governed by a thermal regime in which the Earth's surface, lying beneath a cold atmosphere, is a heat sink, and the geothermal heat flux a heat source. If the mean annual zero-isotherm (freezing point) lies below the depth of seasonal temperature fluctuation, permafrost (perennially frozen ground) can exist. This provides, depending on the environmental factors as climate, topography, ground material, vegetation and snow cover, a mean air temperature about 1.5-9 °C colder than the temperature at the depth of seasonal fluctuation (Washburn, 1979).

Freezing of ground with sufficient water content can induce the frost phenomenon which is a complicated thermodynamic process involving gradual freezing of water at sub-zero temperatures, creation of cryogenic suction, driving of water from unfrozen ground to the freezing and frost heaving of frozen ground (Williams, 1989). The pressure and the stress fields generated by these processes are causes for consolidation of unfrozen ground and for weathering and degradation of frozen ground. Furthermore, it has been observed (Mahar et al, 1983; Hivon and Sego, 1995) that the salinity of water decreases considerable the freezing point and that the freezing process can cause redistribution of salinity concentration.

Permafrost as well as perennial ground freezing and thawing are integral parts of glaciation cycles. Evidence from continental deposits and oxygen-isotope ratios in marine sediments indicates that during the last 2.4 million years, much of the northern part of the Northern Hemisphere has been subject to repeated glacial cycles with a dominant period of about 100000 years and climate modelling (Burgess et al., 2000) suggests that despite an imminent phase of global warming due to the rapid increase of atmospheric greenhouse gases glacial cycles are likely to recur in the future. Past glacial periods were characterised by strong climatic variance including relatively intense cold periods during which permafrost rapidly expanded to cover large areas of the middle latitudes of the Northern Hemisphere, and large ice sheets grew and progressively overrode the permafrost, as far south as latitude 40° in North America and 52° in North-West Europe.

During a pre-glacial period a firm perennially frozen table is sustained under non-glacial conditions, whereas during a glacial stage it is difficult to maintain perennially frozen ground beneath an advancing glacier. The geothermal heat flux and the heat generated by friction at the glacier base are such that the glacially overridden perennially frozen ground becomes almost inevitably unstable, and decays progressively as the glacier advances over it. A wedge of perennially frozen ground is therefore expected to exist beneath the margin of an advancing ice sheet (Boulton et al., 1995) (see Figure 1.1). The perennially frozen ground and the glacier as well as the coupling between them are assumed to have the following features and consequences:

- The glacier sole and decaying perennially frozen ground are ground water sources, and water is driven outwards beneath the glacier by the glacier pressure gradient.

- The marginal wedge of perennially frozen ground is a zone of reduced hydraulic conductivity so that the outward ground water flux is forced to flow through a more restricted section.
- These circumstances tend to generate higher groundwater flow velocities and larger heads and head gradients than in a non-glacial perennially frozen zone.
- The rapid growth and decay of perennially frozen ground has the potential to create large transient overpressures or suction pressures as a consequence of the ice/water phase change.
- The high subglacial pressures, by lowering the melting point, cool down the subglacial bed so a rather thick subglacial permafrost zone can be sustained during the glacial stage.

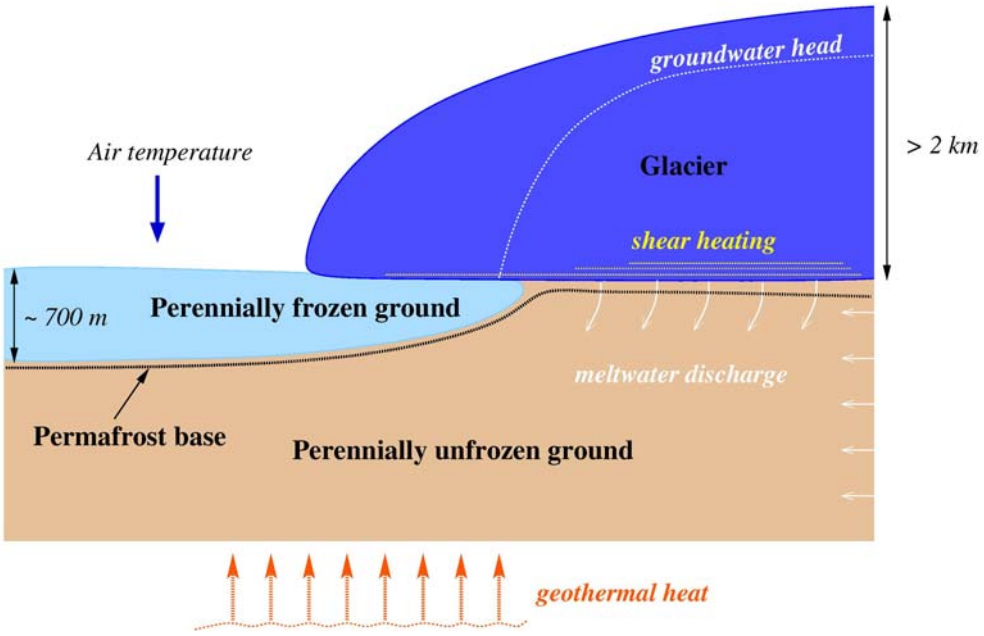

Figure 1.1: Geometry of system of glacier and perennially frozen/unfrozen ground.

2 Work definition and description

2.1 Overall project strategy

The work was undertaken into three phases. In Phase I the 2-D model for soil freezing (Mikkola and Hartikainen, 2001) was applied to some preliminary studies on coupled thermo-hydro-mechanical processes pertaining to permafrost development under non-glacial conditions. The Louvain-la-Neuve two-dimensional Northern Hemisphere climate model (LLN 2-D NH) (Loutre and Berger, 2000) was used to predict the temperatures for the next glacial cycle (Loutre, 2001). In Phase II the model was developed further to study effects of ground water salinity on the development of permafrost and perennially frozen ground. 1-D simulations with some sensitivity analysis on the thermal boundary conditions were carried out under both non-glacial and glacial conditions using the temperature data predicted by the ice sheet/drainage (Boulton and Payne, 1994) as uncoupled from the permafrost model. In Phase III 2-D simulations were performed in such a way that the permafrost and ice sheet/drainage models were weakly coupled together through the ice/bed interface. The ice sheet/drainage model (Boulton and Payne, 1994) was used to predict two temperature scenarios for the past glacial cycle as well as the evolution of ice sheet thickness and excess heat production generated by friction for the last glacial stage.

As described in the previous chapter, the pre-glacial and the glacial conditions are rather complex. Not only is the subsurface domain a coupled system but also the processes on the surface are coupled and transient. Further the lengthy time scale and the problems associated with modelling an entire glacial cycle necessitate a focus on the “worst cases” of loading. The worst cases of loading in a T-H-M perspective are presumed to arise along positions with deep permafrost and large gradients. Such a locality is believed to occur at final stage of pre-glacial period and at early stage of glaciation close to the ice sheet margin.

2.2 Geometry and material properties

The conceptual models have been constructed from a simplification of the geological, hydrological and rock mechanical characteristics of the Whiteshell Research Area (WRA) near the western edge of the Canadian Shield in eastern Manitoba (Chan et al., 2001). The model domain encompasses a volume approximately 25 km x 37 km x 4 km deep and consists of sparsely fractured rock, moderately fractured rock and highly fractured rock, which includes fracture zones. The rock is assumed to be completely saturated. Figure 2.1 shows a simplified map of the WRA, as well as the plan view of the conceptual model boundaries and the hypothetical rectangular repository with dimensions 2 km x 2 km x 10 m which is located approximately 500 m below surface. In addition, the lines labelled AA’ (Section 1) and BB’ (Section 2) indicate the locations and orientations of the two vertical sections which have been taken for the purpose of permafrost modelling. Section 1 is orthogonal and Section 2 parallel to the ice flow direction.

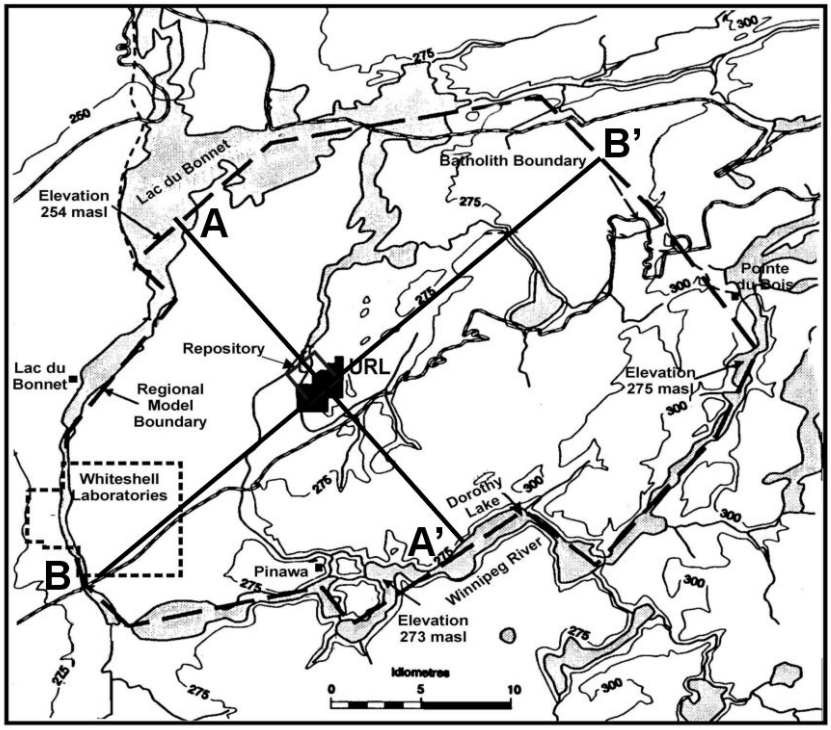

Figure 2.1: Simplified map of the Whiteshell Research Area (WRA).

2.2.1 Phase I modelling

For Phase I the vertical section (Section 1), as shown in Figure 2.2, has been taken for the purpose of 2-D permafrost modelling. A number of fracture zones/faults traverse the area. Three of the low- or intermediate-dip (LID) fracture zones are assumed to dip at 23° and one at 5.4° in the model. The vertical fracture zone is assumed to extend to the bottom of the model at about 4 km depth, whereas some of the LIDs are terminated at shallower depths. Detailed tables of the structural model are given in Aalto and Hartikainen (2004). All material properties are assumed to be homogeneous and given in Table 2.1.

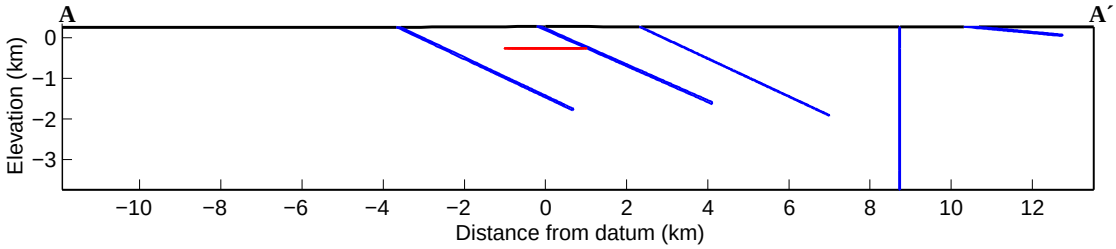

Figure 2.2: Vertical Section 1 (AA') of the proposed fracture zone geometry. The red line is the hypothetical repository location. The vertical and low dipping fracture zones are shown in blue.

Table 2.1: Material properties for Phase I.

Parameter	Rock mass	Fracture zone	Water	Ice	Units
Thermal conductivity, λ_α	3	2	0.56	2.24	$Wm^{-1}K^{-1}$
Specific heat capacity, c_α	750	900	4180	2100	$Jkg^{-1}K^{-1}$
Latent heat of fusion, ℓ			3.33×10^5		Jkg^{-1}
Bulk density, $\bar{\rho}_{\alpha 0}$	2700	2700	1000	917	kgm^{-3}
Porosity, η	0.005	0.05			
Permeability, κ	1.5×10^{-18}	1.5×10^{-15}			m^2
Fluid viscosity, μ			1.47×10^{-3}		Pas
Parameter Λ	1.06×10^{-4}	1.06×10^{-4}			
Young's modulus, E_α	3.5×10^{10}	3.5×10^9		3.5×10^7	Pa
Poisson's ratio, ν_α	0.22	0.22		0.22	

2.2.2 Phase II and Phase III modelling

For Phase II the vertical segment trough the centre of repository, as the line labelled CC' in Figure 2.3, comprises the 1-D model domain with the simplification that rock mass substitutes for the repository and the horizontal fracture zone. For Phase III the structural model is based on the vertical section (Section 2) shown in Figure 2.3. The fracture zones, from which one is vertical, one is horizontal and one dip at 45°, have been idealized as planar features of uniform thickness (20 m). Detailed tables of the structural model are given in Aalto and Hartikainen (2004).

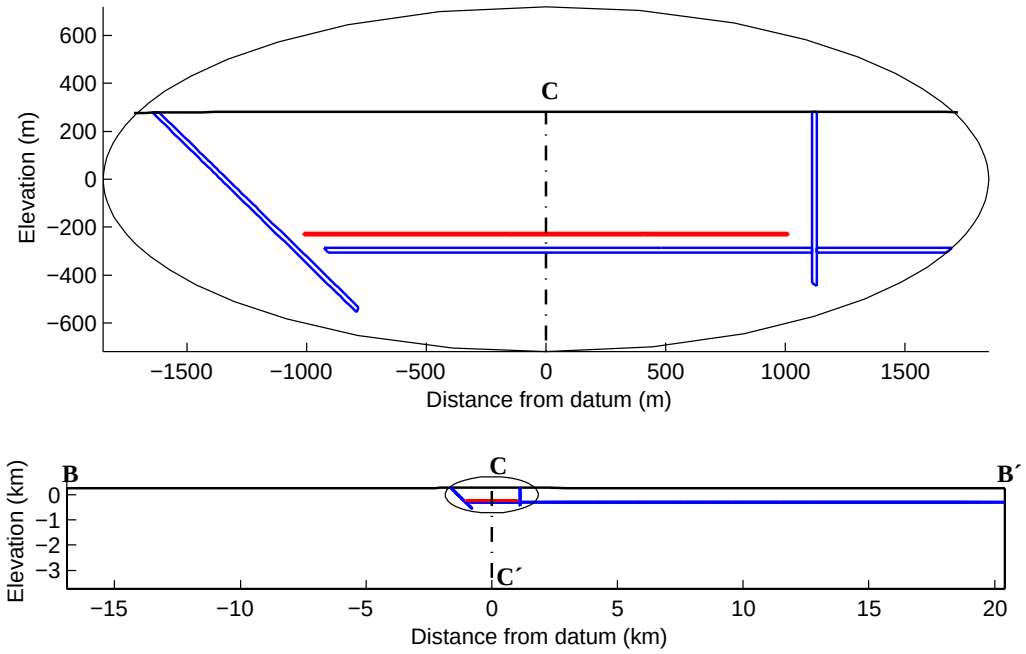

Figure 2.3: Vertical Section 2 of the proposed fracture zone geometry. The vertical and low dipping fracture zones are shown in blue and the repository in red.

The rock mass and the vertical fracture zones are each divided into 14 layers with permeability and porosity decreasing with depth as summarized in Table 2.2 and with homogenous thermal, mechanical, and complementary hydraulic properties as given in Table 2.3. The mechanical properties of the repository are assumed to be those of fracture zones and the elastic response of ice has been omitted, i.e. ice is assumed to have zero Young's modulus.

Table 2.2: Hydraulic properties for Phases II and III.

Rock mass outside fracture zones	Approximate depth (m)	Horizontal permeability (m^2)	Vertical permeability (m^2)	Porosity
Layer 1	1-100	1.0E-15	1.0E-14	0.003
Layer 2	100-200	4.5E-17	4.5E-16	0.003
Layer 3	200-300	6.0E-18	6.0E-17	0.003
Layer 4	300-400	7.75E-19	7.75E-19	0.003
Layer 5	400-500	3.15E-19	3.15E-19	0.003
Layer 6	500-750	3.35E-20	3.35E-20	0.003
Layer 7	750-1000	1.36E-21	1.36E-21	0.003
Layer 8	1000-1250	1.00E-21	1.00E-21	0.003
Layer 9	1250-1600	1.00E-21	1.00E-21	0.003
Layer 10	1600-2000	1.00E-21	1.00E-21	0.003
Layer 11	2000-2500	1.00E-21	1.00E-21	0.003
Layer 12	2500-3200	1.00E-21	1.00E-21	0.002
Layer 13	3200-4000	1.00E-21	1.00E-21	0.001
Vertical fracture zones	Approximate depth (m)	Longitudinal permeability (m^2)	Transverse permeability (m^2)	Porosity
Layer 1	0-100	1.00E-13	1.00E-13	0.05
Layer 2	100-200	1.00E-13	1.00E-13	0.05
Layer 4	200-300	1.00E-13	1.00E-13	0.05
Layer 5	300-400	1.00E-13	1.00E-13	0.05
Layer 5	400-500	1.00E-14	1.00E-14	0.05
Layer 6	500-750	1.00E-15	1.00E-15	0.05
Layer 7	750-1000	1.00E-16	1.00E-16	0.05
Layer 8	1000-1250	1.56E-17	1.56E-17	0.046
Layer 9	1250-1600	8.44E-18	8.45E-18	0.041
Layer 10	1600-2000	4.61E-18	4.61E-18	0.035
Layer 11	2000-2500	2.58E-18	2.58E-18	0.028
Layer 12	2500-3200	1.37E-18	1.37E-18	0.018
Layer 13	3200-4000	7.52E-19	7.52E-19	0.005
Low dipping fracture zones		Longitudinal permeability (m^2)	Transverse permeability (m^2)	Porosity
All layers		1.00E-13	1.00E-13	0.05
		Horizontal permeability (m^2)	Vertical permeability (m^2)	Porosity
Repository		5.63E-17	5.63E-17	0.0085

Table 2.3: Thermal, mechanical and complementary hydraulic properties for Phases II and III.

Parameter	Rock mass (s)	Fracture zone (s)	Units
Thermal conductivity, λ_α	3	3	$Wm^{-1}K^{-1}$
Specific heat capacity, c_α	750	750	$Jkg^{-1}K^{-1}$
Bulk density, $\bar{\rho}_{\alpha 0}$	2650	2650	kgm^{-3}
Intrinsic bulk modulus, $\overline{K}_\alpha$	2.22×10^{10}	2.22×10^{10}	Pa
Parameter Λ	1.06×10^{-4}	1.06×10^{-4}	
Young's modulus, E_α	3.5×10^{10}	3.5×10^{9}	Pa
Poisson's ratio, ν_α	0.22	0.22	
Cohesion, c'	5×10^{6}	3×10^{6}	Pa
Friction angle, ϕ	30	25	°
Tensile strength	5×10^{6}	0	Pa

Parameter	Water (w)	Salt NaCl (c)	Ice (i)	Units
Thermal conductivity, λ_α	0.56	2	2.24	$Wm^{-1}K^{-1}$
Specific heat capacity, c_α	4180	855	2100	$Jkg^{-1}K^{-1}$
Latent heat of fusion, ℓ	3.33×10^{5}			Jkg^{-1}
Molecular weight M_α	0.018	0.0585	0.018	$kgmol^{-1}$
Bulk density, $\bar{\rho}_{\alpha 0}$	1000	1622	917	kgm^{-3}
Intrinsic bulk modulus, $\overline{K}_\alpha$	2.22×10^{9}	2.22×10^{9}	2.22×10^{9}	Pa
Fluid viscosity, μ	1.47×10^{-3}			Pas

2.3 Initial state

Ambient in situ stresses in (MPa) are assumed to be as a function of depth described by the following relationships:

$$\sigma^0_{\text{Hmax}} = \begin{cases} 9.2 + 0.0470\Delta z & \text{if } 0 \le \Delta z \le 900 \\ 36.0 + 0.0172\Delta z & \text{if } 900 \le \Delta z \le 4000 \end{cases} \quad (2.1)$$

$$\sigma^0_{\text{Hmin}} = \begin{cases} 4.4 + 0.0266\Delta z & \text{if } 0 \le \Delta z \le 900 \\ 17.5 + 0.0120\Delta z & \text{if } 900 \le \Delta z \le 4000 \end{cases} \quad (2.2)$$

$$\sigma^0_{\text{V}} = 0.0260\Delta z \qquad \text{if } 0 \le \Delta z \le 4000\,, \quad (2.3)$$

where σ^0_{Hmax} is the horizontal in situ stress used for Phase III, σ^0_{Hmin} is the horizontal in situ stress used for Phase I, σ^0_{V} is the vertical in situ stress and Δz in (m) is the depth below ground surface.

The ambient in situ concentration of saline groundwater C^0 in (gl^{-1}) is assumed to be a function of depth by the expression

$$C^0 = \begin{cases} 100\dfrac{\Delta z}{1000} & \text{if } 0 \le \Delta z \le 1000, \\ 100 & \text{if } 1000 < \Delta z \le 4000. \end{cases} \tag{2.4}$$

2.4 Climate and glacier forcing

2.4.1 Phase I modelling

The mean annual surface temperature that causes growth and decay of permafrost under non-glacial conditions for the next glacial cycle is shown in Figure 2.4. The surface temperature has been inferred from Loutre (2001) based on the Louvain-la-Neuve two-dimensional Northern Hemisphere climate model (LLN 2-D NH) (Loutre and Berger, 2000). Moreover, non-glacial conditions are assumed during the glacial cycle.

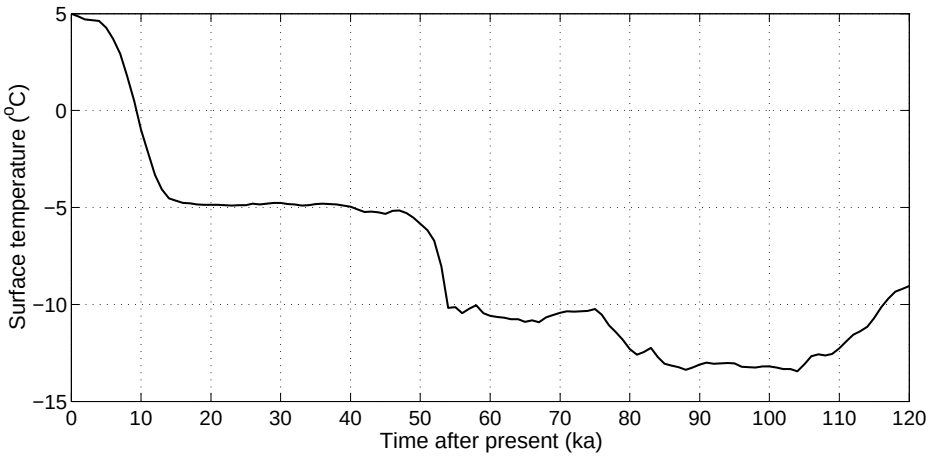

Figure 2.4: The mean annual surface temperature for Phase I.

2.4.2 Phase II modelling

The temperature data predicted by the ice-sheet/drainage model (Boulton and Payne, 1994) is applied to reconstruct the evolution of ground surface temperature, ice sheet thickness and groundwater head trough the last glacial cycle. The predicted temperatures T_{M} in (°C), which represent the basal temperatures during the glacial stages around 9300-25300, 55300-65900 and 84100-85500 years before present and the mean annual air temperatures during the non-glacial periods, are used to define the surface temperature scenarios, as shown in Figure 2.5, by the following relationship:

$$T_{\mathrm{S}} = \alpha T_{\mathrm{M}} + b\,, \tag{2.5}$$

where T_{S} in (°C) is the ground surface temperature. The parameters α and b corresponding to a low level and a high level surface cover are given in Table 2.4.

The evolution of ice sheet thickness, H, and ground water head, h_{G}, as shown in Figure 2.6, are reconstructed as a function of the pressure melting point T_m in (K) by the expressions

$$H = \frac{\ell}{\overline{\rho}_{i0} g}\left(\frac{1}{\overline{\rho}_{w0}} - \frac{1}{\overline{\rho}_{i0}}\right)^{-1} \frac{T_m - T_0}{T_0}, \qquad h_{\mathrm{G}} = \frac{\ell}{\overline{\rho}_{w0} g}\left(\frac{1}{\overline{\rho}_{w0}} - \frac{1}{\overline{\rho}_{i0}}\right)^{-1} \frac{T_m - T_0}{T_0}. \tag{2.6}$$

The pressure melting point is approximated as $T_m = \Delta\tilde{T}_{\mathrm{M}} + T_0$, where $\Delta\tilde{T}_{\mathrm{M}}$ in (K) is the smoothed basal temperature (see Figure 2.5).

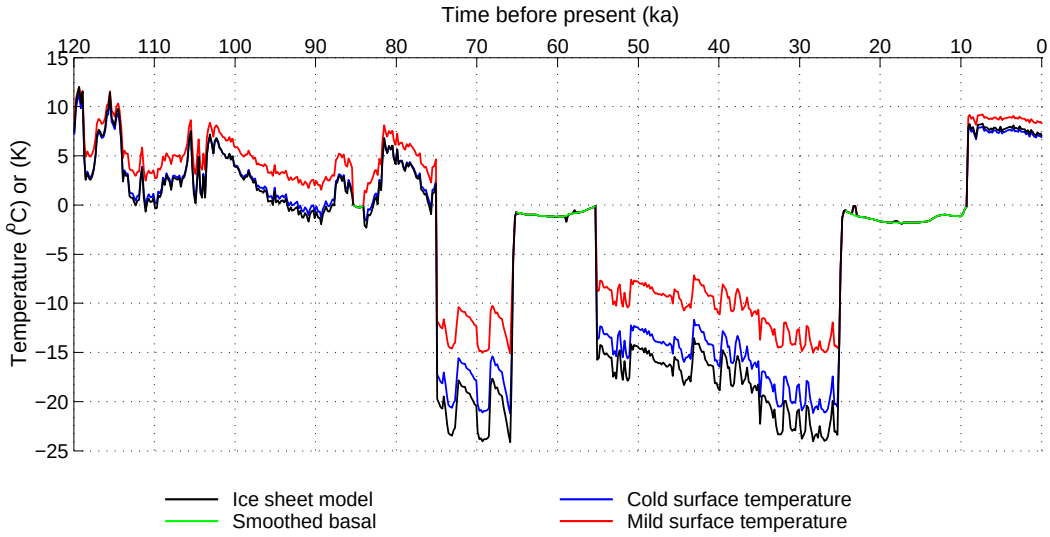

Figure 2.5: Temperatures predicted by the ice sheet/drainage model, reconstructed mean annual surface temperatures and smoothed basal temperatures for Phase II.

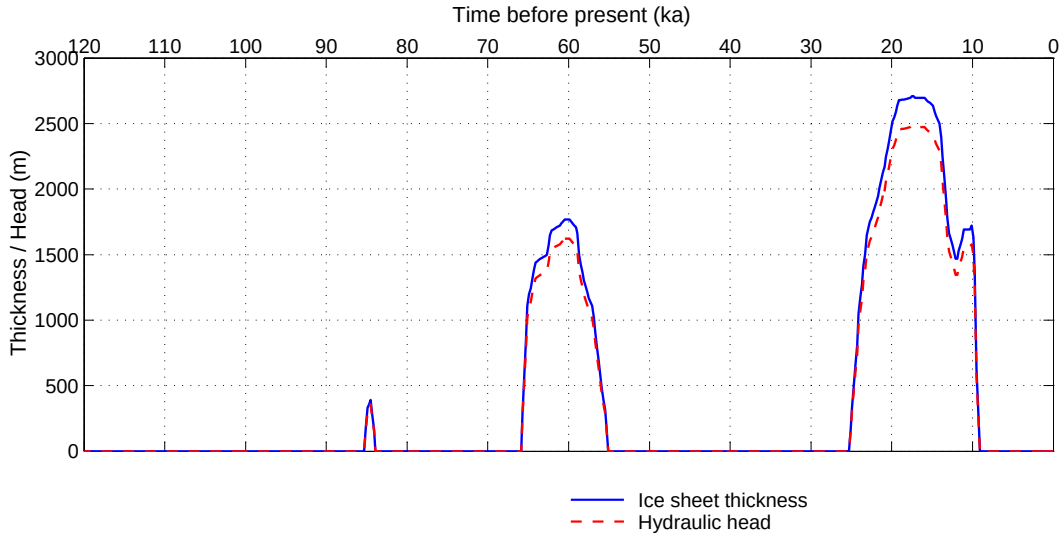

Figure 2.6: Reconstructed evolution of ice sheet thickness and groundwater head for Phase II.

Table 2.4: Surface temperature parameters for Phase II.

Parameter	Cold surface temperature		Mild surface temperature	
	Glacial	Non-glacial	Glacial	Non-glacial
α	1.0	0.9	1.0	0.75
b (°C)	0.0	0.5	0.0	3.0

2.4.3 Phase III modelling

Climate and glacier forcing are based on the ice-sheet/drainage model (Boulton and Payne, 1994). The temperature scenarios, Figure 2.7, are applied to the surface under non-glacial conditions, whereas the mechanical ice load and the excess heat production at the ice-bed interface, Figures 2.8 and 2.9, together with the ground water flux through the up-glacier side boundary, Figure 2.10, are introduced under glacial conditions during the last glacial stage around 10800-24000 years before present. During glaciation the advancing ice sheet is assumed to cross the right hand margin at 23856 years, the zero-datum at 23000 years and the left hand margin at 22291 years before present and to reach the maximum thickness of ~2970-3130 m along the transect at about 14500 years before present. During deglaciation the retreating ice sheet is assumed to pass the left hand margin at 11085 years the zero-datum at 11000 years and the right hand margin at 10860 years before present.

The surface temperatures are described using the relation (2.5) with the parameters associated with Cold surface temperature in Table 2.4. The basal melt rate at the ice/bed interface is defined trough the balance laws of mass and energy as part of the permafrost problem.

It should be mentioned that glacial conditions are considered only during the last glacial period.

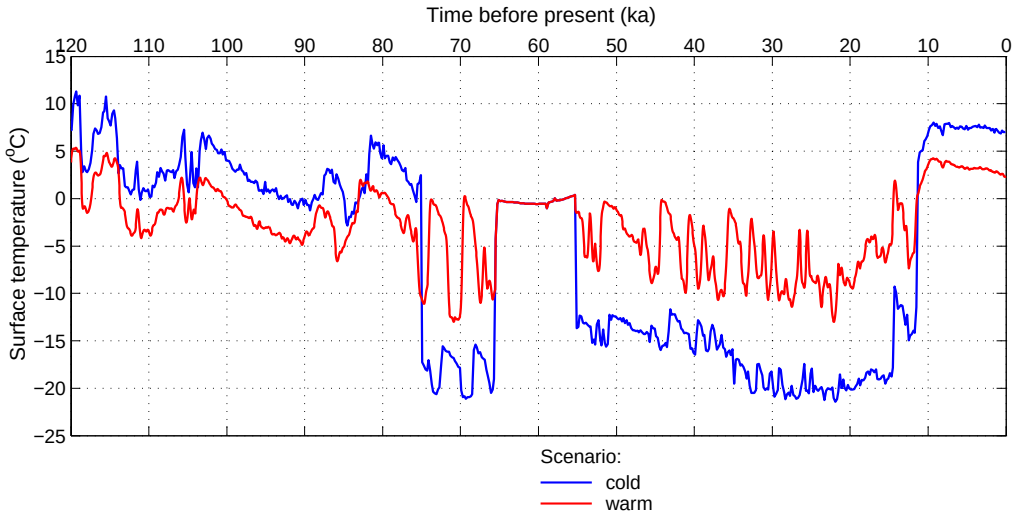

Figure 2.7: Evolution of the mean annual surface temperatures for Phase III.

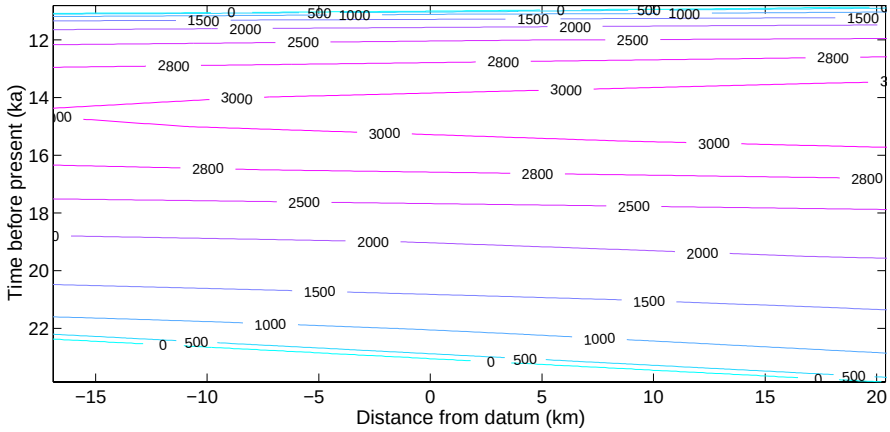

Figure 2.8: Evolution of ice sheet thickness (m) in time along the site for Phase III.

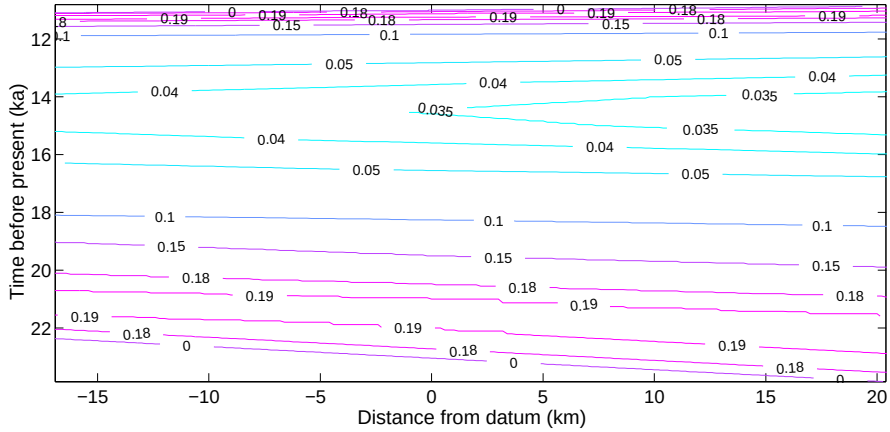

Figure 2.9: Evolution of excess heat production (Wm^{-2}) in time along the site for Phase III.

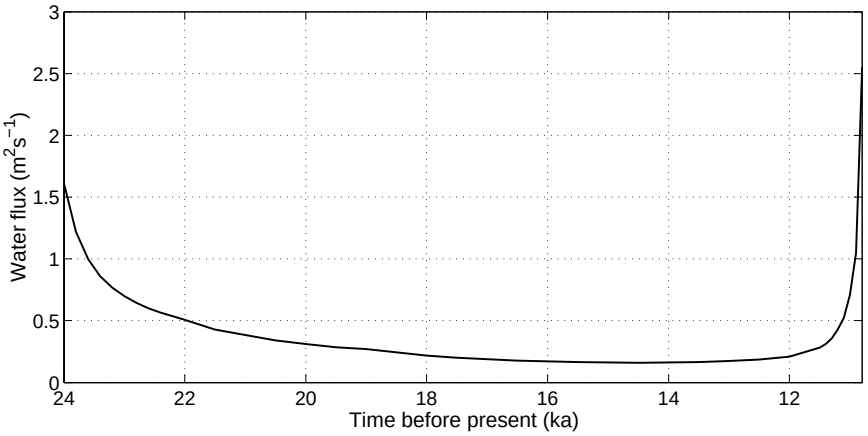

Figure 2.10: Evolution of the ground water flux across the up-glacier boundary for Phase III.

2.5 Geothermal heat

Geothermal heat flow at the base of the model domain (at the depth of about 4 km) is based on Kukkonen (1989). It is assumed to be 0.04 Wm^{-2} for Phases I and III and to vary between 0.04 Wm^{-2} and 0.06 Wm^{-2} for Phase II.

2.6 Heat production of nuclear fuel waste

Heat production of nuclear fuel waste r in (Wm^{-3}) is assumed to be uniform within the repository and estimated as a function of time based on Raiko (1996) by the following relationship (see Figure 2.11):

$$r = \begin{cases} 0.7\dfrac{\Delta t}{30} & \text{if } 0 \le \Delta t \le 30, \\ 0.7\left(\dfrac{10^6}{\Delta t} - 0.6\right)^{0.73}\left(\dfrac{10^6}{30} - 0.6\right)^{-0.73} & \text{if } \Delta t > 30, \end{cases} \tag{2.7}$$

where Δt in (a) is time after the onset of reposition, which is assumed to be at the present day for Phase I and at 82000 years before present for Phase III. For Phase II no heat production is considered.

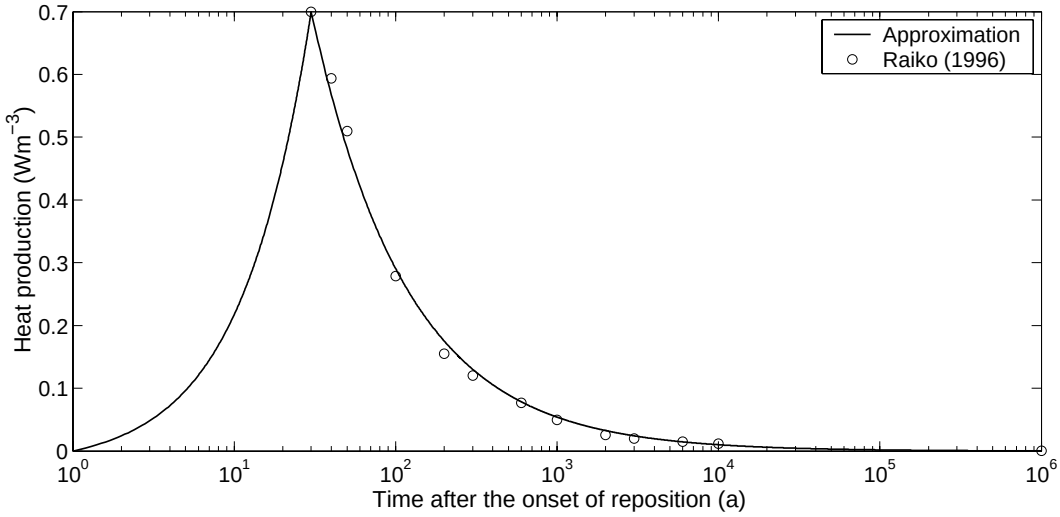

Figure 2.11: Evolution of nuclear fuel waste heat production for Phases I and III.

3 Mathematical model

3.1 General approach

3.1.1 Introduction

The mathematical model for freezing and thawing of saline water saturated ground is based on the approach described in Hartikainen and Mikkola (2003). The bases are the theory of mixture with the concept of molar volume fractions, the conservation laws and the constitutive relations derived through the specific free energy functions and the dissipation potential by making use of the entropy inequality. The thermo-hydro-chemo-mechanically coupled model is capable of describing the relevant features of the frost phenomenon and the implications of pore water salinity as described in Chapter 1.

3.1.2 Basic concepts and notation

The ground is considered as porous medium of rock skeleton (s), filled up with pore fluid (f) and ice (i), such that the phases $\kappa \in \{s, f, i\}$ are found in the volume fractions $\beta^\kappa = \mathrm{d}v^\kappa / (\mathrm{d}v^s + \mathrm{d}v^f + \mathrm{d}v^i)$, where $\mathrm{d}v^\kappa$ is the volume element of $\kappa \in \{s, f, i\}$. Moreover, pore fluid is assumed to be composed of water (w) and dissolved salts (c) by means of the molar fractions $\zeta_\lambda = n_\lambda / (n_w + n_c)$, where n_λ is the mole number of substance $\lambda \in \{w, c\}$. Hence, we have a mixture of constituents $\alpha \in \{s, w, c, i\}$, which coexist in the molar volume fractions

$$\xi_s = \beta^s, \quad \xi_w = \zeta_w \beta^f, \quad \xi_c = \zeta_c \beta^f, \quad \xi_i = \beta^i. \tag{3.1}$$

The molar fractions satisfy the evident conditions

$$\xi_s + \xi_w + \xi_c + \xi_i = 1, \quad \xi_\alpha \geq 0, \quad \alpha \in \{s, w, c, i\}. \tag{3.2}$$

The constituent intrinsic or bulk densities denoted by $\overline{\rho}_\alpha$ define the apparent densities by the expression $\rho_\alpha = \xi_\alpha \overline{\rho}_\alpha$.

The constituent velocities are denoted by $\mathbf{v}_\alpha$. The Darcian flow $\mathbf{J}_{\beta^f} = \beta^f (\mathbf{V}^f - \mathbf{v}_s)$ and the Fickian flows $\mathbf{J}_{\zeta_\lambda} = \zeta_\lambda (\mathbf{v}_\lambda - \mathbf{V}^f), \lambda \in \{w, c\}$ are introduced with the fluid velocity $\mathbf{V}^f = \zeta_w \mathbf{v}_w + \zeta_c \mathbf{v}_c$ to define the molar volume flow of water and solutes as

$$\mathbf{J}_{\xi_\alpha} = \xi_\alpha (\mathbf{v}_\alpha - \mathbf{v}_s) = \zeta_\lambda \mathbf{J}_{\beta^f} + \beta^f \mathbf{J}_{\zeta_\lambda}, \quad \alpha = \lambda, \quad \lambda \in \{w, c\}. \tag{3.3}$$

Note that obviously $\mathbf{J}_{\xi_s} = \mathbf{0}$, but also $\mathbf{J}_{\xi_i} = \mathbf{0}$, since it is assumed that skeleton and ice are equal in velocity.

The strain tensors of skeleton and ice dealing with small strains are given by

$$\boldsymbol{\varepsilon}_\alpha = \tfrac{1}{2}\left[\operatorname{grad}\mathbf{u}_\alpha + (\operatorname{grad}\mathbf{u}_\alpha)^{\mathrm{T}}\right], \quad \alpha \in \{s,i\}, \tag{3.4}$$

where $\mathbf{u}_\alpha$ is the displacement vector.

3.1.3 Balance laws

Since the evolution of ground freezing is slow, inertia forces, kinetic energy terms and the energy terms due to deformations can be considered to be negligibly small in the conservation of mass, momentum and energy. Hence, the balance of mass can be stated as

$$\begin{aligned} &\theta_s = 0, \qquad \theta_c = 0, \qquad \theta_w + \theta_i = 0, \\ &\theta_\alpha = \left(\xi_\alpha \overline{\rho}_\alpha\right)_s^{\bullet} + \xi_\alpha \overline{\rho}_\alpha \operatorname{div}\mathbf{v}_s + \operatorname{div}\left(\overline{\rho}_\alpha \mathbf{J}_{\xi_\alpha}\right), \quad \alpha \in \{s,w,c,i\}, \end{aligned} \tag{3.5}$$

where θ_α denotes the constituent rate of mass production and $\left(\bullet\right)_s^{\bullet} = \partial(\bullet)/\partial t + \operatorname{grad}(\bullet)\cdot\mathbf{v}_s$ symbolizes the material time derivative with respect to the motion of skeleton.

The balance of momentum is given by

$$\sum_{\alpha\in\{s,w,c,i\}} \left(\operatorname{div}\boldsymbol{\sigma}_\alpha + \xi_\alpha \overline{\rho}_\alpha \mathbf{g}\right) = \mathbf{0}, \tag{3.6}$$

where $\boldsymbol{\sigma}_\alpha$ is the constituent Cauchy stress tensor and $\mathbf{g}$ ($g = 9.81\,\mathrm{ms}^{-2}$) is the acceleration of gravity.

The balance of energy is formulated as

$$\sum_{\alpha\in\{s,w,c,i\}} \left(\xi_\alpha \overline{\rho}_\alpha \left(e_\alpha\right)_s^{\bullet} + \overline{\rho}_\alpha \operatorname{grad} e_\alpha \cdot \mathbf{J}_{\xi_\alpha} + e_\alpha \theta_\alpha + \operatorname{div}\mathbf{q}_\alpha - r_\alpha\right) = 0, \tag{3.7}$$

where e_α, $\mathbf{q}_\alpha$ and r_α are the constituent specific internal energy, heat flow vector and external heat supply, respectively.

3.1.4 Constitutive equations

It is assumed that skeleton and ice are elastic solids, pore fluid is an ideal solution of water and dissolved salts and governed by adsorption and that all constituents are intrinsically compressible. Furthermore, phase change between water and ice is assumed to be a reversible process and dissipation is generated by heat conduction, by pore fluid flow, with reduction in permeability due to ice segregation, and by diffusion of solutes. The constitutive relations are summarized as follows.

The constituent internal energies are the expressions

$$e_s = c_s T, \quad e_w = c_w\left(T - T_0\right) + \ell, \quad e_c = c_c T, \quad e_i = c_i\left(T - T_0\right), \tag{3.8}$$

where c_α is the constituent specific heat capacity, T is the absolute temperature and ℓ denotes the latent heat of fusion at $T_0 = 273.15\,\mathrm{K}$.

The constituent heat flow vectors are determined as the Fourier's law

$$\mathbf{q}_\alpha = -\xi_\alpha \lambda_\alpha \operatorname{grad} T, \quad \alpha \in \{s, w, c, i\}, \tag{3.9}$$

where λ_α is the constituent thermal conductivity.

The constituent stress tensors are decomposed as

$$\boldsymbol{\sigma}_s = \boldsymbol{\sigma}_s^{\mathrm{ef}} - p_s^{\mathrm{th}}\mathbf{I}, \quad \boldsymbol{\sigma}_w = -p_w^{\mathrm{th}}\mathbf{I}, \quad \boldsymbol{\sigma}_c = -p_c^{\mathrm{th}}\mathbf{I}, \quad \boldsymbol{\sigma}_i = \boldsymbol{\sigma}_i^{\mathrm{ef}} - p_i^{\mathrm{th}}\mathbf{I}, \tag{3.10}$$

where the constituent effective stress tensors $\boldsymbol{\sigma}_\alpha^{\mathrm{ef}}$ are given by

$$\boldsymbol{\sigma}_\alpha^{\mathrm{ef}} = \xi_\alpha \left[\frac{E_\alpha}{1+\nu_\alpha}\boldsymbol{\varepsilon}_\alpha + \frac{E_\alpha \nu_\alpha}{(1+\nu_\alpha)(1-2\nu_\alpha)} \operatorname{tr}\boldsymbol{\varepsilon}_\alpha \mathbf{I} \right], \quad \alpha \in \{s, i\} \tag{3.11}$$

and the constituent thermodynamic pressures p_α^{th} by

$$p_\alpha^{\mathrm{th}} = \xi_\alpha \left[(\xi_w + \xi_c)\overline{\rho}_w \frac{RT}{M_w} \frac{\partial f}{\partial \xi_\alpha} + \hat{B} \right], \quad \alpha \in \{s, w, c, i\}. \tag{3.12}$$

E_α is the constituent Young's modulus, ν_α is the constituent Poisson's ratio, $R = 8.3144\,\mathrm{JK^{-1}mol^{-1}}$ is the universal gas constant and M_w is the molecular weight of water. Furthermore, the function

$$f(\xi_s, \xi_w, \xi_c) = \begin{cases} \Lambda \left[\dfrac{\xi_w^0 + \xi_c^0}{\xi_s^0} \dfrac{\xi_s}{\xi_w + \xi_c} - 1 \right]^2 & \text{if } \dfrac{\xi_s}{\xi_w + \xi_c} \geq \dfrac{\xi_s^0}{\xi_w^0 + \xi_c^0}, \\ 0 & \text{if } \dfrac{\xi_s}{\xi_w + \xi_c} \leq \dfrac{\xi_s^0}{\xi_w^0 + \xi_c^0} \end{cases} \tag{3.13}$$

characterizes adsorption in the porous medium and the pressure component $\hat{B}$ represents the total pore pressure, since $p_s^{\mathrm{th}} + p_w^{\mathrm{th}} + p_c^{\mathrm{th}} + p_i^{\mathrm{th}} = \hat{B}$. Λ is material parameter and the superscript 0 refers to the initial state.

The compressibility of constituents is characterized through the bulk densities

$$\overline{\rho}_\alpha = \overline{\rho}_{\alpha 0} \exp\left(\frac{1}{\overline{K}_\alpha} \frac{p_\alpha^{\mathrm{th}}}{\xi_\alpha} \right), \quad \alpha \in \{s, w, c, i\}, \tag{3.14}$$

where $\overline{\rho}_{\alpha 0}$ denotes the reference constituent bulk density and $\overline{K}_\alpha$ is the intrinsic constituent bulk modulus.

Fluid flow in porous medium is described as the law of Darcian type

$$\mathbf{J}_{\beta^f} = -\frac{\boldsymbol{\kappa}}{\mu}\cdot\left[\operatorname{grad}\left(\frac{p_w^{\mathrm{th}}+p_c^{\mathrm{th}}}{\xi_w+\xi_c}\right)-\frac{\xi_w\overline{\rho}_w+\xi_c\overline{\rho}_c}{\xi_w+\xi_c}\mathbf{g}+\overline{\rho}_w\frac{RT}{M_w}\operatorname{grad} f\right], \tag{3.15}$$

where $\boldsymbol{\kappa}$ is the permeability tensor of porous medium and μ is the dynamic viscosity of pore fluid. Permeability is assumed to be a function of the unfrozen fluid content $\chi=(\xi_w+\xi_c)/(\xi_w+\xi_c+\xi_i)$ of the form

$$\boldsymbol{\kappa}=\boldsymbol{\kappa}_0\chi^5, \tag{3.16}$$

where the subscript 0 refers to the unfrozen state.

Transportation of solutes is defined as the law of Fickian type

$$\mathbf{J}_{\zeta_c} = -\mathbf{D}\cdot\left[\operatorname{grad}\left(\frac{\xi_c}{\xi_w+\xi_c}\right)-\frac{M_c-M_w}{RT}\frac{\xi_w\xi_c}{(\xi_w+\xi_c)^2}\mathbf{g}\right], \tag{3.17}$$

where $\mathbf{D}$ is the diffusion tensor and M_c is the molecular weight of solutes. Note further that $\mathbf{J}_{\zeta_w}=-\mathbf{J}_{\zeta_c}$.

Finally, the phase change is governed by the generalized Clausius-Clapeyron's equation

$$\begin{aligned}&-(c_w-c_i)\left[T\ln\left(\frac{T}{T_0}\right)-(T-T_0)\right]-\ell\frac{T-T_0}{T_0}+\left(\frac{p_w^{\mathrm{th}}}{\xi_w\overline{\rho}_w}-\frac{p_i^{\mathrm{th}}}{\xi_i\overline{\rho}_i}\right)+\\&+\frac{RT}{M_w}\ln\left(\frac{\xi_w}{\xi_w+\xi_c}\right)+\frac{RT}{M_w}f(\xi_s,\xi_w,\xi_c)=0.\end{aligned} \tag{3.18}$$

3.2 Permafrost model

The model is simplified further for the purpose of numerical simulations by excluding the transportation of solutes, i.e. $\mathbf{J}_{\zeta_c}=\mathbf{0}$. Hence, by use of (3.3) the balance equations (3.5)-(3.7) omitting the mass balance of solutes can be reformulated as follows:

$$(\xi_s)_s^{\bullet}+\xi_s\operatorname{div}\mathbf{v}_s+\frac{\xi_s}{\overline{K}_s}\left(\frac{p_s^{\mathrm{th}}}{\xi_s}\right)_s^{\bullet}=0, \tag{3.19}$$

$$\begin{aligned}&-\left(1-\frac{\overline{\rho}_i}{\overline{\rho}_w}\right)\left[(\xi_i)_s^{\bullet}+\xi_i\operatorname{div}\mathbf{v}_s\right]+\operatorname{div}\mathbf{v}_s+\frac{\xi_s}{\overline{K}_s}\left(\frac{p_s^{\mathrm{th}}}{\xi_s}\right)_s^{\bullet}+\frac{\xi_w}{\overline{K}_w}\left(\frac{p_w^{\mathrm{th}}}{\xi_w}\right)_s^{\bullet}+\frac{\xi_c}{\overline{K}_c}\left(\frac{p_c^{\mathrm{th}}}{\xi_c}\right)_s^{\bullet}+\\&+\frac{\overline{\rho}_i}{\overline{\rho}_w}\frac{\xi_i}{\overline{K}_i}\left(\frac{p_i^{\mathrm{th}}}{\xi_i}\right)_s^{\bullet}+\frac{1}{\xi_w+\xi_c}\left[\frac{\xi_w}{\overline{K}_w}\operatorname{grad}\left(\frac{p_w^{\mathrm{th}}}{\xi_w}\right)+\frac{\xi_c}{\overline{K}_c}\operatorname{grad}\left(\frac{p_c^{\mathrm{th}}}{\xi_c}\right)\right]\cdot\mathbf{J}_{\beta^f}+\operatorname{div}\mathbf{J}_{\beta^f}=0\end{aligned} \tag{3.20}$$

$$\operatorname{div}\boldsymbol{\sigma}+\sum_{\alpha\in\{s,w,c,i\}}\xi_\alpha\overline{\rho}_\alpha\mathbf{g}=\mathbf{0}, \tag{3.21}$$

$$\sum_{\alpha\in\{s,w,c,i\}} \xi_\alpha \overline{\rho}_\alpha (e_\alpha)^{\bullet}_s + (e_i - e_w)\theta_i + \frac{\xi_w \overline{\rho}_w \operatorname{grad} e_w + \xi_c \overline{\rho}_c \operatorname{grad} e_c}{\xi_w + \xi_c} \cdot \mathbf{J}_{\beta^f} + \operatorname{div}\mathbf{q} - r = 0\,, \quad (3.22)$$

where the mixture Cauchy stress tensor $\boldsymbol{\sigma} = \boldsymbol{\sigma}_s + \boldsymbol{\sigma}_w + \boldsymbol{\sigma}_c + \boldsymbol{\sigma}_i$, the mixture heat flow vector $\mathbf{q} = \mathbf{q}_s + \mathbf{q}_w + \mathbf{q}_c + \mathbf{q}_i$ and the external heat supply r generated by nuclear fuel waste have been introduced. Further, besides the unfrozen fluid content χ the porosity, η, and the mass concentration of solutes, C, can be defined as functions of the molar volume fractions by the following relationships:

$$\eta = 1 - \xi_s\,, \qquad \chi = \frac{\xi_w + \xi_c}{\xi_w + \xi_c + \xi_i}\,, \qquad C = \frac{m_c}{v_{w0}} = \overline{\rho}_{w0} \frac{M_w}{M_c} \frac{\xi_c}{\xi_w}\,, \quad (3.23)$$

where m_c is the mass of solutes and v_{w0} is some constant volume of water.

The constitutive relations are those described above. In particular, the Clausius-Clapeyron's equation (3.18) is used to determine the unfrozen fluid content as a function of η, C, T and $\hat{B}$ (see Figure 3.1).

To represent the hydraulic response of numerical simulations the hydraulic head is introduced by the expression

$$h = \frac{\hat{B}}{\overline{\rho}_{w0} g} + z\,, \quad (3.24)$$

where z is the elevation above some datum.

Furthermore, Coulomb's shear failure analysis for a brittle material is adopted with a linear Mohr envelope (Jaeger and Cook, 1976). The Mohr-Coulomb failure criterion adapted for a saturated rock mass states that shear failure occurs when the effective shear stress τ^{ef} across a critical plane reaches the critical value

$$\tau_c^{\mathrm{ef}} = c + \sigma^{\mathrm{ef}} \tan\phi \quad (3.25)$$

where τ_c^{ef} is the shear strength, σ^{ef} is the effective normal stress across this plane, c is the cohesion and ϕ is the internal friction angle. Failure occurs across a critical plane whose normal is inclined at an angle β to σ^{ef}. This angle is given by

$$\beta = 45° + \phi/2\,. \quad (3.26)$$

To analyse the stability of the rock mass the normal component and the shear component of the effective stress tensor across the critical plane are resolved using the following equations:

$$\sigma^{\mathrm{ef}} = \tfrac{1}{2}\left(\sigma_1^{\mathrm{ef}} + \sigma_3^{\mathrm{ef}}\right) + \tfrac{1}{2}\left(\sigma_1^{\mathrm{ef}} - \sigma_3^{\mathrm{ef}}\right)\cos(2\beta), \quad (3.27)$$

$$\tau^{\mathrm{ef}} = \tfrac{1}{2}\left(\sigma_1^{\mathrm{ef}} - \sigma_3^{\mathrm{ef}}\right)\sin(2\beta), \quad (3.28)$$

where σ_1^{ef} and σ_3^{ef} are the major and the minor principal effective stresses, respectively.

To determine whether the rock would fail, the factor of safety FS is established as follows:

$$FS = \frac{\tau_c^{\mathrm{ef}}}{\left|\tau^{\mathrm{ef}}\right|}. \tag{3.29}$$

If $FS > 1$, the rock would be stable. If $FS \leq 1$, shear failure would occur. It should be noted that, since Equation (3.25) is valid for shear failure analysis under compressive normal effective ($\sigma^{\mathrm{ef}} \geq 0$), $\tau_c^{\mathrm{ef}} \geq 0$.

Tensile failure is evaluated by comparing any effective normal stress component with the appropriate tensile strength.

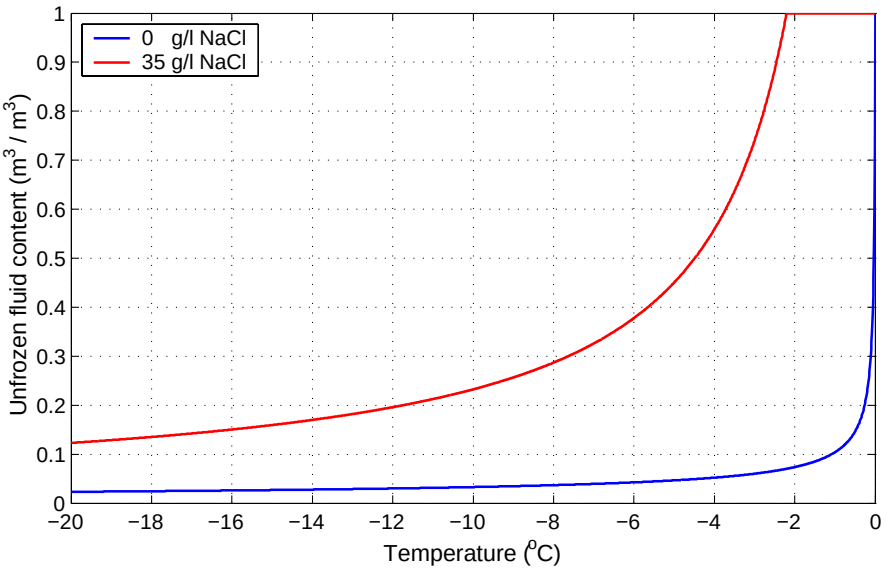

Figure 3.1: Unfrozen fluid content versus temperature for fresh water, as $C^0 = 0$ *(colour blue) and for saline water, as* $C^0 = 35\ \mathrm{gl}^{-1}$, *(colour red). Further,* $\Lambda = 1.06 \times 10^{-4}$, $\eta = \eta^0$ *and* $\hat{B} = 0$.

3.3 Finite element method

Permafrost problem is solved by the finite element method using the methodology, which is described in Mikkola and Hartikainen (2002).

4 Numerical simulations and results

Numerical simulations are based on the conceptual models described in Chapter 3.

4.1 Phase I modelling

4.1.1 Boundary and initial conditions

The bottom boundary is assumed to be impermeable, immobile and subjected to a geothermal heat low $\phi_{\mathrm{B}}^{T} = 0.04\ \mathrm{Wm}^{-2}$:

$$\mathbf{J}_{\beta f} \cdot \mathbf{n} = 0, \qquad \mathbf{u}_s = \mathbf{0}, \qquad \mathbf{q} \cdot \mathbf{n} = \phi_{\mathrm{B}}^{T}, \tag{4.1}$$

where $\mathbf{n}$ is the outward unit normal vector of the boundary. The side boundaries are given a prescribed hydrostatic pressure distribution and zero-normal displacements and assumed to be adiabatic:

$$\hat{B} = \overline{\rho}_{w0} g \Delta z, \qquad \mathbf{u}_s \cdot \mathbf{n} = 0, \qquad \mathbf{q} \cdot \mathbf{n} = 0, \tag{4.2}$$

where Δz is the depth below ground surface. The surface boundary is given a zero-pressure boundary condition when permafrost is absent and assumed to be impermeable when permafrost is present. Further, the boundary is unloaded and given the prescribed mean annual surface temperature T_{S}, Figure 2.4:

$$\begin{matrix} \hat{B} = 0 \quad \text{(permafrost absent)} \\ \mathbf{J}_{\beta f} \cdot \mathbf{n} = 0 \quad \text{(permafrost present)} \end{matrix}, \qquad \boldsymbol{\sigma} \cdot \mathbf{n} = \mathbf{0}, \qquad T = T_{\mathrm{S}} \tag{4.3}$$

The initial conditions are defined as

$$\hat{B}(\mathbf{x}, t^0) = \hat{B}^0(\mathbf{x}), \qquad \mathbf{u}_s(\mathbf{x}, t^0) = \mathbf{0}, \qquad T(\mathbf{x}, t^0) = T^0(\mathbf{x}), \tag{4.4}$$

where the values of initial pore pressure $\hat{B}^0$ and initial temperature T^0 are obtained from the stationary solution with the prescribed boundary conditions at the initial time $t^0 = 0$.

4.1.2 Computations

A finite element mesh of 68417 linear triangular elements (35026 nodes) was used. A simulation with the above boundary conditions was performed.

4.1.3 Summary of results

Permafrost developed progressively into the repository depth (~540 m) in about 70000 at the site, which was out of the range affected by the heat production of waste, and in

about 90000 at the repository site. The maximum permafrost depth was approximately 600 m at the repository site and about 700 m far from the repository site.

As permafrost developed, the excess pore pressure, i.e. $B_e = \hat{B} - \overline{\rho}_{w0} g \Delta z$, was found to increase to the value of about 1.5 MPa in the repository and to the value of approximately 5.5 MPa located in the rock mass at the depth of 250 m below the ground surface.

The calculated maximum frost heave range between 0.08 m and 0.23 m would indicate that frost heaving occurred principally due to the increase in volume of in situ water in freezing. The maximum frost heaves were located at the sites of the fracture zones.

4.2 Phase II modelling

4.2.1 Boundary and intial conditions

The bottom boundary is assumed to be impermeable and immobile and subjected to a geothermal heat flow ϕ_B^T, which varies between 0.04 and 0.06 Wm^{-2}:

$$\mathbf{J}_{\beta f} \cdot \mathbf{n} = 0, \qquad \mathbf{u}_s = \mathbf{0}, \qquad \mathbf{q} \cdot \mathbf{n} = \phi_B^T . \tag{4.5}$$

The surface boundary is given a prescribed water pressure corresponding to ground water head h_G, Figure 2.6, a prescribed mechanical ice load corresponding to ice sheet thickness H, Figure 2.6, and a prescribed surface temperature T_S, Figure 2.5:

$$\hat{B} = \overline{\rho}_{w0} g h_G , \qquad \boldsymbol{\sigma} \cdot \mathbf{n} = \overline{\rho}_{i0} \mathbf{g} H , \qquad T = T_S . \tag{4.6}$$

The initial conditions are defined as

$$\hat{B}(\mathbf{x}, t^0) = \hat{B}^0(\mathbf{x}), \qquad \mathbf{u}_s(\mathbf{x}, t^0) = \mathbf{0}, \qquad T(\mathbf{x}, t^0) = T^0(\mathbf{x}) , \tag{4.7}$$

where the values of initial pore pressure $\hat{B}^0$ and initial temperature T^0 are obtained from the stationary solution with the prescribed boundary conditions at the initial time $t^0 = 120000$ years before present.

4.2.2 Computations

A finite element mesh consisting of 2000 linear two-node elements was used. Several simulations were performed considering fresh and saline ground water with the identical hydro-mechanical but distinct thermal boundary conditions described above.

4.2.3 Results and discussions

In general, it was found that the thermal response of subsurface is rapid to the changes in the circumstances on the ground surface. Further, an increase of 0.02 Wm^{-2} in the geothermal heat flow reduced permafrost depth about 130-170 m while approximately 150-190 m shallower permafrost was generated by Mild surface temperatures than by

Cold surface temperatures. The essential results concerning permafrost development, i.e. the 0 °C-isotherm, and creation and degradation of perennially frozen ground for Case A, i.e. Cold surface temperature and geothermal heat flow of 0.04 Wm^{-2}, and for Case D, i.e. Mild surface temperature and geothermal heat flow 0.06 Wm^{-2}, are presented in the following.

Figures 4.1 and 4.2 demonstrate that salinity of ground water has a minor effect on permafrost development but a significant impact on perennial freezing of subsurface. The increase in thickness of permafrost is less than one meter, whereas the reduction in thickness of perennially frozen subsurface is approximately 70-140 m, as summarized in Table 4.1. The former correlates to the small change in thermal properties, as water freezes in low-porosity rock, and the latter to the decrease in the freezing point due to salinity. This was also seen as a small variation (less than 0.2 °C) in the subsurface temperatures (Figure 4.3) between the fresh and saline ground water.

The perennial freezing and, especially, the perennial thawing of subsurface are affected further by pore pressure (Figure 4.4). The reduction in the thickness of perennially frozen subsurface during pre-glacial periods is approximately 20-47 m. The increase in pore pressure due to the glacier loading decreases the melting point and hence, enhances thawing of subglacial bed creating an unfrozen zone at sub-zero temperatures. It was found that a perennially frozen subglacial zone thaws in about 2500 years for Case A and in about 1500 years for Case D, whereas a rather thick (~100 m) permafrost zone is sustained the whole glacial stage.

Table 4.1: Maximum thickness of permafrost and perennially frozen subsurface.

Thickness (m)	Case A		Case D	
	Fresh	Saline	Fresh	Saline
Permafrost	783.8	784.4	462.0	462.2
Perennially frozen	736.4	597.3	441.4	371.4

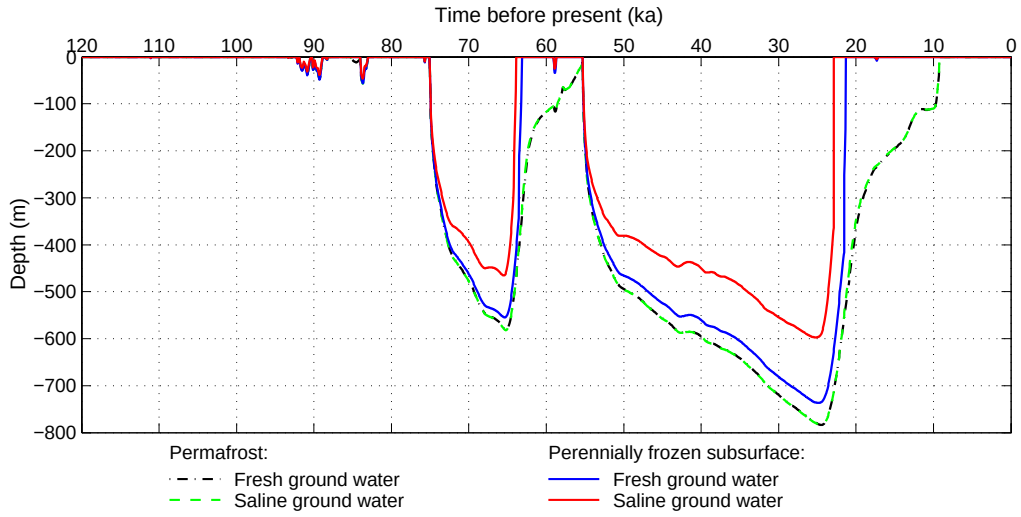

Figure 4.1: Evolution of permafrost depth (0 ℃-isotherm) and the depth of perennially frozen subsurface. Case A (Cold surface temperature, geothermal heat 0.04 Wm^{-2}).

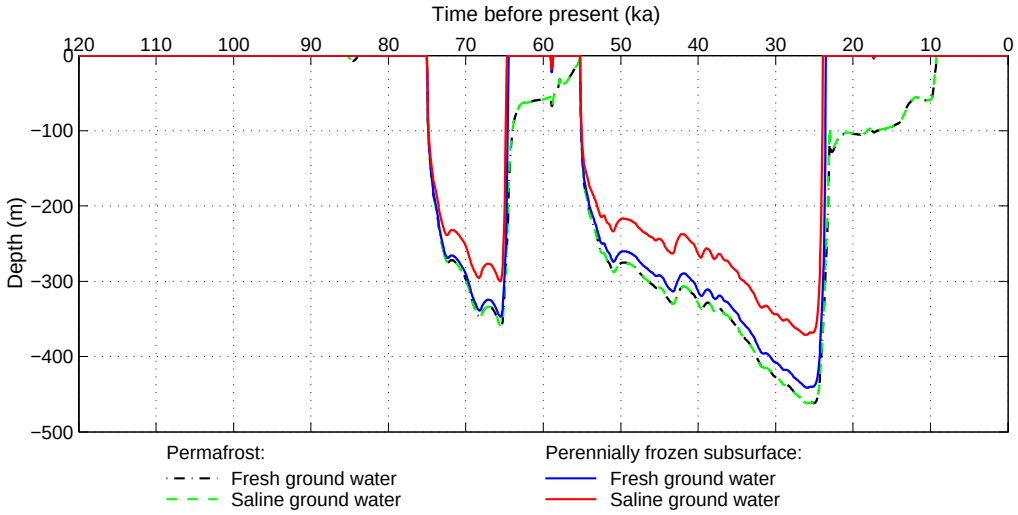

Figure 4.2: Evolution of permafrost depth (0 ℃-isotherm) and the depth of perennially frozen subsurface. Case D (Mild surface temperature, geothermal heat 0.06 Wm^{-2}).

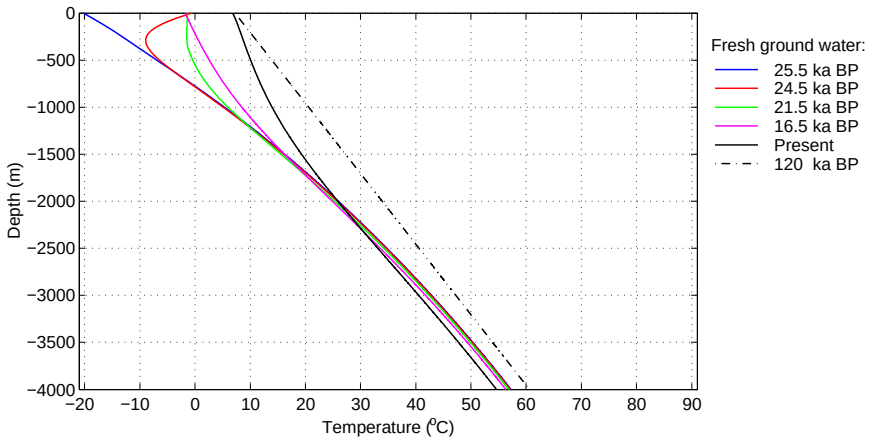

Figure 4.3: Temperature along the vertical segment trough the centre of repository in time. Case A (Cold surface temperature, geothermal heat 0.04 Wm^{-2}).

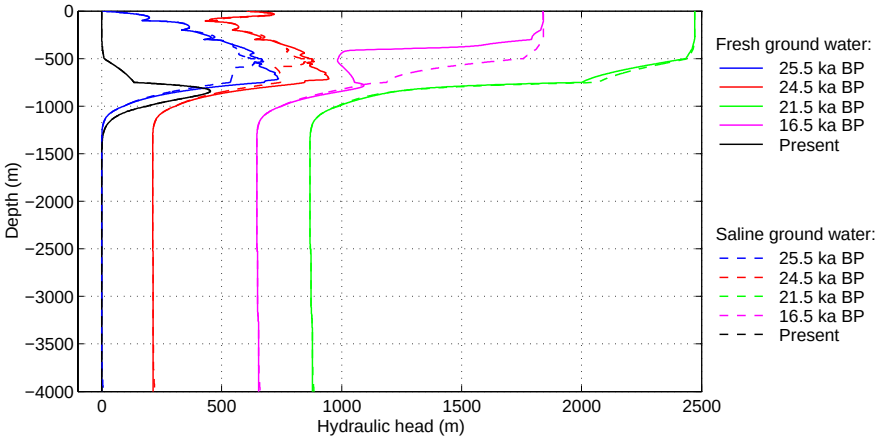

Figure 4.4: Hydraulic head along the vertical segment trough the centre of repository in time. Case A (Cold surface temperature, geothermal heat 0.04 Wm^{-2}).

4.3 Phase III modelling

4.3.1 Boundary and initial conditions

The bottom boundary is assumed to be impermeable, immobile and subjected to a geothermal flow $\phi_{\mathrm{B}}^{T} = 0.04\ \mathrm{Wm}^{-2}$:

$$\mathbf{J}_{\beta f} \cdot \mathbf{n} = 0, \qquad \mathbf{u}_s = \mathbf{0}, \qquad \mathbf{q} \cdot \mathbf{n} = \phi_{\mathrm{B}}^{T}. \tag{4.8}$$

The down-glacier boundary, i.e. the left side boundary, is assigned a prescribed hydrostatic pressure corresponding to the variation in ice sheet thickness H at the top boundary, Figure 2.8, and zero-normal displacements and assumed to be adiabatic:

$$\hat{B} = \overline{\rho}_{w0} g \Delta z + \overline{\rho}_{i0} g H, \qquad \mathbf{u}_s \cdot \mathbf{n} = 0, \qquad \mathbf{q} \cdot \mathbf{n} = 0. \tag{4.9}$$

The up-glacier boundary, i.e. the right side boundary, is given a prescribed hydrostatic pressure distribution when glacier is absent and a prescribed water flow $\phi_{\mathrm{R}}^{\hat{B}}$ when glacier is present, zero-normal displacements, and is assumed to be adiabatic:

$$\begin{matrix} \mathbf{J}_{\beta f} \cdot \mathbf{n} = \phi_{\mathrm{R}}^{\hat{B}} & \text{(glacier present)} \\ \hat{B} = \overline{\rho}_{w0} g \Delta z & \text{(glacier absent)} \end{matrix}, \qquad \mathbf{u}_s \cdot \mathbf{n} = 0, \qquad \mathbf{q} \cdot \mathbf{n} = 0. \tag{4.10}$$

The water flow $\phi_{\mathrm{R}}^{\hat{B}}$ is assumed to be a piecewise constant function of horizontal permeability described by the relationship $\phi_{\mathrm{R}_I}^{\hat{B}} = \chi^{5}\left(\kappa_{\mathrm{H}_I} \big/ \sum_J \kappa_{\mathrm{H}_J} \Delta h_J\right) \Phi_{\mathrm{R}}^{\hat{B}}$, where κ_{H_I} and Δh_I, respectively, are the horizontal permeability and the approximate thickness of Layer *I* given in Table 2.2 and $\Phi_{\mathrm{R}}^{\hat{B}}$ is the ground water flux across the right side boundary in time shown in Figure 2.10.

The surface boundary is divided into three parts:

a. The glacier free part is unloaded and given a zero-pressure boundary condition and surface temperatures T_{S}, Figure 2.7:

$$\hat{B} = 0, \qquad \boldsymbol{\sigma} \cdot \mathbf{n} = \mathbf{0}, \qquad T = T_{\mathrm{S}}. \tag{4.11a}$$

b. The glacier covered part when no basal melting occurs is given a zero-pressure boundary condition, a prescribed ice load corresponding to the ice sheet thickness H, Figure 2.8, and a prescribed heat flow ϕ_{S}^{T} corresponding to the excess heat production, Figure 2.9:

$$\hat{B} = 0, \qquad \boldsymbol{\sigma} \cdot \mathbf{n} = \overline{\rho}_{i0} \mathbf{g} H, \qquad \mathbf{q} \cdot \mathbf{n} = \phi_{\mathrm{S}}^{T}. \tag{4.11b}$$

c. The glacier covered part when basal melting occurs is given the prescribed ice load, Figure 5.5. Temperature equals to the pressure melting point defined by the Clausius-Clapeyron equation (3.18) and water flow is equivalent to the basal melt rate, which is determined trough the mass balance and the energy balance at

the interface. In addition, the pore pressure is constrained to not exceed the value corresponding to the variation in ice sheet thickness H :

$$\mathbf{J}_{\beta^f} \cdot \mathbf{n} = \frac{\mathbf{q} \cdot \mathbf{n} - \phi_S^T}{\overline{\rho}_{w0} \ell}, \qquad \boldsymbol{\sigma} \cdot \mathbf{n} = \overline{\rho}_{i0} \mathbf{g} H, \qquad T = T_m. \qquad (4.11c)$$
$$\hat{B} \le \overline{\rho}_{i0} g H$$

The initial conditions are defined as

$$\hat{B}(\mathbf{x}, t^0) = \hat{B}^0(\mathbf{x}), \qquad \mathbf{u}_s(\mathbf{x}, t^0) = \mathbf{0}, \qquad T(\mathbf{x}, t^0) = T^0(\mathbf{x}), \qquad (4.12)$$

where the values of initial pore pressure $\hat{B}^0$ and initial temperature T^0 are obtained from the stationary solution with the prescribed boundary conditions at the initial time $t^0 = 120000$ years before present.

4.3.2 Computations

A finite element mesh consisting of 66884 linear triangular elements (34008 nodes) was used. The following scenarios were simulated:

- the cold scenario (cold surface temperatures),
- the warm scenario (warm surface temperatures) and
- the permafrost free scenario assuming the subsurface to be unfrozen and considering the glacier forcing described previously besides the hydraulic boundary condition on the top boundary, which was given a prescribed hydrostatic pressure corresponding to the variation in ice sheet thickness, i.e. $\hat{B} = \overline{\rho}_{i0} g H$.

4.3.3 Results and discussions

The simulations have generated a considerable amount of results from which a relevant subset is presented herein. Points and verticals for presentation of time histories of variables are shown schematically in Figure 4.5.

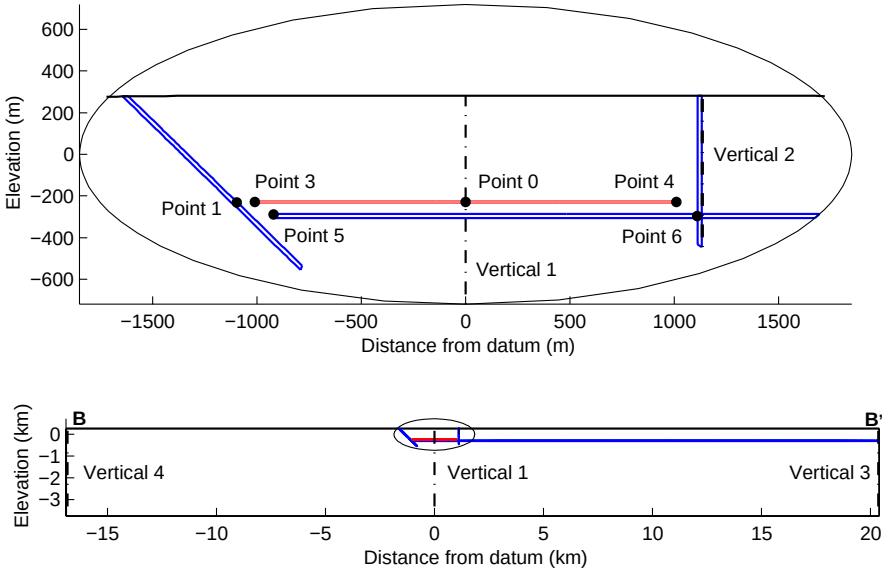

Figure 4.5: Locations of points verticals for history plotting.

4.3.3.1 Thermal response

It was found that after the onset of reposition of the fuel waste (at 82000 years before present) the temperature in the middle of the repository (Point 0) increased by +47.5 °C from +8.9 °C to +56.4 °C for the cold scenario and from +5.9 °C to +53.4 °C for the warm scenario in approximately 150 years, and decreased then to the minimum values of about –3.2 °C for the cold scenario and about +4.8 °C for the warm scenario occurring approximately 1200 years after the onset of glaciation (at 22650 years before present) (see Figure 4.6). It can be seen that the heating effect of fuel waste decays rather sharply in the horizontal direction (Figure 4.6 and the curves at 81850 years before present in Figures 4.12 and 4.14). This effect can be also noticed in the evolution of permafrost depth (0 °C-isotherm) which is shown in Figures 4.7 and 4.8 for the cold and warm scenarios, respectively, at four selected verticals – Vertical 1 the centre line of the model domain, Vertical 2 the right edge of the vertical fracture zone, Vertical 3 the right side boundary and Vertical 4 the left side boundary. In general, the reduction in permafrost thickness due to the heat production of fuel waste is approximately 50-150 m (see Table 4.2).

The heat generation of fuel waste has evidently an impact on perennial freezing and thawing of subsurface too. The evolution of perennially frozen subsurface follows the development of permafrost under non-glacial conditions. Under glacial conditions the subsurface thaws upwards due to the geothermal heat and downwards due to the basal shear heating of the ice sheet. A notable effect of the heat production could be seen in the rate of subglacial thawing, e.g. for the cold scenario a ~630 m thick perennially frozen zone at the centre line thawed in approximately 2580 years (Figure 4.9), while a ~790 m thick zone at the right side boundary thawed in about 4640 years (Figure 4.10). Consequently, a discontinuous perennially frozen subglacial wedge was generated (see Figures 4.11 and 4.13). It was seen that beneath the advancing glacier the perennially frozen subglacial wedge, ~26 km deep with a ~4 km wide cold margin at the ice\bed interface for the warm scenario (much larger for the cold scenario), degraded in about

2700 years for the warm scenario and in about 5900 years for the cold scenario, whereas a quite thick subglacial permafrost zone survived and even grew for the warm scenario.

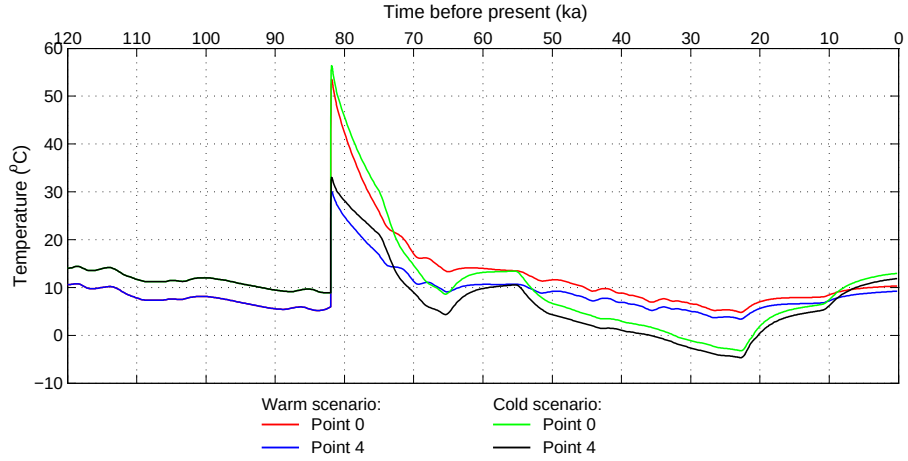

Figure 4.6: Evolution of temperature in the repository. Cold and warm scenarios.

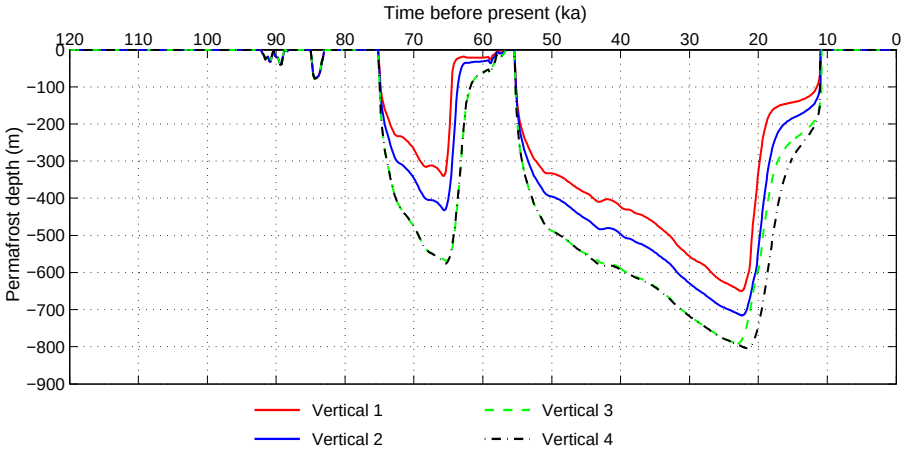

Figure 4.7: Evolution of permafrost depth at Verticals 1, 2, 3 and 4. Cold scenario.

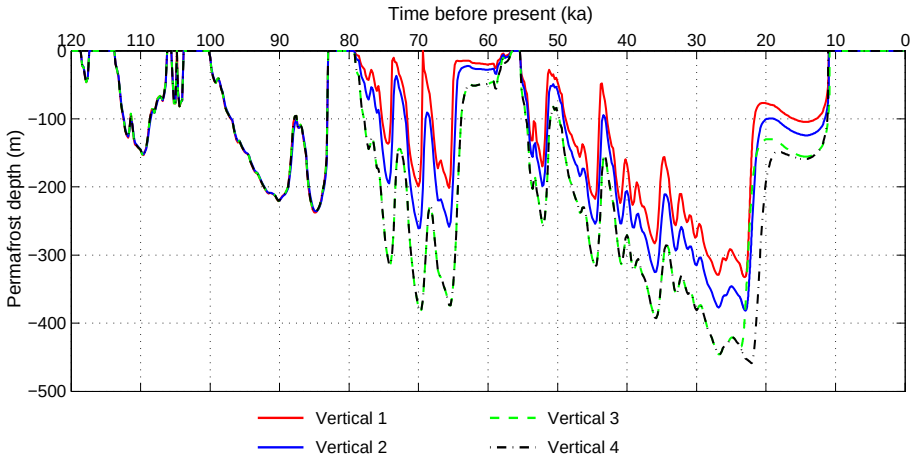

Figure 4.8: Evolution of permafrost depth at Verticals 1,2,3 and 4. Warm scenario.

Table 4.2: Maximum values of permafrost thickness in (m) at Verticals 1, 2, 3 and 4.

Scenario	Vertical 1	Vertical 2	Vertical 3	Vertical 4
Cold	650	716	791	804
Warm	332	382	435	459

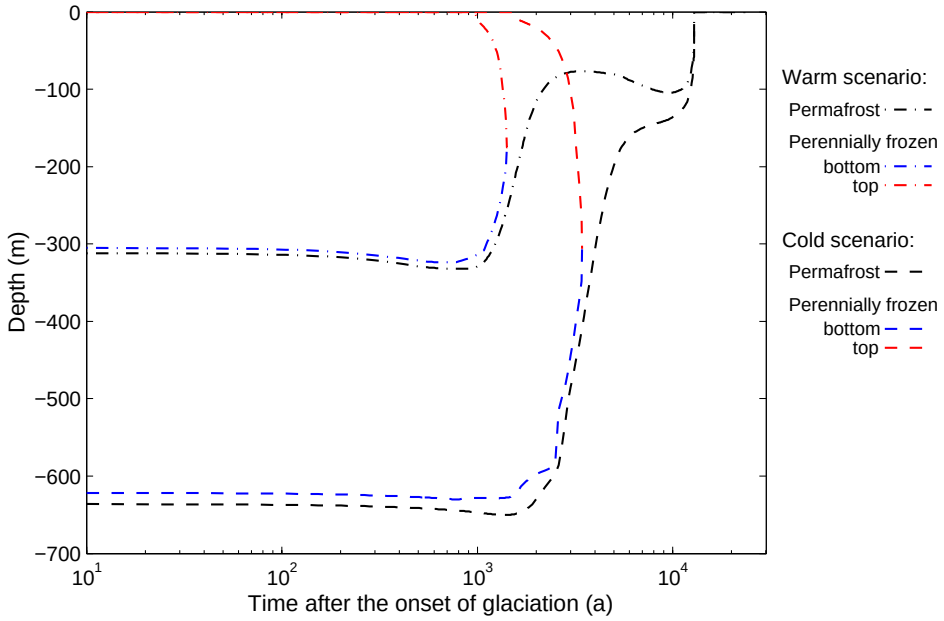

Figure 4.9: Evolution of permafrost depth (0 ℃-isotherm) and the depth of perennially frozen subsurface at the centre line of the model domain (Vertical 1). Cold and warm scenarios.

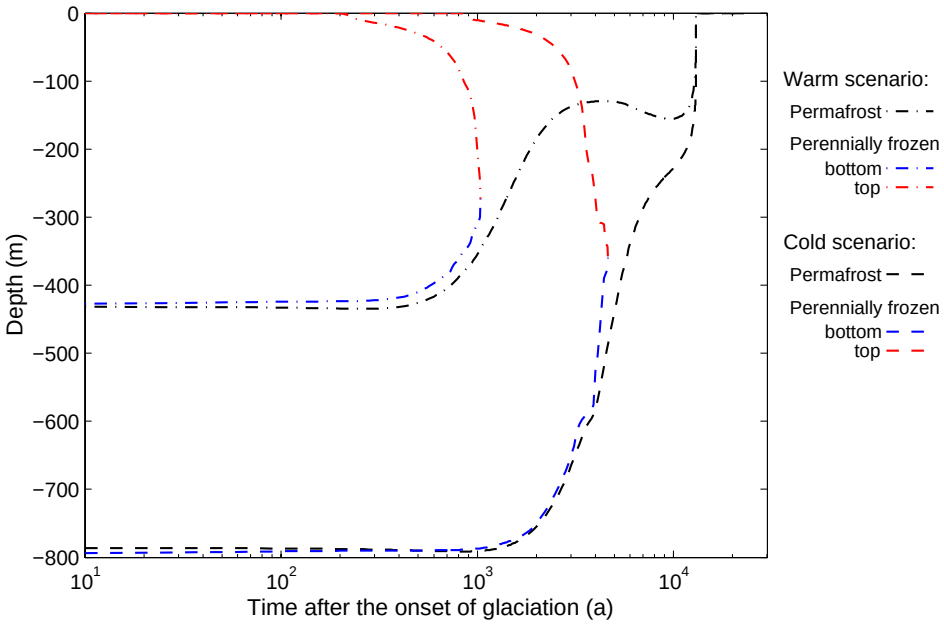

Figure 4.10: Evolution of permafrost depth (0 ℃-isotherm) and the depth of perennially frozen subsurface at the right side boundary (Vertical 3). Cold and warm scenarios.

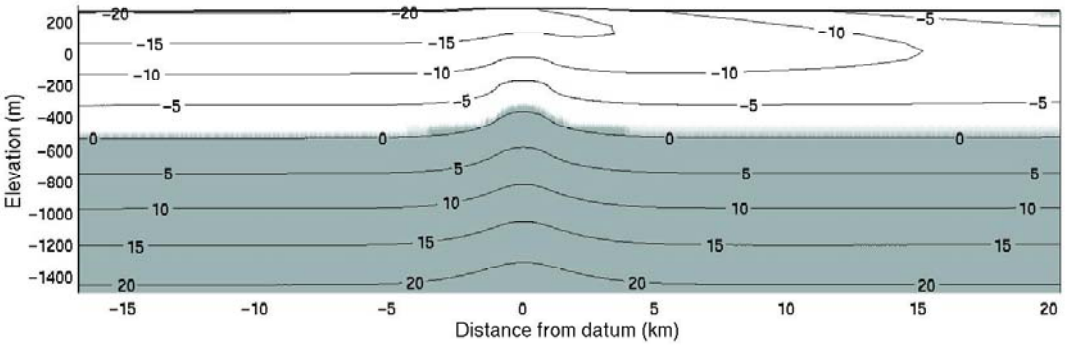

a) At 23000 years before present (856 years after the onset of glaciation).

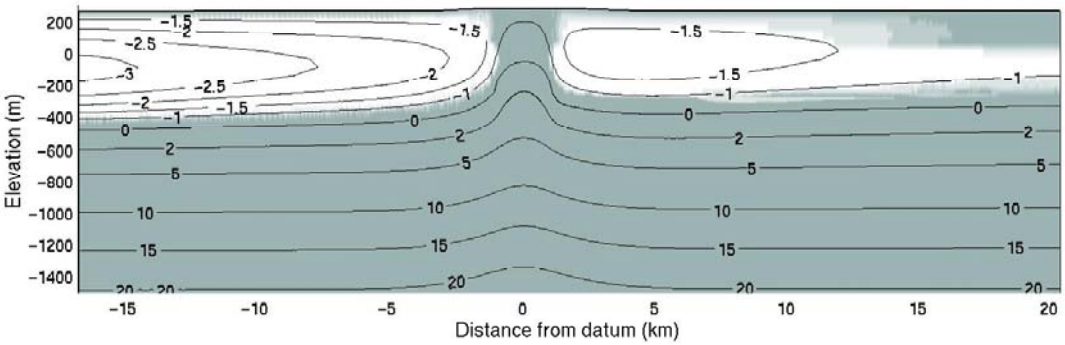

b) At 20000 years before present (3856 years after the onset of glaciation).

Figure 4.11: Temperature contours in (ºC) and extent of perennially frozen (colour white) and unfrozen (colour grey) subsurface. Cold scenario.

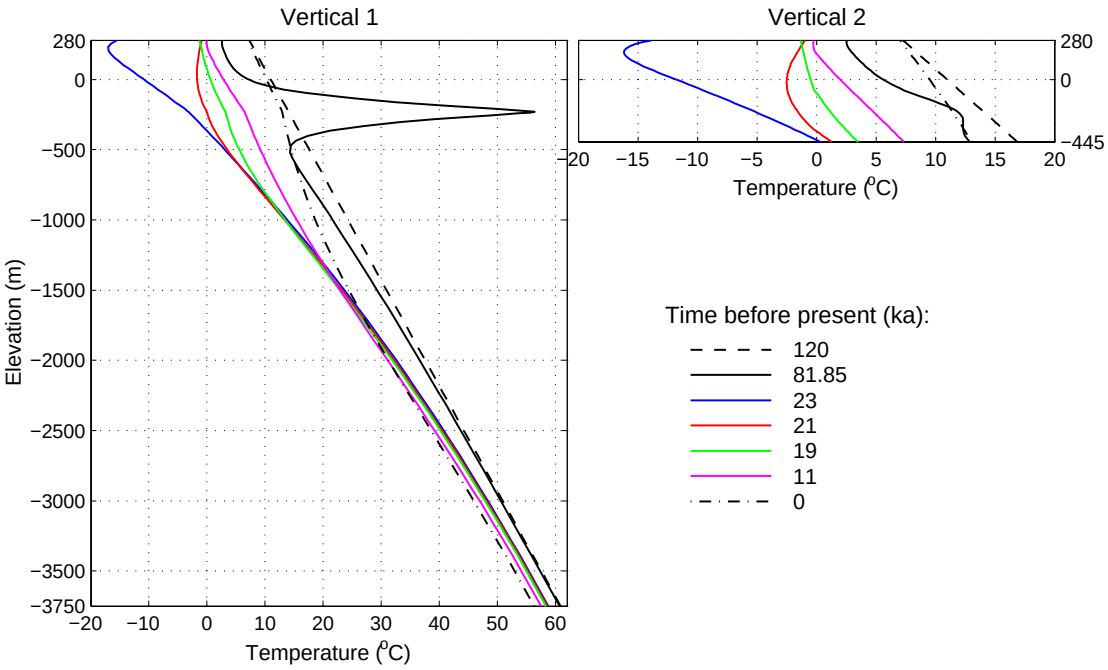

Figure 4.12: Vertical profile of temperature through the centre of repository (Vertical 1) and along the right edge of vertical fracture zone (Vertical 2). Cold scenario.

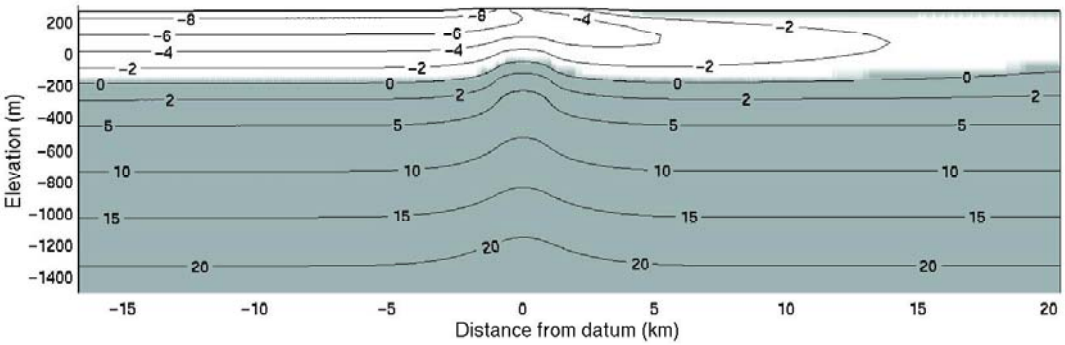

a) At 23000 years before present (856 years after the onset of glaciation).

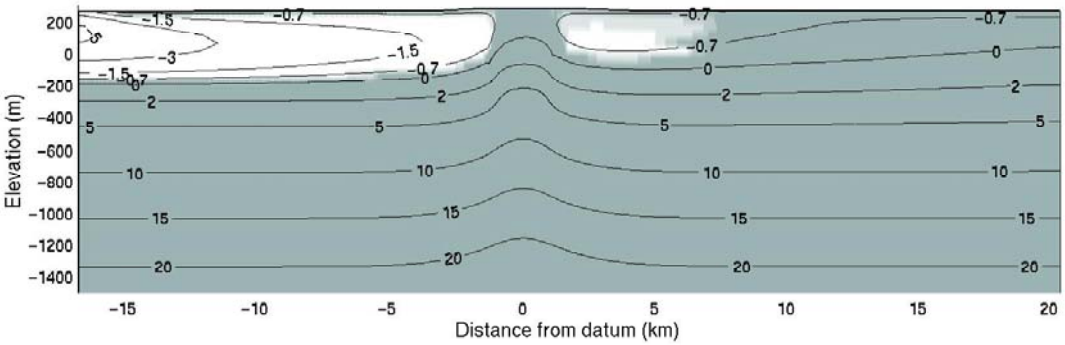

b) At 22200 years before present (1656 years after the onset of glaciation).

Figure 4.13: Temperature contours in (ºC) and extent of perennially frozen (colour white) and unfrozen (colour grey) subsurface. Warm scenario.

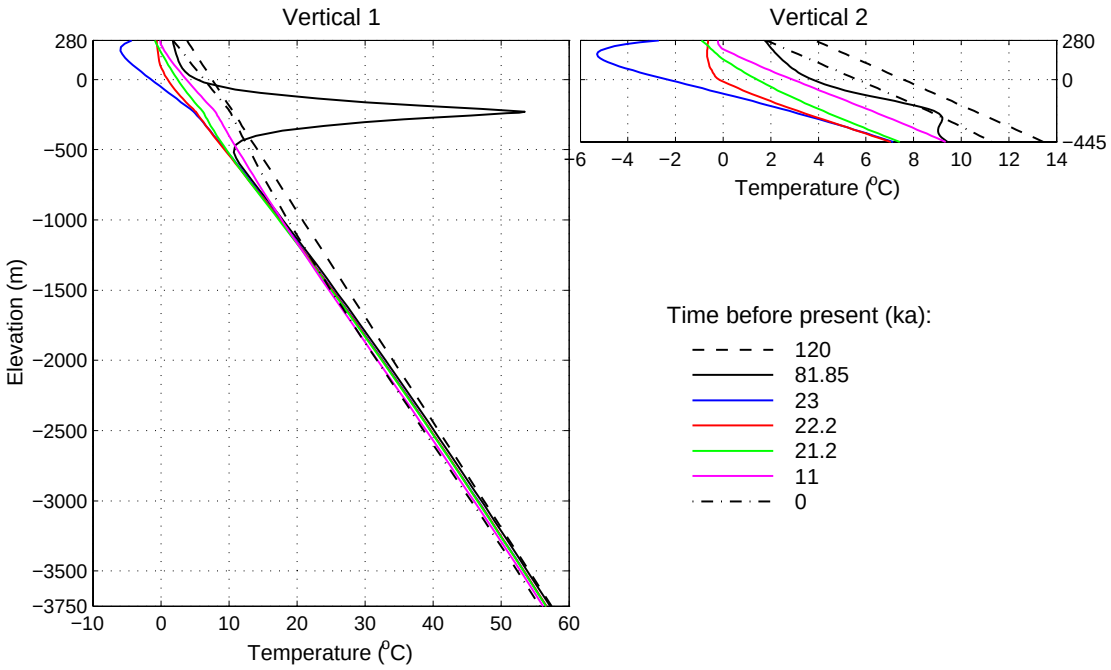

Figure 4.14: Vertical profile of temperature through the centre of repository (Vertical 1) and along the right edge of vertical fracture zone (Vertical 2). Warm scenario.

4.3.3.2 Hydraulic response

It was found that during the pre-glacial period (23856-55300 years before present) the subsurface hydraulic head increased from the initial value of ~280 masl (metres above present-day mean sea level) up to ~1069 masl for the cold scenario and up to ~606 masl for the warm scenario (see the curves at 23856 years before present in Figures 4.18 and 4.20 as well as Figures 4.17a and 4.19a). The maximum pre-glacial hydraulic head occurred in the horizontal fracture zone below the repository for the cold scenario and in the dipping fracture zone as well as in the vertical fracture zone at the depth of ~150 m for the warm scenario. It was also seen that an excess pore pressure with a downward hydraulic gradient was generated in the perennially unfrozen zone alongside the base of the perennially frozen zone. A presumable cause for this could be that the resistance of rock matrix to the expansion of pore space due to the volume increase of freezing water generates a pushing force, which exceeds the pulling force due to the cryogenic suction, and hence, water is pushed from the freezing front to the unfrozen zone.

The evolution of the subsurface hydraulic head for three locations at approximately 500-m depth below ground surface – Point 1 in the dipping fracture zone, Point 4 in the repository and Point 6 in the horizontal fracture zone – and for three prescribed scenarios from the onset of glaciation to the present day is shown in Figure 4.15. Four major findings concerning the impact of perennial freezing and thawing on the subglacial hydraulic head can be pointed out:

1. There is an abrupt drop of ~300-700 m in the hydraulic head for the cold scenario around 2000-3000 years after the onset of glaciation (see the curves for the cold for the cold scenario in Figure 4.15 and the curves at 21000 years before present in Figure 4.18). This is mainly a consequence of the volume decrease of melting ice.

2. For the warm scenario the horizontal Darcy velocity increases by ~0.01 ma^{-1} (Point 6, Figure 4.16) and the hydraulic head by ~100-500 m (see the curves for the warm scenario in Figure 4.15 as well as Figure 4.19a) in about 1000 years after the onset of glaciation. This is plausibly due to that the subpermafrost ground water flow is not able to discharge through the less permeable perennially frozen zone.

3. Once the pore ice is melted, the hydraulic head increases rapidly (see Figure 4.15 as well as Figures 4.17b and 4.19b). This is likely due to the compression of pores by the mechanical loading of the ice sheet. A minor cause is the basal water inflow.

4. The minimal variation in the values of hydraulic head between the permafrost and permafrost free scenarios (see Figure 4.15), once the subglacial bed is thawed, indicates that direct hydraulic impacts of perennial ground freezing are difficult to observe after glaciation.

A large downward hydraulic gradient (2-20 m/m) can bee seen in the transition zone between the perennially frozen and unfrozen subglacial bed as well as in the unfrozen zone below the depth of ~650 m. This is associated with the large frozen/unfrozen as well as initial permeability contrast in the bedrock. As the glacier advances over the site, there are horizontal hydraulic gradients all the way down to the bottom of the model (4 km). This effect is related to the compression of pore space by the glacier loading.

An interesting result can be detected in the basal melt rate, which is shown for the warm scenario in Figure 4.21. The melt rate for the cold scenario was about 1-3 mm a^{-1} less

than that for the warm scenario. The basal melt rate at the repository site is about 5-20% higher than the basal melt rate near the side margins of the model domain. This is apparently a consequence of the subglacial heat production from the repository even though the amount is quite small (~0.0027 Wm^{-3} at 23000 years before present).

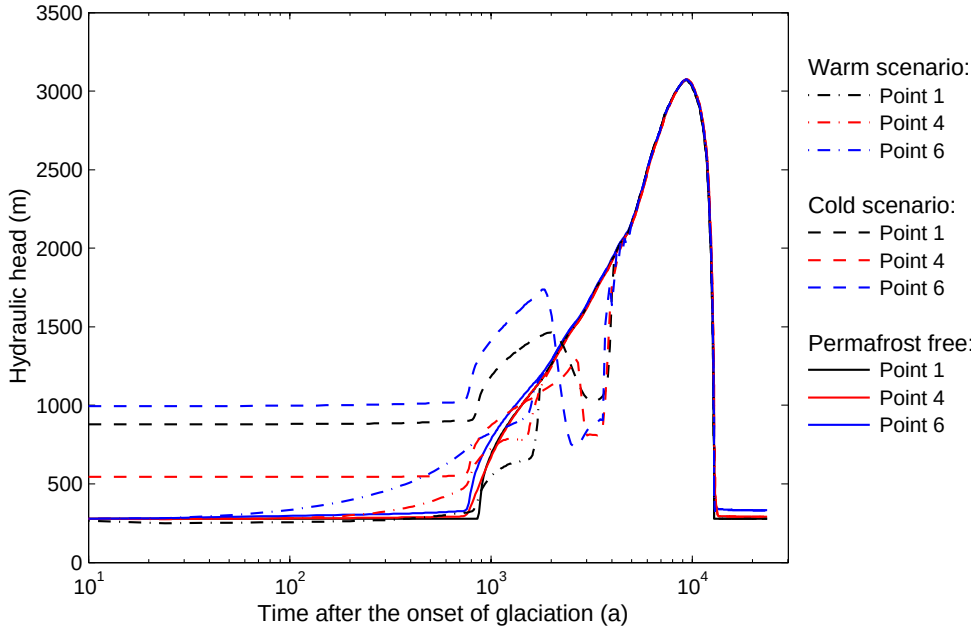

Figure 4.15: Evolution of hydraulic head in (masl) in the dipping fracture zone (Point 1), in the repository (Point 4) and in the horizontal fracture zone (Point 6).

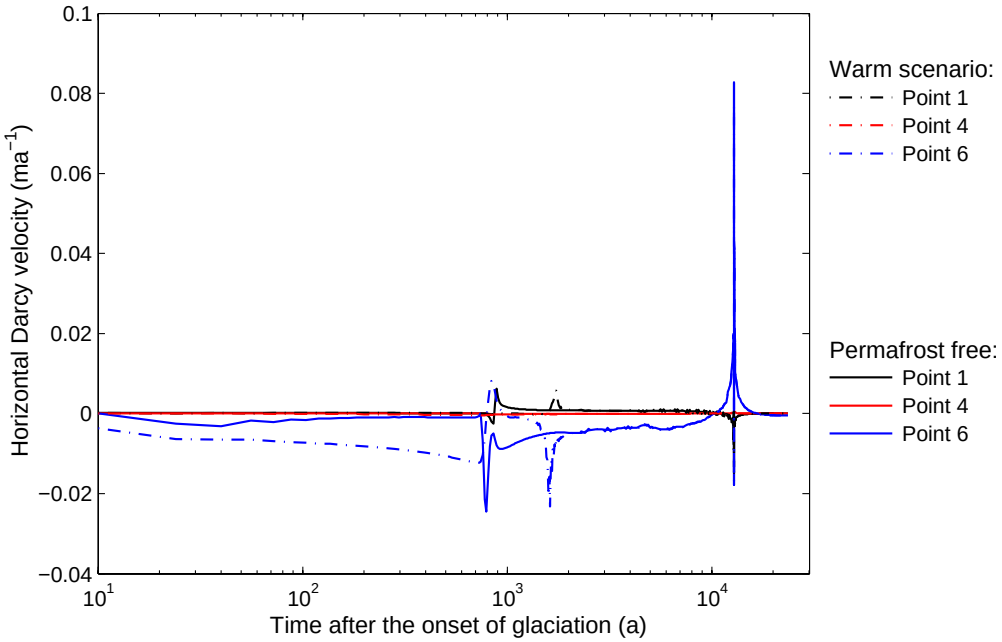

Figure 4.16: Evolution of horizontal Darcy velocity in the dipping fracture zone (Point 1), in the repository (Point 4) and in the horizontal fracture zone (Point 6).

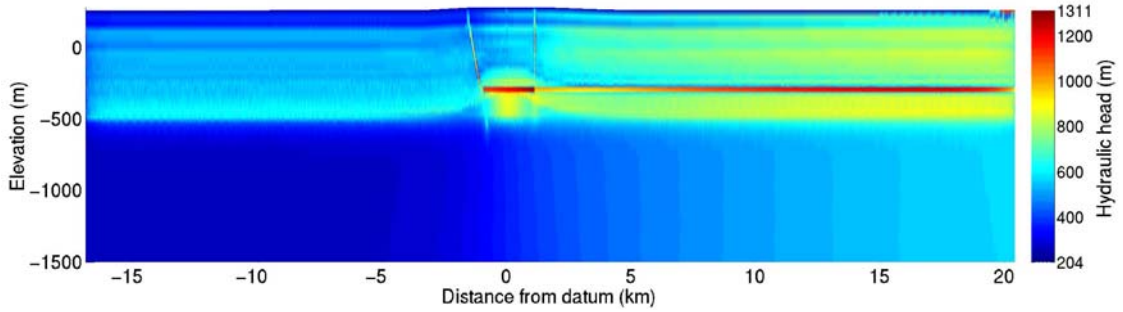

a) At 23000 years before present (856 years after the onset of glaciation).

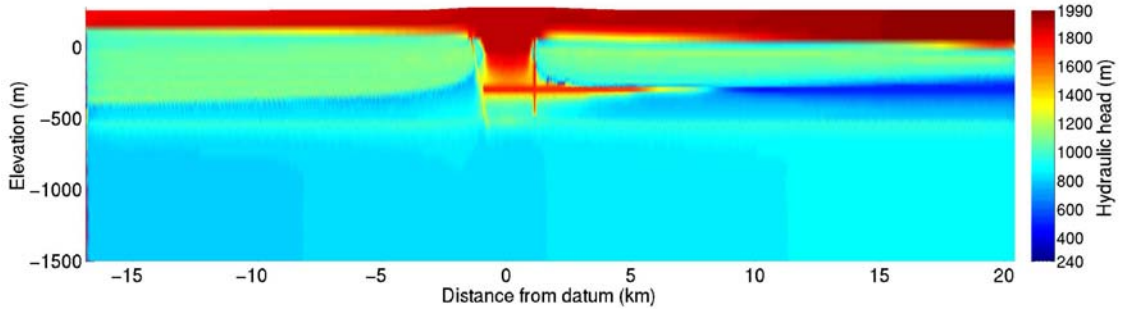

b) At 20000 years before present (3856 years after the onset of glaciation).

Figure 4.17: Hydraulic head field in (masl). Cold scenario.

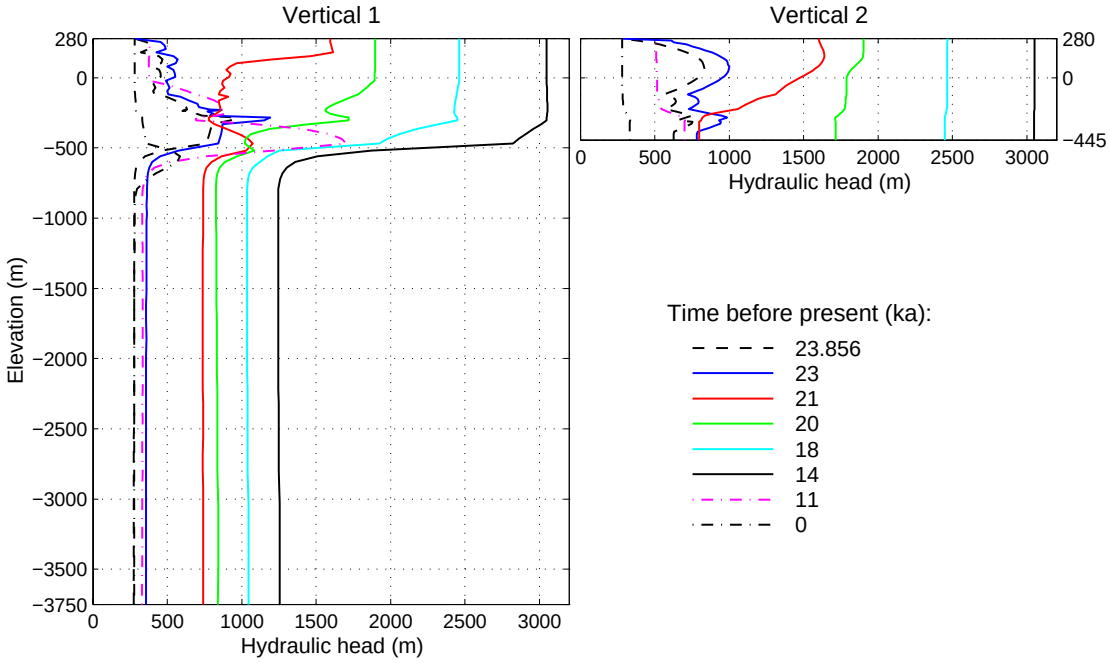

Figure 4.18: Vertical profile of hydraulic head in (masl) through the centre of repository (Vertical 1) and along the right edge of vertical fracture zone (Vertical 2). Cold scenario.

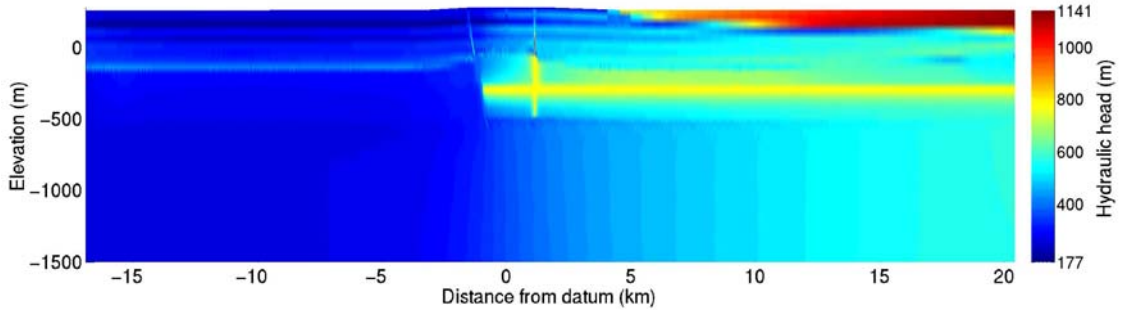

a) At 23000 years before present (856 years after the onset of glaciation).

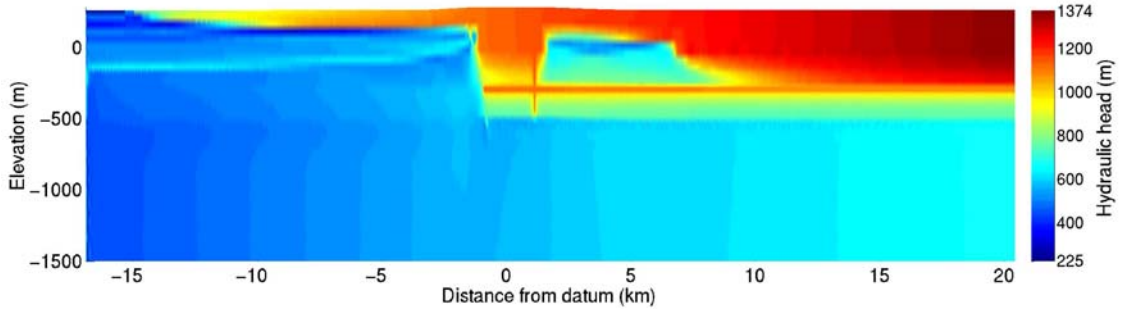

b) At 22200 years before present (1656 years after the onset of glaciation).

Figure 4.19: Hydraulic head field (masl). Warm scenario.

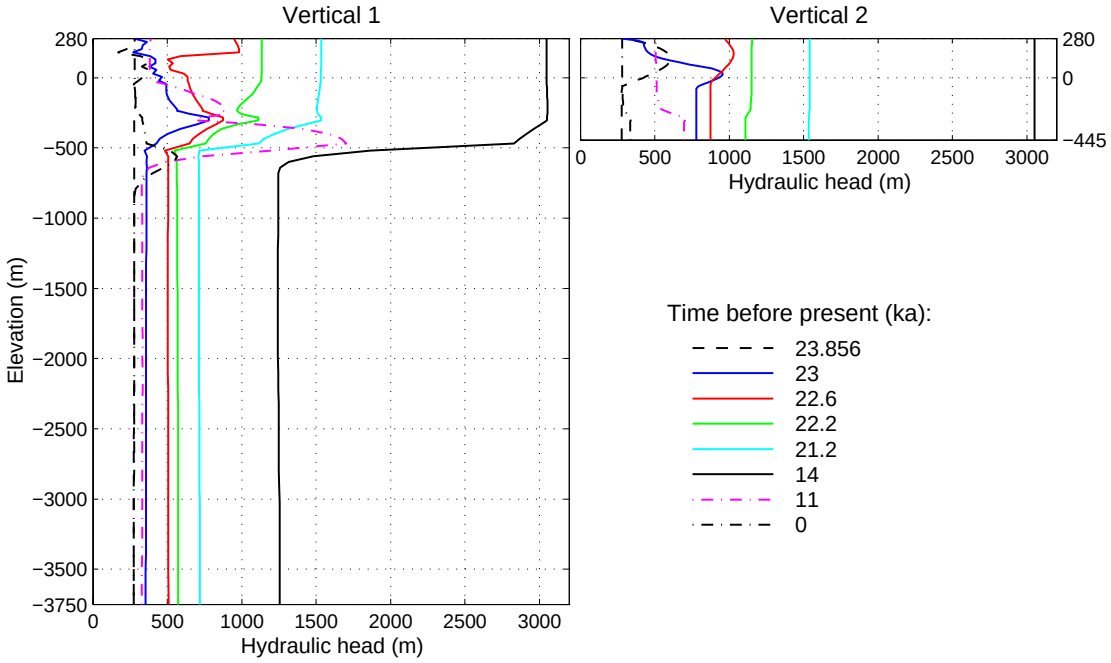

Figure 4.20: Vertical profile of hydraulic head in (masl) through the centre of repository (Vertical 1) and along the right edge of vertical fracture zone (Vertical 2). Warm scenario.

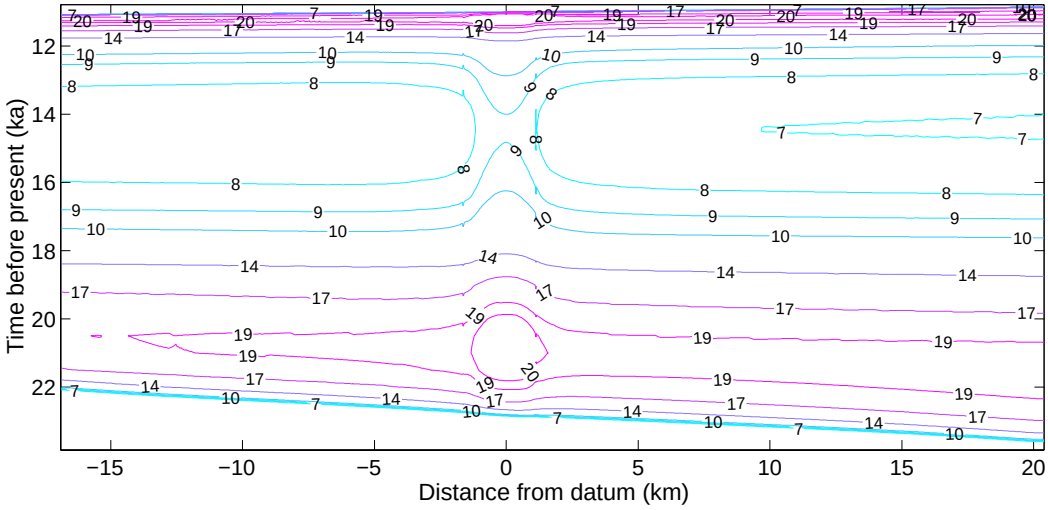

Figure 4.21: Evolution of basal melt rate (mm a^{-1}) in time along the site. Warm scenario.

4.3.3.3 Mechanical response

Figure 4.22 depicts the evolution of vertical displacement at three selected points. The maximum pre-glacial upward displacement, i.e. the frost heave, was approximately 0.089 m for the cold and 0.014 m for the warm scenario, whereas the maximum glacial downward displacement occurring at glacial maximum was about 1.45m for all three scenarios. Horizontal displacements were much smaller. In consequence of melting of pore ice, a slight increase in the downward displacement can be seen for the cold scenario around 2000-3500 years after the onset of glaciation.

The evolution of the minimum and maximum effective principal stresses at three selected points is shown in Figures 4.23 and 4.24, respectively. An examination of simulated effective stresses indicates that the perennial freezing and thawing affect the values through the pore pressure in two different ways: the increase in pore pressure due to freezing of pore water and due to the restricted subpermafrost ground water flow decreases the effective stresses at early stage of glaciation, whereas the decrease in pore pressure due to melting of pore ice increases the effective stresses, as the subglacial bed thaws beneath an advancing glacier.

Despite a considerable increase in pore pressure due to perennial freezing of subsurface, neither hydraulic jacking, i.e. effective tensile stresses, nor shear failure according to the Mohr-Coulomb failure criterion – the minimum Mohr-Coulomb factor of safety of about 1.05 for the cold scenario (see Figure 4.25) – was predicted at the repository depth. However, it was found that the minor pre-glacial effective principal stress, which is vertical, was tensile from the surface to about 100 m below in the rock mass and to about 250 m below in the dipping fracture. In both the rock mass and the fracture zones maximum tensile stresses were approximately 2 MPa, which is less than the prescribed tensile strength of 5 MPa for the rock mass but exceeds the value of 0 MPa for the fracture zones.

The sudden drop in the minor effective principal stress during the retreat of the ice sheet is presumed to be a consequence of that the effective stresses of elastic medium recover much more rapidly than the pore pressure, which is able to dissipate slowly through the very low-permeability rock.

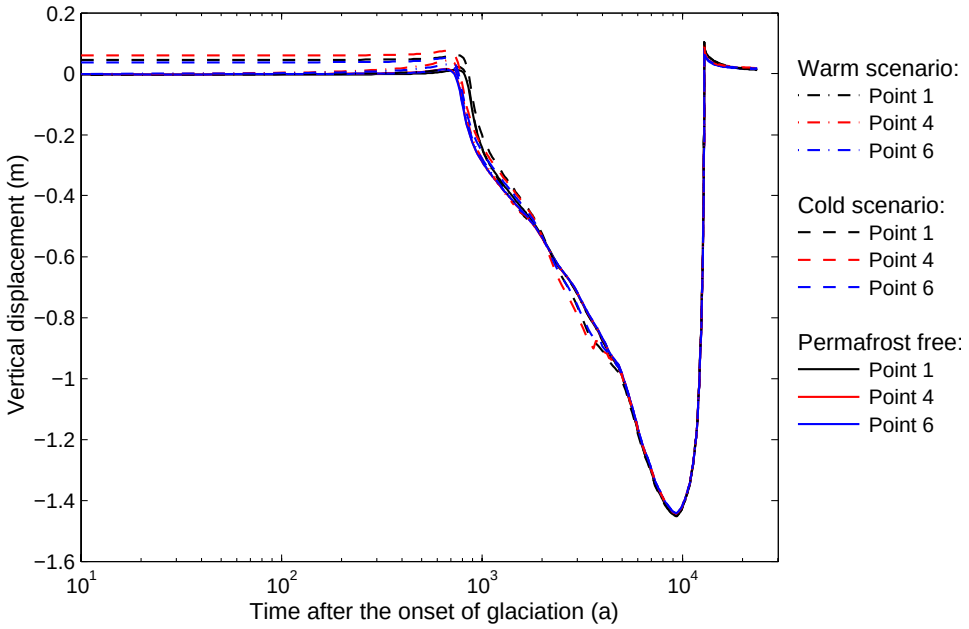

Figure 4.22: Evolution of vertical displacement in the dipping fracture zone (Point 1), in the repository (Point 4) and in the horizontal fracture zone (Point 6).

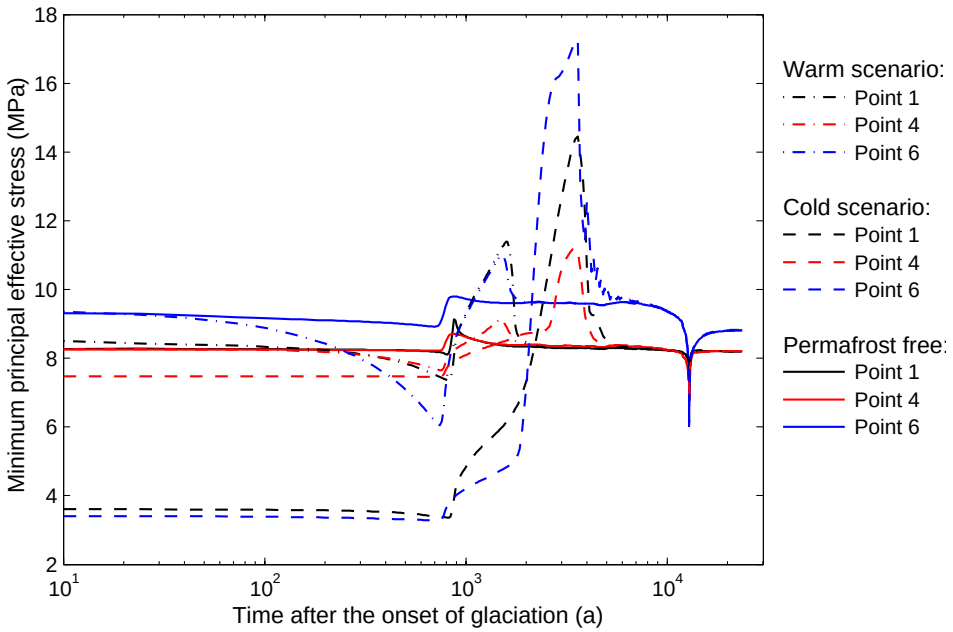

Figure 4.23: Evolution of minimum principal effective stress in the dipping fracture zone (Point 1), in the repository (Point 4) and in the horizontal fracture zone (Point 6).

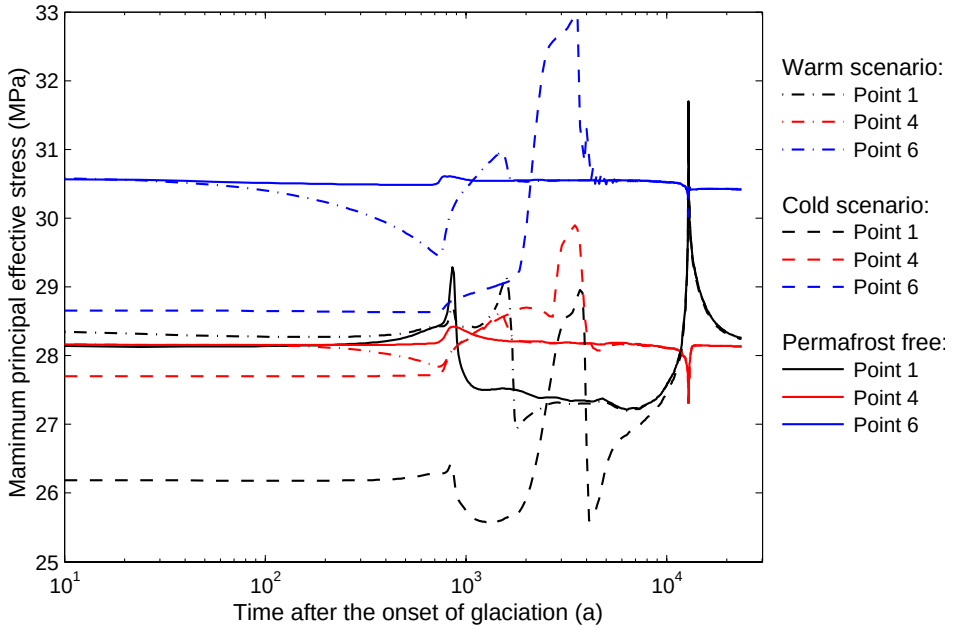

Figure 4.24: Evolution of maximum principal effective stress in the dipping fracture zone (Point 1), in the repository (Point 4) and in the horizontal fracture zone (Point 6).

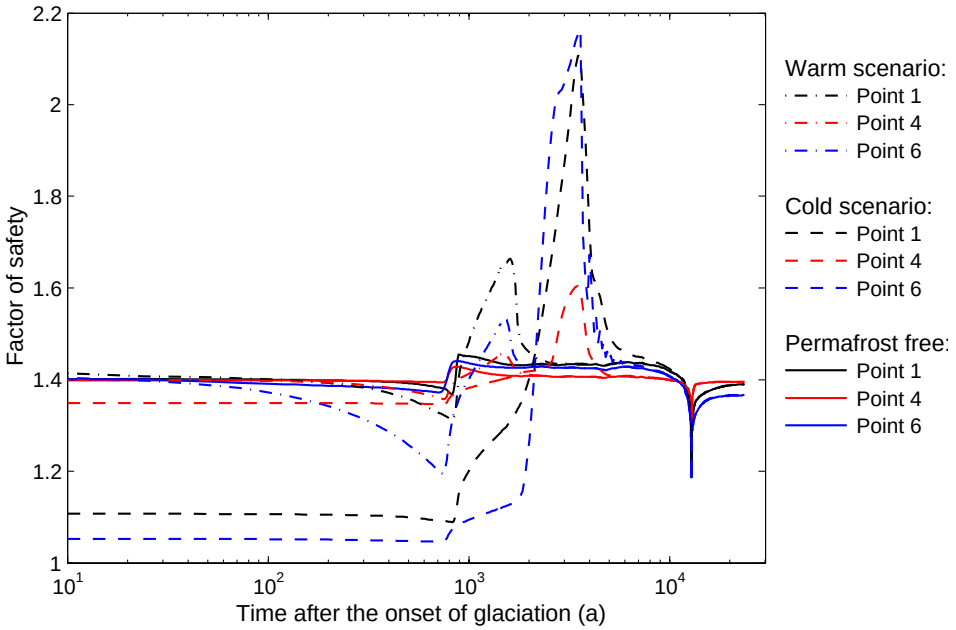

Figure 4.25: Evolution of Mohr-Coulomb factor of safety in the dipping fracture zone (Point 1), in the repository (Point 4) and in the horizontal fracture zone (Point 6).

5 Conclusions

The general conclusions are that impacts of perennial freezing and thawing during a glacial cycle occur on a depth scale that is relevant to the safety of repositories buried several hundreds metres beneath the surface and on timescales that are relevant to safety assessments for long lived waste and that transient coupled processes must be considered in safety assessments.

Site-specific analysis for the Whiteshell site concludes the following:

- Within low-porosity and low-permeability bedrock permafrost and perennially frozen ground can develop into repository depth, the latent heat of water/ice phase change has an insignificant effect on permafrost development and frost heaving is negligibly small.
- Ground water salinity has a minor effect on permafrost development but reduces considerably the creation of perennially frozen ground.
- The heat production of nuclear fuel waste reduces notably the formation of perennially frozen ground, enhances the degradation of perennially frozen subglacial ground and increases basal melting.
- Glaciation generates large heads and head gradients, which undergo rapid changes as the subglacial bed thaws.
- Perennially frozen ground controls effectively the subglacial ground water flow.
- Hydraulic jacking at repository depth is unlikely to be important but mechanical stability can be potential in the perennially frozen ground.
- Local climate and specific fracture zone geometry should be incorporated in site-specific analyses.

The climate is evidently one of the biggest uncertainties for prediction of permafrost development and perennial freezing and thawing of ground. Hence, vegetation, snow cover and water bodies controlling the ground surface temperature need further examination. In addition, a great deal of issues such as seasonal freezing and thawing, chemical impacts, the marine site and the implications of 3-D modelling that were beyond the scope of this study should be taken into consideration. Also the long-term impacts of perennial freezing and thawing should be investigated more closely.

The permafrost model is continuously developed. The incorporation of transport of solutes and the extension to 3-D are under progress. Furthermore, the ice sheet and permafrost models should be integrated so that the whole glacial system can be driven by climate. This is expected to generate a more realistic assessment of the rates of subsurface change, particularly how the rate of loading by the ice sheet is related to water pressure changes and therefore to water/ice phase changes. The rates of change are crucial in determining the extent of water overpressures and possible hydraulic jacking.

6 References

Aalto, J. and Hartikainen, J. 2004. DECOVALEX III, Permafrost modelling in BMT3. Research reports on the Laboratory of Structural Mechanics, TKK-RM-04-03, Helsinki University of Technology.

Boulton, G.S. and Payne, A. 1994. Mid-latitude ice sheets through the last glacial cycle : glaciological and geological reconstructions. In Duplessy, J.-C. and Spyridakis, M.-T. (eds.): Long-term climatic variations. *NATO ASI Series* I 22, 177-212.

Boulton, G.S., Hulton, N. and Vautravers, M. 1995. Ice sheet models as tools for palaeoclimatic analysis - the example of the European ice sheet through the last glacial cycle. Ann. Glaciol.

Burgess, P.E., Palutikof, J.P. and Goodess, C.M. 2000. Investigations into long-term future climate changes. In: Linking Climate Change to Land Surface Change. S.J. McLaren and D.R. Kniveton (eds.), Kluwer Academic Publishers, Netherlands. 231-246.

Chan, T., Christiansson R., Andersson, J., Boulton, G.S, Stanchell, F.W. and Vidstrand, P. 2001. DECOVALEX III, Task 3, BMT 3 BENCHPAR Work-Package 4; Glaciation bench mark test. Prepared by Atomic Energy of Canada Limited for Ontario Power Generation. Ontario Power Generation, Nuclear Waste Management Technical Memorandum Report 06819 (UF)-03781-T10-R00.

French, H.M. 1996. *The periglacial environment*. Second edition. Addison Wesley Longman Limited.

Hartikainen, J. and Mikkola, M. 2003. Thermomechanical modelling for freezing of solute saturated soil. To appear in Proceedings of the IUTAM-Symposium on the mechanics of physicochemical and electromechanical interactions in porous media.

Hivon, E.G. and Sego, D.C. 1995. Strength of frozen saline soils.
Can. Geotech. J., 32, 336-354

Kukkonen, I. 1989. Terrestrial heat flow in Finland, the central Fennoscandian Shield. PhD thesis, Geological Survey of Finland, Report YST-68.

Jaeger, J.C. and Cook, N.G.W. 1976. *Fundamentals of rock mechanics*. Second edition. Fletcher and Son Ltd, London.

Loutre, M.F. 2001. Private communications.

Loutre, M.F. and Berger, A. 2000. Future climatic changes: Are we entering an exceptionally long interglacial. *Climatic Change*, 46, 61-90.

Mahar, L.J., Wilson, R.J. and Vinson, T.S. 1983. Physical and numerical modeling of uniaxial freezing in a saline gravel. In *PERMAFROST*, Proceedings of the Fourth International Conference on Permafrost, Fairbanks, Alaska. Washington D.C. National Academy Press, 773-778.

Mikkola, M. and Hartikainen, J. 2001. Mathematical model of soil freezing and its numerical implementation. *Int. J. Num. Meth. Eng*., 52, 543-557.

Mikkola, M. and Hartikainen, J. 2002. Computational aspects of soil freezing problem. In Proceedings CD of the Fifth World Congress on Computational Mechanics, Vienna, Australia.

Raiko, H. 1996. Thermal optimization of the final disposal of spent nuclear fuel. POSIVA-96-03 (In Finnish).

Washburn, A.L. 1979. *Geocryology*. Arnold, E. London.

Williams, P.J. 1989. *The Frozen Earth*. Cambridge University Press.